Title
Multidimensional optical microscopy for characterization of biology and materials at the nanometer scale

Author
Moon, Seonah

Publication Date
2019

Peer reviewed|Thesis/dissertation

Multidimensional optical microscopy for characterization of biology and materials at the nanometer scale

by

Seonah Moon

A dissertation submitted in partial satisfaction of the

requirements for the degree of

Doctor of Philosophy

in

Chemistry

in the

Graduate Division

of the

University of California, Berkeley

Committee in charge:

Professor Ke Xu, Chair
Professor Phillip Geissler
Professor Seung-Wuk Lee

Spring 2019

Multidimensional optical microscopy for characterization of biology and materials at the nanometer scale

Abstract

Multidimensional optical microscopy for characterization of biology and materials at the nanometer scale

by

Seonah Moon

Doctor of Philosophy in Chemistry

University of California, Berkeley

Professor Ke Xu, Chair

The advent of super-resolution microscopy over the past decade has excited many researchers. Single-molecule localization microscopy (SMLM; to include specific implementations including STORM, (f)PALM, and PAINT), a branch of super-resolution microscopy, offers outstanding spatial resolution of ∼20 nm through single-molecule imaging. Another exciting but often overlooked feature of SMLM is that when properly designed, it may enable ultrahigh-throughput characterization of individual molecules for multiple physical parameters.

The first part of this dissertation describes the multidimensional characterization of single molecules through SMLM. We introduced spectrally-resolved SMLM, which captures the positions and spectra of fluorescent molecules with ultrahigh throughput. Combined with a solvatochromic fluorescent dye, we demonstrated spatial mapping of the local chemical environment for heterogeneous systems. We thus present polarity mapping of lipid membranes in live cells and discuss the origin of the heterogeneity. Difference between plasma membrane and organelle membrane is visualized in live cells, along with their structures and dynamics. We also characterized the structure, polarity, and chemical compositions of adsorbed organic layers on a surface. Besides nanoscale structures of the surface adlayer, we reveal their spontaneous demixing on the surface. Finally, we develop a novel approach for the multidimensional characterization of single molecules through machine learning, in which the parameters of interest are directly extracted from the unmodified diffraction pattern of single fluorescent molecules. We thus demonstrated concurrent spectral separation and axial localization for two fluorescent dyes in fixed cells under SMLM settings.

In Part II, we discuss multiple strategies to improve the performance of optical microscopy, for which efforts we make unusual use of the exceptional mechanical, electrical, and optical properties of graphene, a single layer of bonded carbon atoms. We first take advantage of the superior conductivity of graphene to facilitate correlated correlated SMLM and electron microscopy, in which graphene works as a protective and conductive layer to enable electron microscopy for wet cells. Both the molecular specificity from SMLM and the

high spatial resolution from electron microscopy are thus conveniently achieved. We next demonstrate a novel electroporation-microscopy system based on graphene, which enables the spatially and temporally controlled delivery of fluorescent probes of various sizes into the cells with high efficiency. Remarkably, the superior optical and electrical properties of the graphene allow us to electroporate and image the cells in the same device with precise control and high resolution, thus broadening the palette of fluorescent probe for live cell SMLM. Lastly, we present new methodologies to achieve high-contrast and high-throughput microscopy for graphene itself on transparent substrates. Whereas traditional, transmission microscopy only provide $\sim$3% optical contrast for each layer of graphene, we develop an approach based on interference reflection microscopy (IRM) to achieve $>$10-fold higher contrast on various inorganic and polymer transparent substrates, and demonstrate high-throughput fast imaging with diffraction-limited resolution.

Contents

List of Figures

List of Tables

Acknowledgments

I couldn't thank enough Ke for his guidance and support. Honestly I have very little idea of how the super-resolution microscopy works when I joined his group. Nevertheless, I chose to join his lab because interesting sciences are going on and I could see myself as a part of the team. In past 5 years, I learned how to stay curious, to handle challenging moments in research, and to think about the next steps.

I am grateful to have wonderful lab members, Wan Li, Limin Xiang, Kun Chen, Rui Yan, Bowen Wang, Yunqi Li, Bret Unger, Ha park, Meghan Hauser, Michal Wojcik, Sam Kenny, Zhengyang Zhang, Doory Kim, and Yennie Shyu. They are all smart, motivated, and supportive colleagues. Meghan Hauser, Michal Wojick, Sam Kenny, and Zhengyang Zhang are starting members of the lab, and they helped me a lot when I first moved to the U.S. and joined the group. They deserve every single credit for making me an independent STORM-er. I worked closely with Wan Li on the all the graphene-related projects, and she kindly taught me electochemistry and graphene knowledge. I also enjoyed discussion with Doory Kim, who has extensive experience in STORM, to troubleshoot problems I often faced. Last but not least, I'd like thank all other lab members for their insightful discussion and generous support.

Chapter 1

Introduction

Optical microscopy is a powerful tool for characterization of biological and material systems. Fluorescence microscopy, a type of optical microscopy that relies on fluorescent emission of probes, is a method of choice in cell biology. Often compatible with live samples, fluorescence-based methods provide ways to see the structures of cellular components, interaction between multiple components, measuring chemical/physical properties in the bio-samples.

Diffraction barrier

However, the performance of fluorescence microscopy is limited by diffraction of light. In 1873, a German physicist Ernst Abbe found that the size of diffraction pattern of a point light source is:

$$d = \frac{\lambda}{2n\ sin\theta} = \frac{\lambda}{2NA} \tag{1.1}$$

where λ is wavelength of the light source, n is the refractive index of medium, θ is aperture angle, and NA is numerical aperture of an objective lens. With typical fluorescence microscopy setting where λ is 500$\sim$700 nm and high NA ($\sim$1.4) objective lens, the size of point spread function is $\sim$250 nm. This sets the limit in the resolving power, or spatial resolution of the microscopy. This $\sim$250 nm resolution is far below the size of typical mammalian cells (few tens of μm), but often not enough to clearly visualize the delicate sub-cellular structures and their interactions.

Single-molecule localization microscopy

In the last decade, super-resolution microscopy methods have been developed and earned popularity in visualizing/characterizing (bio)samples. Among them, single-molecule localization microscopy (SMLM) methods, such as STORM (STochastic Optical Reconstruction Microscopy)[7], PALM (PhotoActivaited Localization Microscopy)[8], or PAINT (Points Accumulation for Imaging in Nanoscale Topography)[9] provide 20$\sim$30 nm spatial (lateral) resolution. Unlike conventional widefield fluorescence microscopy where most if not all fluorescent molecules are turned on and imaged all together, single-molecule localization microscopy

takes a series of the images of a small population of the fluorescent molecules. For isolated molecules in each image, the positions could be readily and precisely determined by fitting. Considering the photon shot noise as the only error source, the precision of such fitting is given by:

$$\Delta x = \frac{\sigma_{PSF}}{\sqrt{N}} \tag{1.2}$$

where Δx is the error in localization, σ is the standard deviation of point-spread function, and N is the number of photon[10]. Practically, extra error such as background noise as well as pixelation of the detector also contribute. Then the precision is derived as[10]:

$$\Delta x = \sqrt{\frac{\sigma_{PSF}}{N} + \frac{a^2/12}{N} + \frac{8\pi\sigma_{PSF}b^2}{a^2N^2}} \tag{1.3}$$

where σ_{PSF} is the standard deviation of the PSF, N is the number of photon, a is the pixel size of the detector, and b is the background fluorscence and the detector noise. Typically it provides a few nm precision[10,11], and was first employed in single-particle tracking experiments[12,13], then single-molecule tracking experiments[11,14–16].

In order to isolate the fluorescent molecules to fit individual molecules, photo-switchable fluorescent probes[7], or photo-activable fluorescent proteins[8] are employed in SMLM. A fluorescent molecule exhibits fluctuation in intensity (blinking)[17–21] as it occasionally visits a triplet state (often referred as "dark state"), or photo-switching behavior via photo-induced reactions[22,23]. Blinking kinetics of a fluorescent molecules is carefully tuned through illumination or formulation of imaging media[24] for the optimal performance. Alternatively, reversible binding of fluorescent probes to the target structure[9] is employed to isolate the fluorescent molecules.

Spectrally resolved single-molecule localization microscopy

Relying on the fitting of the isolated single fluorescent molecules, SMLM provides the location (in x, y, and z[25]) of the fluorescent molecules, and temporal information. Other optical characteristics of the fluorescent molecules have not been fully explored in the conventional SMLM. The characteristics of the fluorescent molecules, like emission wavelength, fluorescent lifetime, brightness, along with the spatial information, would bring us rich insight of the sample. Among them, fluorescent spectrum is easily accessible and often closely associated with the chemical environment in the vicinity of the fluorescent probes.

For SMLM, detection of the emission profile of an emitter (single fluorescent molecule) has been done in an indirect, ratiometric fashion[26–31]. In this scheme, the emission from a fluorescent molecule is split into two channels by a dichroic mirror, one for short wavelength emission and another one for longer wavelength. This provides an easy way to estimate the emission profile of an emitter, but the actual spectrum is not obtained in this scheme. To record "true" single-molecule spectra, researchers relied on measuring dispersion of the fluorescence signal from a single spot of the sample. In this scheme, sparsely distributed fluorescent molecules (or particles like quantum dots) were imaged with a scanning-based

microscope[32–34], to map spectral property to positional information. This scheme allows us to record the spectral and spatial information at the same time, but it is rather slow and still diffraction-limited. Our lab recently developed spectrally-resolved SMLM, which provides a way to collect the spectral dimension as well as the positional information with high-throughput[35,36]. In this scheme, the spatial and spectral dimension of blinking fluorescent molecules were collected in parallel fashion.

Emission spectrum of a fluorescent molecule can be shifted by the chemical environment such as pH[37–41], solvent polarity[42–44], or concentration of metal ions[45,46]. Often referred as "environment-sensitive probes", this class of fluorescent probes is a good way to encode and measure the micro-environments of a system. Combined with SMLM, such probes would provide the ultimate sensitivity and superior spatial resolution, single-molecule sensitivity and a few tens of nm of the spatial resolution.

Graphene and its application in microscopy

Graphene is hexagonal meshwork structure of carbon atoms that has been spotlighted for its interesting properties[47]. Graphene is extremely thin thus flexible, transparent, and a great conductor of heat and electricity. In early days of the graphene, it was mechanically exfoliated from a small chunk of graphite with a scotch tape[47,48]. It is now common to synthesize a large scale graphene through chemical vapor deposition (CVD)[49,50], where the graphene grows on a copper or nickle foil. Although the large-scale graphene attracts great interest as a candidate material for transparent and flexible electronics[49–52], optical inspection of graphene in such setting is challenging due to its low light absorbance and thickness[53–59].

In this thesis, I present an interference based approach to visualize and inspect the small-scale defects (typically new hundreds of nm) of the graphene on transparent substrates (e.g. glass or plasitc films). Besides the optical inspection of the graphene, I also discuss exciting applications of graphene in the microscopy fields, in electron microscopy and optical microscopy, taking advantage of its outstanding mechanical, electrical, and optical properties.

Thesis overview

In part I, I present approaches to explore the extra dimensions in single-molecule localization microscopy. We designed and utilized spectrally-resolved super-resolution microscopy to look at nanoscale structures and chemical heterogeneity of biology and chemical systems. Chapter 2 discusses how we use single-molecule fluorescence spectra to map out the chemical polarity (hydrophobicity) of the lipid membranes. In this work, the local chemical polarity of lipid membrane was measured by a fluorescent sensor that changes emission color depending on the chemical polarity. We observed distinct difference between plasma and organelle membrane of a live cell due to their compositional difference. In chapter 3, we applied the same approach to surface chemistry, and looked into the nature of the adsorbed layers of organic solvents on surface. Both nanoscale structures and compositional heterogeniety were explored through spectrally resolved super-resolution microscopy. We compared this with

other microscopy methods, and showed that our method offers a way to look at the delicate adsorbed layers with minimal perturbation. In chapter 4, we demonstrated an alternative approach in spectral imaging through a state-of-the-art computational method, machine learning. We demonstrated three-dimensional, spectral imaging of fluorescent beads that are ∼45 nm apart in the emission wavelength. Furthermore, we applied this approach to a cell sample to perform three-dimensional, two-color imaging. In chapter 5, we summarize and discuss the previous and current efforts to achieve spectral resolution and "functional mapping" in fluorescence microscopy. We discussed a few different methods to resolve single-molecule spectra, and compare their strengths, weaknesses, and suitable applications. We further discussed a few application of spectrally-resolved single-molecule imaging in multi-color imaging, mapping of chemical property, and characterizing single-molecule reaction pathways.

In part II, I present projects that aim to boost the performance and usability of optical microscopy. In particular, we exploited superb properties of a new material, graphene, to improve the performance and potential of optical microscopy. In chapter 6, we present easy and fast correlative microscopy through graphene encapsulation. Correlative light-electron microscopy provides strengths of both optical and electron microscopy. Having graphene as a protective and conductive layer, we could perform electron microscopy of wet cells and correlate them with super-resolution images from our super-resolution microscopy. We achieved near-perfect preservation of delicate cellular structures, and the spatial resolution down to a few nm. In chapter 7, we introduced a novel graphene-based electroporator that broadens choice of fluorescent probe in live cell imaging, thus potentially improves the final image quality. This device delivers a choice of fluorescent probes at various size with high efficiency. We demonstrated live-cell STORM imaging with cell-impermeable organic dye. We also present the spatially-controlled delivery of fluorescent dyes, where a part of adherent cells were labelled in highly selective manner. In chapter 8, we designed a high-performance microscopy for graphene itself. We re-engineered Interference Reflection Microscopy (IRM) to visualize graphene layer(s) on transparent substrates such as glass or plastic films. Compared to other microscopy methods, electron microscopy and atomic force microscopy, we noted that IRM provides superior performance as well as imaging speed. We further demonstrated *in situ* monitoring of crack propagation upon tensile stress.

Below is the full publication list. The works presented in this thesis are in part reproduced from the publications below with permission of all co-authors.

Publication list

1. Kim, T.[#], **Moon, S.**[#], and Xu, K. (2018). Information-rich localization microscopy through machine learning. Nature Communications **10**, 1996.

2. Xiang, L., Wojcik, M., Kenny, S.J., Yan, R., **Moon, S.**, Li, W., and Xu, K. (2018). Optical characterization of surface adlayers and their compositional demixing at the nanoscale. Nature Communications **9**, 1435.

3. Yan, R.[#], **Moon, S.**[#], Kenny, S.J.[#], and Xu, K. (2018). Spectrally Resolved and Functional Superresolution Microscopy via Ultrahigh-Throughput Single-Molecule Spectroscopy. Acc. Chem. Res. **51**, 697-705.

4. **Moon, S.**[#], Yan, R.[#], Kenny, S.J., Shyu, Y., Xiang, L., Li, W., and Xu, K. (2017). Spectrally Resolved, Functional Super-Resolution Microscopy Reveals Nanoscale Compositional Heterogeneity in Live-Cell Membranes. J. Am. Chem. Soc. **139**, 10944-10947.

5. Li, W.[#], **Moon, S.**[#], Wojcik, M.[#], and Xu, K. (2016). Direct Optical Visualization of Graphene and Its Nanoscale Defects on Transparent Substrates. Nano Lett. **16**, 5027-5031.

6. Wojcik, M., Hauser, M., Li, W., **Moon, S.**, and Xu, K. (2015). Graphene-enabled electron microscopy and correlated super-resolution microscopy of wet cells. Nature Communications **6**, 7384.

# denotes equal contribution.

Part I

Spectrally resolved, multidimensional super-resolution microscopy and its application

Super-resolution microscopy has revolutionized the way we look at biological systems. Among a few branches in super-resolution microscopy, single-molecule localization microscopy, such as STORM (STochastic Optical Reconstruction Microscopy)[7] or PALM (Photo-Activated Localization Microscopy)[8] relies on localizing sparsely activated fluorescent molecules, and provides 20∼30 nm spatial resolution. Because of the nature of the imaging process, we can measure physical quantity associated with single molecules, such as spectrum, with high throughput. This enables the measurement at a molecule level and provides the ultimate sensitivity.

In Part I, I present a few applications of the single-molecule measurement, particularly spectral measurement. Such effort was recently initiated by a few groups, including our group. Our group previously reported "true-color" STORM[35], where we combined fluorescence spectroscopy with super-resolution microscopy, and used the spectral dimension for multiplexed imaging. Then we further expand this method to measure micro-environments of heterogeneous systems via environment-sensing fluorescent molecules. Our method provides unique capability to visualize the nanoscale structure and to characterize the chemical heterogeniety. In this part, I present two applications of spatial mapping of hydrophobicity in the heterogeneous systems, namely cell membranes and organic adsorbed layers on surface. I also introduce a new approach for multidimensional single-molecule imaging, where the color and axial position of molecule is directly determined through machine learning. Finally, I summarize previous/ongoing efforts to retrieve spectrum of individual fluorescent molecules, compare their strength and weaknesses, and present applications of spectrally-resolved super-resolution microscopy in biology, surface chemistry, and revealing chemical reaction pathways.

Chapter 2

Spectrally resolved, functional super-resolution microscopy reveals nanoscale compositional heterogeneity in live-cell membranes

The work in this chapter was conducted in collaboration with Rui Yan, Samuel J. Kenny, Yennie Shyu, Limin Xiang, Wan Li and Ke Xu. It is reproduced in part here from ref[1] and with permission from all coauthors.

2.1 Introduction

Our lab previously designed and introduced "True-color" STORM as one form of spectrally-resolved super-resolution microscopy (SR-SRM) and demonstrated multicolor imaging of spectrally-similar dyes in a fixed cell[60]. In this work, we visualized four delicate cellular structures, where they are labelled with four different, but spectrally-similar dyes, only ∼10 nm apart from each other. Here the "color" of the dye indicates the organelle it binds to, so that we characterized shapes of cellular components and interaction among them with high spatial resolution (∼10 nm) and excellent molecular specificity (less than 1% color crosstalk).

However, heterogeneity of a cell is not only present in its shapes, but also in composition and function. Most optical microscopy measurements, including super-resolution microscopy, are good at revealing the geometry and structures, but not often enough to reveal the compositional and functional heterogeneity. The unique capability of our method, SR-SRM, offers a way to encode/decode the chemical heterogeneity of the system through fluorescence spectrum. We hypothesized that the local chemical property could be encoded through a fluorescent sensor, and decoded precisely by reading the spectrum, with ∼10 nm spectral resolution we achieved previously[35]. To prove this concept, we employed a polarity-sensing fluorescent molecule to characterize the compositional and functional heterogeneity of cellular

membranes.

Being chemically interconnected by diffusion and vesicular transport, the cellular membranes are nevertheless compositionally and functionally heterogeneous[61,62]. Biochemical studies indicate remarkable compositional differences between the isolated plasma membrane and organelle membranes[61,63,64], but their native organization in living cells is difficult to visualize[65–67] given the nanoscale dimensions of organelles. For the plasma membrane per se, research over the past two decades has debated the possible coexistence of liquid-ordered (Lo) and liquid-disordered (Ld) membrane domains, but this proposed phase separation at the nanoscale remains indeterminate[68–71].

The difficulty of probing nanoscale heterogeneity in live-cell membranes arises from a lack of means to visualize it in an unbiased manner[70–73]. Labeling specific membrane components or phases with fluorescent probes is subject to labeling specificity and may shift the native equilibrium by stabilizing or disrupting the target being labeled. Environment-sensitive fluorescent probes[74,75], in particular solvatochromic fluorophores that exhibit spectral shifts in media of varied chemical polarity[42,44], provide a possibility to sense membrane heterogeneity without the need to label (and so potentially disturb) a specific target. Instead, the fluorophore may indiscriminately sample the membrane and reports local polarity through spectral changes: a lower local polarity corresponds to less membrane hydration and thus more orderly packed lipids[73,76]. With conventional detection methods, however, the diffraction of light limits spatial resolution to ∼300 nm, and it is still difficult to obtain the full fluorescence spectra for every pixel. The low spatial resolution also limits polarity sensitivity as local differences in spectrum are averaged over all probes in the diffraction-limited volume.

The ultimate sensitivity of environment-sensitive probes may be reached if each probe molecule is individually examined, thus avoiding the averaging of potentially distinct spectra of different molecules. Taking advantage of stochastic fluorescence blinking, SRM techniques[77–79] like STORM (stochastic optical reconstruction microscopy)[7] and PAINT (points accumulation for imaging in nanoscale topography)[9,80] localize single molecules with high spatial resolution. Thanks to the recent advent of SR-SRM[35,36,81–83], a recent study[82] combined Nile Red, a solvatochromic dye, with SR-PAINT to enable surface hydrophobicity mapping.

By achieving Nile Red-based SR-STORM and SR-PAINT for live-cell membranes, we here detected local variations in membrane chemical polarity with single-molecule sensitivity and ∼30 nm spatial resolution. This functional (as opposed to conventional, shape-only) SRM approach enabled us to directly visualize nanoscale compositional heterogeneity in the membranes of live mammalian cells.

2.2 Result and discussion

2.2.1 Nile Red-based spectrally-resolved PAINT (SR-PAINT) enables polarity sensing of supported lipid bilayers

We originally realized SR-STORM with a dual-objective design in which the sample was sandwiched between two opposing objective lenses[35]. For compatibility with live cells, in this study we built a new system based on an inverted microscope (Figure 1a and Supplementary Information). Fluorescence blinking of single Nile Red molecules was achieved with a 561 nm excitation laser through photoswitching (STORM)[84] or reversible binding to membranes (PAINT)[9,80]. Obtained single-molecule fluorescence was split into two light paths. Path 1 provided the position of each molecule, and a dispersive prism was inserted into Path 2 to generate spectra of the same molecules. The resultant single-molecule images and spectra in the wide-field were concurrently recorded on two different areas of an EM-CCD at 110-220 frames per second (4.5-9 ms integration per frame; Figure 1bc and Movie S1 in ref[1] for representative raw data at a supported lipid bilayer and a live cell, respectively). With $\sim$30 molecules detected in each frame (probe density $<$0.1 molecules/μm^2), we obtained the emission spectra and super-resolved locations of $>10^6$ single Nile Red molecules in a few minutes, thus enabling the re-construction of super-resolution SR-STORM/SR-PAINT images that carried functional information on local chemical polarity. Concurrent positional and spectral recording may also be achieved via the zeroth and first diffraction orders of a grating[36,82,85], but gratings achieve low light efficiency, and the strong dispersion makes it difficult to probe densely labeled two-dimensional structures like cellular membranes.

We first applied Nile Red-based SR-PAINT to supported lipid bilayers of different compositions. Averaged spectra of the measured single Nile Red molecules (Figure 1d) showed the reddest spectrum for a bilayer of the unsaturated lipid 1,2-dioleoyl-sn-glycero-3-phosphocholine (DOPC), a model system for the Ld phase of the plasma membrane[43]. A bilayer of a 1:1 mixture of DOPC and sphingomyelin (SM), a more saturated lipid, showed a modest ($\sim$5 nm) blue-shift. Further addition of cholesterol (Chol) led to a substantial ($\sim$20 nm) blue-shift. These results are consistent with previous measurements on model lipid vesicles[43,73,76]: Nile Red exhibits fluorescence blueshifts in media of reduced polarity; the DOPC-only bilayer is the least orderly packed and so the most hydrated and polar, whereas cholesterol assists the packing of sphingolipids into more ordered and less hydrated membrane phases.

2.2.2 SR-PAINT/STORM on live cell membranes reveals a difference between plasma membrane and organelle membrane

We next achieved Nile Red-based STORM and PAINT for membranes in live mammalian cells. For STORM, cells were labeled with 100 nM Nile Red, and imaged in a buffer containing ascorbic acid to assist photoswitching. For PAINT, unlabeled cells were imaged in a

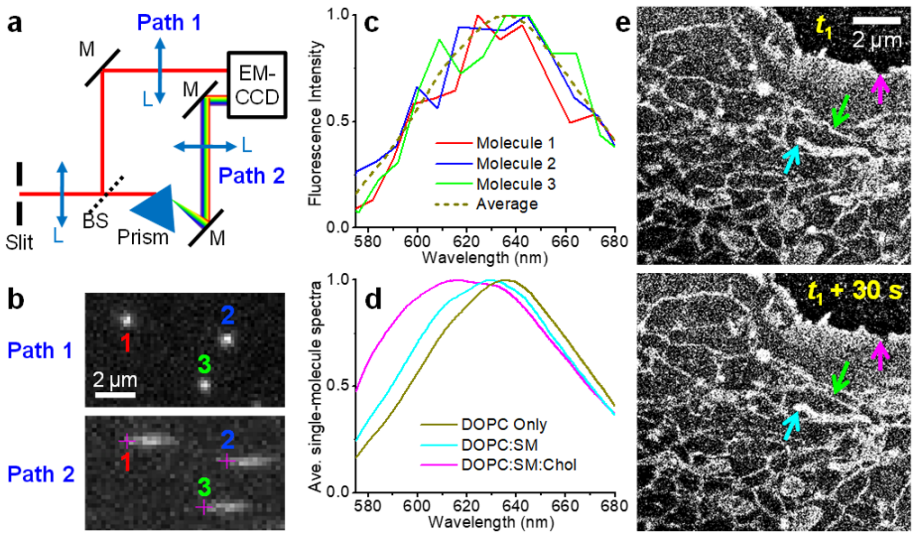

Figure 1: SR-STORM/SR-PAINT with Nile Red. (a) Schematic of setup. Slit is at the camera port of an inverted microscope. L, lens; BS, beam splitter; M, mirror. (b) A small region of the concurrently acquired images and spectra of single Nile Red molecules in a DOPC bilayer, obtained in a 6-ms snapshot. Crosses denote the mapped spectral positions of 590 nm for each molecule. (c) Spectra of the 3 molecules in (b), compared to that averaged from 280,898 single molecules from the same sample. (d) The averaged spectra for single Nile Red molecules labeled to sup-ported lipid bilayers of different compositions (DOPC, DOPC:SM 1:1, and DOPC:SM:Chol 1:1:1). (e) Sequential STORM images of a Nile Red-labeled live COS-7 cell at 30 s separation. Magenta, green, and cyan arrows point to structural changes in the plasma, ER, and mitochondrial membranes, respectively.

buffer containing 3 nM Nile Red for reversible binding to the membrane during imaging. For both approaches, the cell plasma membrane and the membranes of intracellular organelles were well labeled and visualized at the nanoscale [Figure 1e; arrows point to example endoplasmic reticulum (ER) (elongated tubular structures), mitochondria (thicker lumps), and plasma membrane]. With 50 % fluorescence split to the image channel, we detected ∼800 photons per molecule. This value is comparable to that of several known membrane STORM dyes, and translates to a spatial resolution of ∼30 nm (localization precision in full width at half maximum)[86]. Consistent with this resolution, the thinner ER tubules appeared 50-100 nm in width in our images, in agreement with previous results[86]. Three-dimensional STORM/PAINT indicated that for the plasma membrane, it was typically the top (apical) membrane that was imaged, which went out of the focal range for thicker parts of the cell (SI in ref[1]). STORM/PAINT image sequences were obtained at 30 s time resolution, which allowed us to track the morphological evolution of cellular membranes far beyond the diffraction limit (Figure 1e and Movie S2 in ref[1]).

Integrating Nile Red-based cell-membrane imaging with SR-STORM/SR-PAINT, we next asked whether the lipid composition-sensing capability we demonstrated for supported bilayers could reveal possible heterogeneities in the membrane composition of live mammalian cells. Remarkably, we observed significant spectral differences between Nile Red molecules

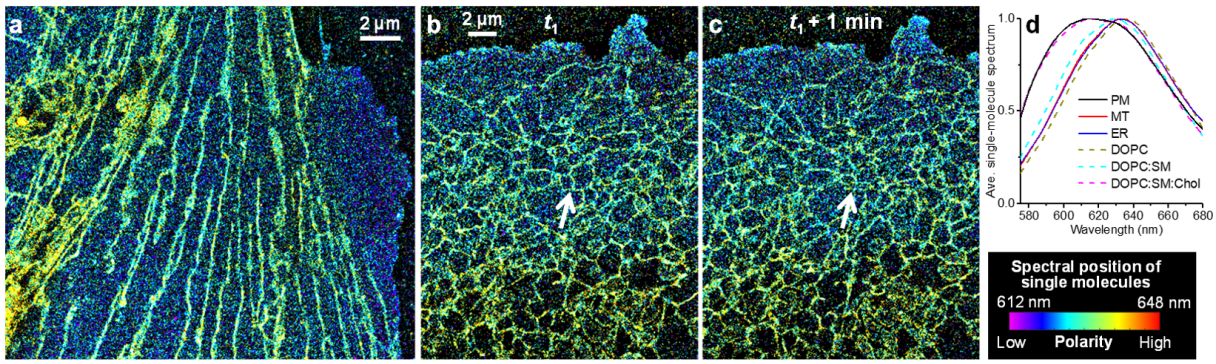

Figure 2: Spectrally resolved, functional SRM visualizes polarity differences between organelle and plasma membranes in live cells. (a) True-color SR-PAINT image of a Nile Red-labeled live PtK2 cell. Each detected single molecule is color-coded according to its spectral mean [color bar below (d)]. (b,c) Sequential true-color SR-STORM images of a Nile Red-labeled live COS-7 cell at 1 min separation. Arrows point to notable structural changes in ER. (d) Averaged spectra of single Nile Red molecules from different nanoscale regions in live cells at the plasma membrane (PM), mitochondria (MT), and ER, compared to that at model supported lipid bilayers of different com-positions.

at the plasma membrane and at the intracellular membranes of nanoscale organelles.

To present both the spectral and spatial information of every detected Nile Red molecule ($\sim 10^6$ total for a typical image), we calculated the spectral mean of each molecule as the intensity-weighted average of wavelength[35,87], and used this value to assign a color on a continuous scale (612-648 nm) as we plotted the position of each molecule. The resultant "true-color" SRM[35] images showed strikingly different colors for the plasma membrane (blue) and organelle membranes (yellow) (Figure 2a-c). Image sequences further showed that as the plasma and organelle membranes underwent dynamic structural rearrangements at the nanoscale, their respective spectral characteristics were maintained (Figure 2bc, Movie S3, and SI in ref[1]). Highly similar results were obtained from SR-PAINT and SR-STORM (Figure 2a-c and SI in ref[1]), and across different cell types (Figure 2a: PtK2, rat kangaroo epithelial cell; Figure 2bc: COS-7, monkey fibroblast). Fixed cells exhibited similar spectral characteristics as live cells (Figure 3), indicating that the membrane compositions are stable upon chemical fixation. The locally averaged single-molecule spectra, as computed from nanoscale subareas of the SR-STORM/SR-PAINT data, were nearly identical for mitochondrial and ER membranes, but showed a strong blueshift of $\sim$20 nm for the plasma membrane (Figure 2d), with results from different cells being identical (SI in ref[1]). Distribution of the measured single-molecule spectral means (Figure 4) showed similar standard deviations for the mitochondrial and plasma membranes over a DOPC bilayer ($\sim$6 nm), likely limited by our spectral precision. A slightly larger standard deviation of 7 nm was observed for the ER membrane.

Together, these results reveal fundamental differences be-tween the organelle and plasma membranes: the redder spectra of organelle membranes suggest that they are physically more polar, structurally less ordered, and functionally more flexible and permeable to water,

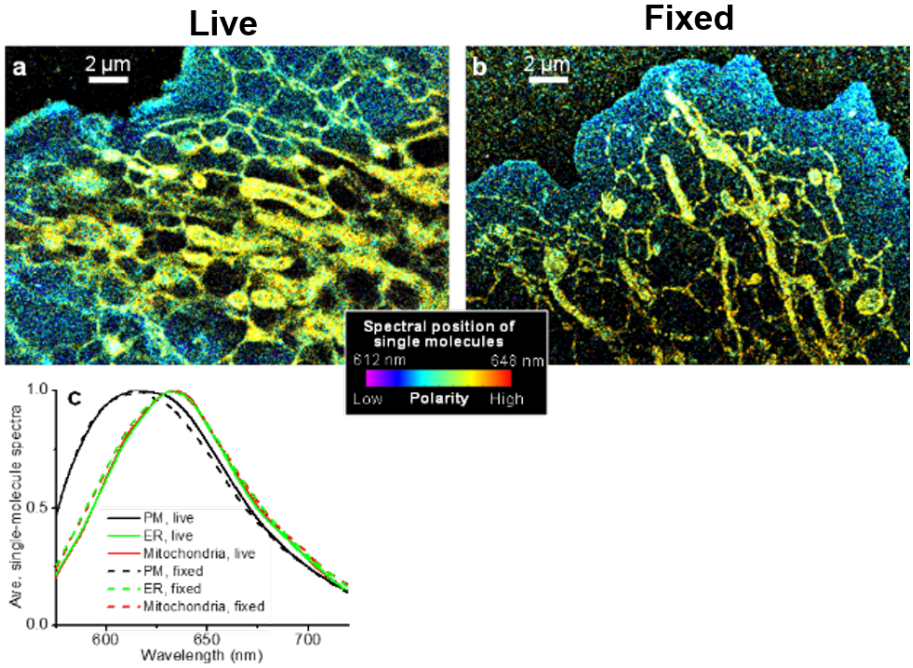

Figure 3: Comparison of Nile Red-based SR-STORM results on live and fixed cells. (a,b) True-color SR-STORM images of Nile Red-labeled live (a) and fixed (b) COS-7 cells. (c) Locally averaged Nile Red single-molecule spectra at the plasma membrane (PM) and mitochondrial and ER membranes, for the live (solid curves) and fixed (dotted curves) cells.

consistent with their intracellular functions[61,63].

Bulk measurements on isolated organelle and plasma membranes indicate that the former and latter are characterized by low ($<\sim$5 %) and high ($\sim$30-40 %) cholesterol levels[61,63,64], respectively. As cholesterol assists the packing of lipid bilayers into more ordered and less hydrated membrane phases[61,73,76], it may explain the significant differences in single-molecule spectra we observed between organelle and plasma membranes. Indeed, a comparison of our SR-STORM/SR-PAINT results on live-cell membranes and sup-ported lipid bilayers showed that the organelle membranes are spectrally similar to cholesterol-free bilayers, whereas the plasma membrane is spectrally similar to the DOPC:SM:Chol (1:1:1) bilayer (Figure 2d).

2.2.3 SR-STORM reveals the polarity change of the membranes upon cholesterol level manipulation

To understand whether cholesterol is indeed the driving force behind the membrane polarity differences we observed, we next combined Nile Red-based SR-STORM with cholesterol manipulation via methyl-β-cyclodextrin (MβCD)[88]. Depleting cholesterol with MβCD led to a strong redshift of Nile Red single-molecule spectra at the plasma membrane but little change at organelle membranes, as evidenced by both true-color SRM images and locally averaged

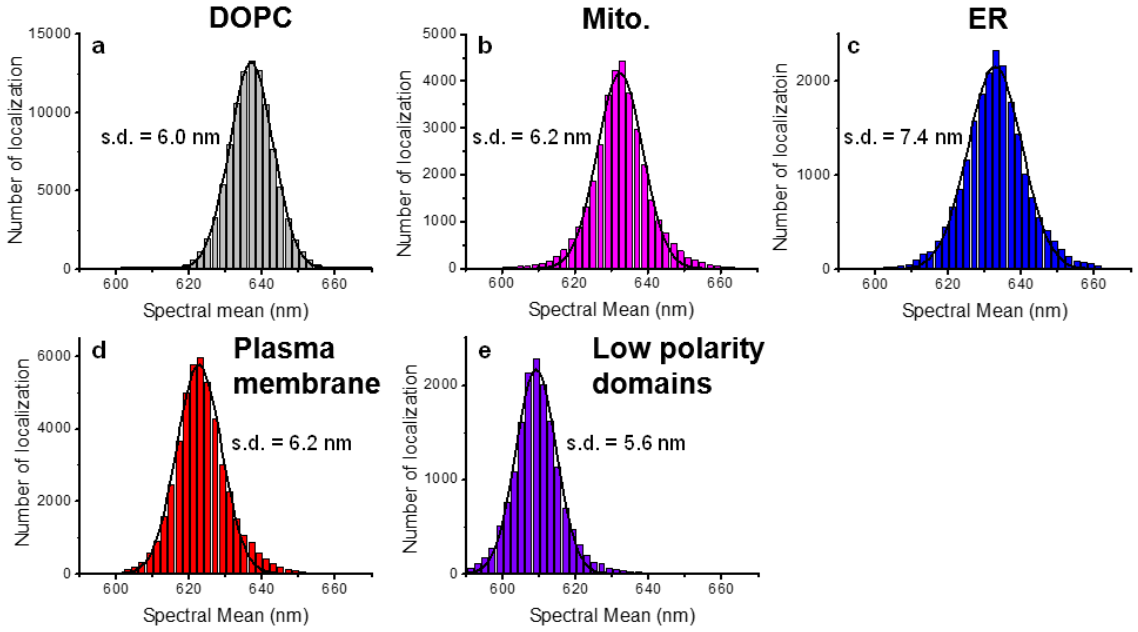

Figure 4: Distribution of the measured spectral means of single Nile Red molecules at different membranes. (a) Supported lipid bilayer of DOPC. (b) Mitochondrial membrane. (c) ER membrane. (d) Plasma membrane. (e) Low-polarity nanodomains induced by CTB. Black lines are Gaussian fits with standard deviations (s.d.) labeled in each subfigure. The standard deviation of 6.0 nm in the (relatively homogenous) DOPC bilayer is likely limited by our measurement precision of single-molecule spectra. The similar standard deviations of 6.2 nm observed for the mitochondrial membrane and the plasma membrane suggest that they are not significantly more heterogeneous than the DOPC bilayer at the spectral precision of our experiments. The ER membrane showed a slightly larger standard deviation of 7.4 nm, which may be related to its active lipid dynamics.1 A slightly smaller standard deviation of 5.6 nm was found for the low-polarity nanodomains, attributable to brighter single molecule signals (Figure 6e).

single-molecule spectra (Figure 5ab and SI in ref[1] for fixed and live cells, respectively).

In contrast, upon addition of 1 mM water-soluble cholesterol (cholesterol-MβCD), the organelle membrane spectra blue-shifted markedly to become closer to that of the plasma membrane as the latter remained spectrally unchanged (Figure 5ce and SI in ref[1] for fixed and live cells, respectively). While live cells were resistant to further addition of cholesterol (SI in ref[1]), for fixed cells substantial blue-shifts were observed for both the plasma and organelle membranes with 5 mM water-soluble cholesterol, so that both became bluer than that of the untreated plasma membrane (Figure 5de). A portion of the organelle membranes, however, appeared resistant to cholesterol addition, as indicated by nanoscale regions with redder colors in true-color SRM images and a shoulder peak in the locally averaged single-molecule spectra. Together, these results indicate that cellular cholesterol levels were responsible for the polarity differences we found for the plasma and organelle membranes.

Intriguingly, for fixed cells treated with 5 mM water-soluble cholesterol, in addition to an overall blueshift, SR-STORM further revealed nanoscale (apparent size $\sim$100 nm; Figure 7) domains (arrows in Figure 5d) of strongly blue-shifted spectra (Figure 5e) dispersed

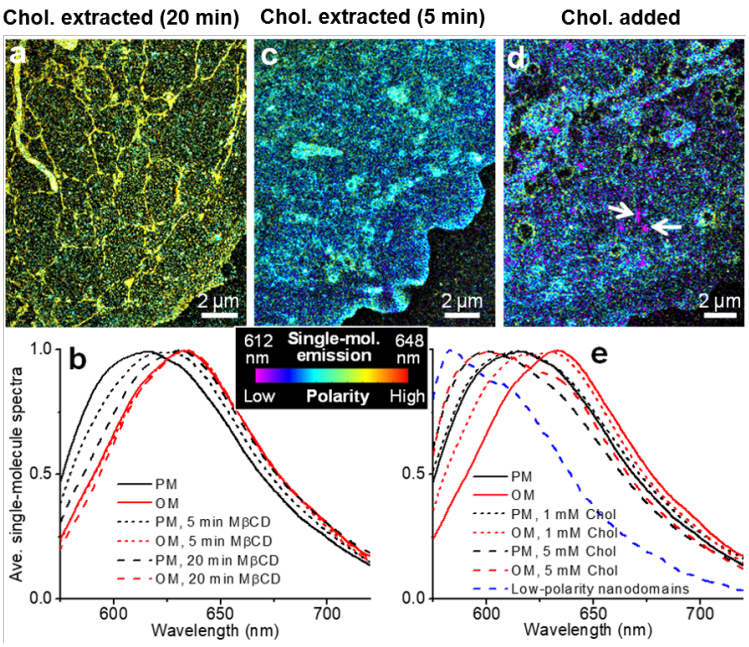

Figure 5: The observed heterogeneity in cellular membrane polarity is driven by cholesterol. (a) True-color SR-STORM image of a Nile Red-labeled fixed COS-7 cell after depletion of cholesterol with 5 mM MβCD for 20 min. (b) Averaged single-molecule spectra at the plasma membrane (PM) and organelle membrane (OM) after 5 and 20 min treatment of 5 mM MβCD, compared to that of untreated cells. (c,d) True-color SR-STORM images of Nile Red-labeled fixed COS-7 cells after cholesterol enrichment with 1 mM (c) and 5 mM (d) water-soluble cholesterol. Arrows in (d) point to low-polarity nanodomains. (e) Averaged single-molecule spectra at the plasma membrane (PM) and organelle membrane (OM), as well as at the low-polarity nanodomains, after cholesterol enrichment, compared to that of untreated cells.

across the plasma membrane. This finding, enabled by the unbiased sensing of local polarity by single Nile Red molecules, provides direct visual evidence of nanoscale phase separation of the plasma membrane. The strongly blue-shifted local spectra (Figure 5e) indicate highly nonpolar, orderly packed membrane domains, reminiscent of the long-hypothesized cholesterol-rich, raft-like liquid-ordered (Lo) nanodomains in the cell plasma membrane[68–71].

2.2.4 Drug-induced, low-polarity nanodomains observed by SR-STORM

To further examine this possibility and elucidate whether raft-like nanodomains can also be observed in cells without cholesterol addition, we next attempted to stabilize Lo do-mains with cholera toxin B-subunit (CTB), a common lipid-raft marker and stabilizer[72,89] that crosslinks ganglioside GM1 (SI in ref[1]). Indeed, the application of CTB to cells induced blue-shifted nanoscale domains (Figure 6a and SI in ref[1] for fixed and live cells, respectively) that partly co-localized with CTB (Figure 6b and SI in ref[1]), and the local single-molecule spectra (Figure 6c) were similar to those in cells with cholesterol addition (Figure 5e). In-

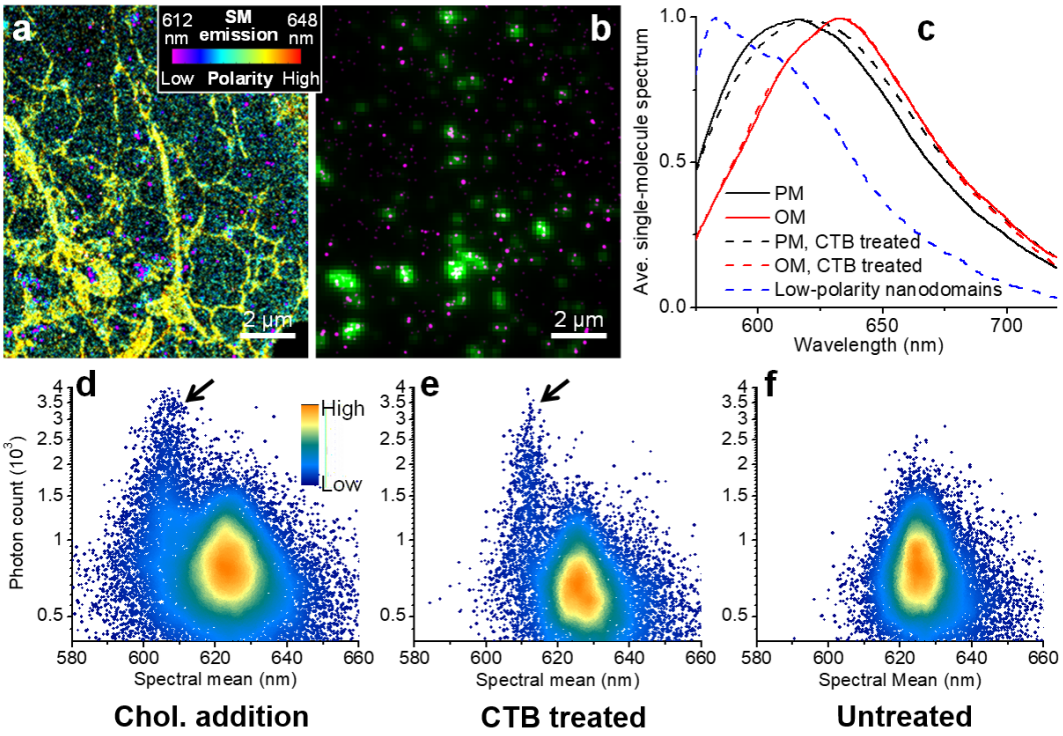

Figure 6: Functional SR-STORM examination of the low-polarity phase. (a) True-color SR-STORM image of a Nile Red-labeled COS-7 cell after CTB treatment and fixation. (b) The low-polarity nanodomains (magenta) overlaid with epifluorescence of the dye-tagged CTB (green). (c) Averaged single-molecule spectra at the plasma membrane (PM), organelle membrane (OM), and the induced low-polarity nanodomains after CTB treatment, compared to that of control cells. (d-f) Distributions of the measured spectral mean and photon count for single Nile Red molecules at the plasma membranes of cholesterol-enriched (d), CTB-treated (e), and control (f) COS-7 cells.

terestingly, we also observed a slight redshift for the rest of the plasma membrane (Figure 6c), attributable to global lowering of cholesterol levels as cholesterol was sequestered to the CTB-induced raft-like nanodomains. Meanwhile, no change in spectrum was observed for organelle membranes.

Our finding that raft-like, low-polarity nanodomains were only observed in cholesterol-added or CTB-treated cells suggests raft-like Lo domains may be absent in native cells. To examine if this interpretation is limited by our spatial resolution (∼30 nm), we next employed a unique advantage of SR-STORM/SR-PAINT owing to its nature as ultrahigh-throughput single-molecule spectroscopy: without using any spatial information, individual molecules residing in phases of different polarities should show up as different subpopulations in single-molecule statistics. Indeed, for cholesterol-added and CTB-treated cells, the Lo phase is readily identified as a subpopulation of single molecules that are bluer in spectrum and brighter[90] in intensity (arrows in Figure 6de and SI in ref[1]). Such a subpopulation is absent in untreated cells (Figure 6f). This observation suggests that in untreated cells, Lo nanodomains do not exist as a significant fraction of the membrane at time scales longer

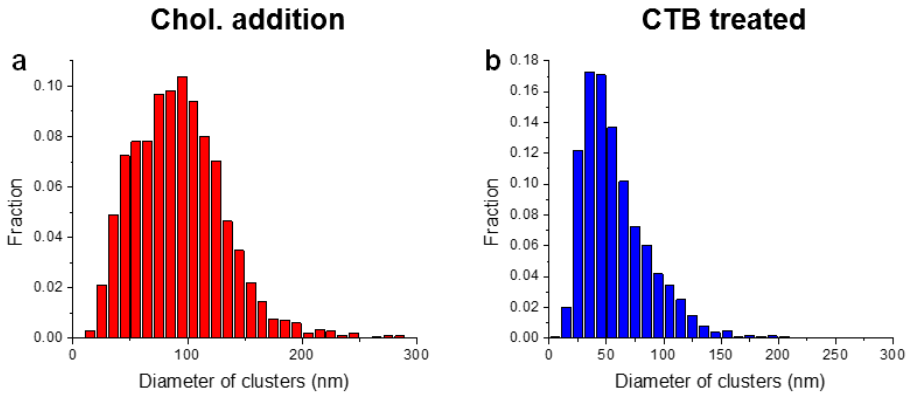

Figure 7: Distribution of the apparent sizes of low-polarity nanodomains in COS-7 cells induced by (a) addition of 5 mM water-soluble cholesterol and (b) application of CTB. Diameter of each nanodomain was defined by the smallest circle that could enclose 90% of the single-molecule localizations of the nanodomain. The resultant circle diameters are inflated by possible non-circular geometry of the nanodomains, as well as our localization uncertainty of ∼30 nm in FWHM. The generally larger sizes observed with cholesterol addition (average: 90 nm) when compared to the CTB treatment (average: 60 nm) may be related to the different available amounts of cholesterol in the plasma membrane.

than our spectral integration time (5-9 ms), a result in line with evidence from recent single-molecule diffusion experiments[91,92]. However, we do not rule out the possibility that even a single Nile Red molecule could perturb the lipid dynamics in its immediate vicinity.

2.3 Conclusion

By obtaining the fluorescence spectra and super-resolved positions of $\sim 10^6$ polarity-sensing single molecules per experiment, our functional SRM approach allowed for the unbiased visualization of nanoscale heterogeneity in live-cell membranes. The ultimate sensitivity we achieved through examining the spectra of individual molecules also opens the door to future interrogations of other parameters in live cells, including local pH, viscosity, and protein activity, at the nanoscale. The identification of suitable fluorescent probes for such applications, either independent of or in tandem with Nile Red, as well as the combination of functional SRM with traditional structural SRM experiments, represents immediate challenges.

2.4 Materials and Methods

Optical setup

SR-STORM and SR-PAINT were achieved on a home-built setup (Figure 1a) based on a Nikon Ti-E inverted fluorescence microscope. A 561-nm laser (Coherent) was introduced to the back focal plane of an oil-immersion objective lens (Nikon CFI Plan Apochromat λ 100x, NA 1.45) via a dichroic mirror (ZT561rdc, Chroma). A translation stage was used to shift

the laser beams toward the edge of the objective lens such that the excitation light reached the sample at incidence angles slightly smaller than the critical angle of the coverglass-water interface, illuminating 1 μm into the sample. Emission was filtered by a long-pass (ET575lp, Chroma) and a short-pass (FF01-758/SP or FF01-715/SP, Semrock) filter, and cropped at the image plane of the microscope camera port to a width of ∼4 mm. The cropped intermediate image was collimated by an achromatic lens (f = 80 mm) for splitting into two perpendicular paths at a 50:50 beam splitter (BSW10, Thorlabs). In Path 1, emission was focused by an achromatic lens (f = 75 mm) onto one-half of an electron-multiplying charge-coupled device (EM-CCD) camera (iXon Ultra 897, Andor) to achieve an effective magnification of ∼94x. In Path 2, emission was dispersed by an equilateral calcium fluoride (CaF_2) prism (PS863, Thorlabs) before being focused by an achromatic lens (f = 60 mm) onto the other half of the same camera, thus resulting in an effective magnification of ∼75x. Wavelength calibration was performed using fluorescent beads and narrow bandpass filters, as described previously[35]. Briefly, 100-nm diameter, four-color fluorescent beads (T7279, Life Technologies) were adsorbed to a glass coverslip at low density. The sample was mounted and imaged on the setup with 405 nm, 561 nm, or 647 nm excitation. Beads appeared as diffraction-limited spots in Path 1, and as dispersed 1D spectra in Path 2. Bandpass filters with 10 nm bandwidth were used to determine the spectral positions of different known wavelengths in Path 2 relative to the bead positions in Path 1. Three-dimensional (3D) STORM/PAINT microscopy was achieved through cylindrical lens-based astigmatism[25].

Supported lipid bilayers

Supported lipid bilayers were prepared via vesicle fusion of small unilamellar vesicles (SUVs). 1,2-dioleoyl-sn-glycero-3-phosphocholine (DOPC) and sphingomyelin were purchased from Avanti Polar Lipids (850375 and 860062). Cholesterol was purchased from Sigma (C8667). Each lipid was separately dissolved in chloroform at concentrations of 10 mg/mL. To prepare SUVs, the chloroform solutions of lipids were mixed in a pre-cleaned flask at designated ratios. After evaporation of chloroform with nitrogen flow, the flask was filled with ∼55 °C mili-Q water to form a 2 mg/mL lipid-water mixture. The mixture was sonicated at 60 °C for ∼40 min to form a clear SUV suspension. To form supported lipid bilayers on glass, hydrophilic glass coverslips were prepared by treatment with hot piranha solutions (H_2SO_4:H_2O_2 at 3:1). The coverslip was incubated in a 1:4 mixture of the SUV suspension and a buffer solution (10 mM HEPES, 150 mM NaCl, 3 mM $CaCl_2$) at 60 °C for 15 min. After incubation, excess SUVs were rinsed away thoroughly with Dulbecco's phosphate-buffered saline (DPBS).

Cell culture

COS-7 and PtK2 mammalian cells were maintained in Dulbecco's Modified Eagle's Medium (DMEM) with 10% fetal bovine serum (FBS), 1x non-essential amino acids (NEAA) and 1% penicillin/streptomycin in 5% CO_2 at 37 °C. For imaging, cells were plated at a density of 10,000/cm^2 on 12-mm diameter glass coverslips, 35 mm glass-bottomed dishes (P35G-

1.5-14-C, MatTek), or chambered coverglass (Thermo Scientific Nunc Lab-Tek II) to achieve a confluency of ∼50% after growth of two days. For the fixed-cell SR-STORM/SR-PAINT experiments, cells were fixed with 3% paraformaldehyde and 0.1% glutaraldehyde in DPBS for 20 min, followed by a rinse with 0.1% $NaBH_4$ solution in DPBS for 5 min and three washes with DPBS. For two-color epifluorescence of GM1 and CTB, cells were fixed with 4% paraformaldehyde in DPBS and washed once with DPBS (SI in ref[1] and caption).

Cholesterol depletion and addition

For cholesterol depletion, live or fixed cells were treated with a 5 mM solution of methyl-β-cyclodextrin (MβCD; Sigma C4555) in Leibovitz's L-15 medium (for live cells) or DPBS (for fixed cells) for 5-20 min. For cholesterol addition, live or fixed cells were treated with 1 or 5 mM solutions of water-soluble cholesterol (cholesterol-MβCD; Sigma C4951) in L-15 medium (for live cells) or DPBS (for fixed cells) for 30 min-2 h. Cells were then gently washed twice with L-15 medium (for live cells) or DPBS (for fixed cells).

Cholera toxin B-subnit treatment

Cholera Toxin Subunit B-Alexa Fluor 647 conjugate (CTB-AF647) was purchased from Invitrogen (C34778). Cells were briefly rinsed with Leibovitz's L-15 medium, and then incubated in 1 μg/mL CTB-AF647 in L-15 medium for 5-10 min at room temperature. Cells were washed twice with L-15, and immediately imaged as live cells or fixed as described above.

Nile Red staining

Nile Red (415711000, Acros Organics) was dissolved in dimethyl sulfoxide (DMSO) to a 3 mM stock solution. For live-cell experiments, cells were briefly rinsed with 37 °C L-15 medium. For SR-STORM, cells were incubated with 100 nM Nile Red in L-15 medium for 20-30 min at 37 °C, and then washed with 37 °C L-15 medium for two or three times before imaging. For fixed samples, cells were stained with 100 nM Nile Red solutions in DPBS, and then washed with DPBS for two or three times. For SR-PAINT, cells were not stained before imaging, and Nile Red was introduced in the imaging buffer (below).

SR-STORM and SR-PAINT imaging

SR-STORM and SR-PAINT were carried out on the optical setup described above. For SR-STORM, imaging buffer was L-15 medium (for live cells) or DPBS (for fixed cells) containing 100-200 μM ascorbic acid[84]. For SR-PAINT, imaging buffer was 3 nM Nile Red in either L-15 medium (for live cells) or DPBS (for fixed cells and supported bilayers). The sample was illuminated with the 561 nm laser at an intensity of ∼2 kW/cm^2, which led to sparsely distributed images (Path 1) and spectra (Path 2) of single molecules in the wide-field due to

the photoswitching (in STORM) or the dynamic binding/dissociation (in PAINT) of individual Nile Red molecules. The EM-CCD concurrently recorded the single-molecule spectra and images at 110 frames per second for a frame size of 512x256 pixels, or at 160-220 frames per second for a frame size of 512x128 pixels, and typically recorded 30,000-100,000 frames for each experiment. With ∼30 molecules detected across each frame, the emission spectra and images of $<10^6$ single molecules were thus obtained within a few minutes. To map[35] the spectral and spatial coordinates of Path 1 and Path 2, a narrow bandpass filter centered at 590 nm (FF01-590/10, Semrock) was placed before the beam splitter for the final ∼5,000 frames of the recorded movie. Comparison of the single-molecule images in Path 1 and the 590 nm-filtered single-molecule spectra in Path 2 thus enabled the generation of a mapping function between the spatial positions in Path 1 and the spectral positions of the 590 nm wavelength for Path 2. To analyze the SR-STORM/SR-PAINT data, the super-localized positions of single molecules in Path 1 were projected to Path 2 based on this mapping function. Single-molecule spectra were thus obtained based on the mapped position of 590 nm for each molecule and the aforementioned calibration curve obtained from fluorescent beads. Overlapping spectra were excluded from analysis. The spectral mean of each molecule was calculated as the intensity-weighted average of wavelengths for the measured single-molecule spectrum, and presented on a continuous color scale as "true-color" super-resolution images[35]. For live-cell results, time sequences of (SR-)STORM/PAINT images were generated using all the single-molecule localizations and spectra collected between the indicated time point (e.g., t1) and the next time point in the sequence (e.g., t1 + 30 s). Local averages of single-molecule spectra were calculated from nanoscale regions of the SR-STORM/SR-PAINT data for plasma membrane, mitochondrial membrane, and ER membrane of well-defined morphologies. Note that for thinner parts of the cell (e.g., top 2/3 of Figure 2bc and along the edge of the cell in SI in ref[1]), the presence of the top plasma membrane confuses the local spectra of mitochondrial and ER membranes (c.f. SI in ref[1]). Such regions were avoided in our analysis of the local spectra of organelle membranes.

Chapter 3

Optical characterization of surface adlayers and their compositional demixing at the nanoscale

The work presented in this chapter was conducted in collaboration with Limin Xiang, Michal Wojcik, Samuel J. Kenny, Rui Yan, Wan Li, and Ke Xu. It is in part reproduced here from ref[2] with permission from all coauthors.

3.1 Introduction

In the previous chapter, I discussed how Nile red, a solvatochormic dye, was employed to measure the polarity and hydration level of the biomembranes. While the solvatochromic dye is now a popular way to characterize the hydration level and order of the lipid membranes[44], often cellular membranes, its origin traces back to a solvent polarity indicator[42]. In this chapter, I discuss how we characterize the chemical polarity and composition of organic solvents adsorbed on surface through the solvatochromic dye and spectrally-resolved super-resolution microscopy (SR-SRM). Unlike traditional measurement where the dyes' spectra are measured in bulk solution, our microscopy measurement gives spatial and spectral mapping of the adsorbed layers on surface.

Upon exposure to a liquid or vapor, a solid substrate quickly picks up molecularly thin adlayers that often dominate its surface behavior. For instance, the adsorption of airborne hydrocarbons readily converts an initially hydrophilic metal, semiconductor, or graphene surface into a hydrophobic one within hours[93–96]. Understanding the nature of such adlayers is of utmost importance in addressing the chemistry and physics of both the adsorbate and the substrate, and is thus key to wide-ranging applications from semiconductor fabrication to atmospheric sciences and crude-oil production[95,97–99].

However, it remains a challenge to elucidate the microscopic structure and composition of adlayers. Atomic force microscopy (AFM) and related scanning-probe techniques have been employed to probe adlayer structure[99–102], but are challenging for small-molecule adlayers that only weakly adhere to the surface. Our previous efforts on graphene templating partly overcome this issue, but the influence of graphene-sample interaction is difficult to assess[103–105].

Recent advances in super-resolution fluorescence microscopy (SRM)[78,106], including those based on single-molecule imaging, provide noninvasive, optical means to achieve nanoscale spatial resolution. Although originally developed for biology, SRM has proven valuable for non-biological soft-matter and surface systems[107–112]. The recent integration of spectral measurement with SRM further enables multidimensional imaging[1,4,35,36,81,82]. In particular, with spectrally resolved STORM and PAINT (SR-STORM/SR-PAINT), we have demonstrated four-color SRM[35] and revealed compositional heterogeneity in cell membranes[1].

Here we develop a general approach to probe the nanoscale structure and composition of weakly adhered organic adlayers via spectrally resolved SRM. By recording the images and emission spectra of $\sim 10^6$ individual solvatochromic fluorescent molecules that turn fluorescent in the adlayer phase, we optically achieve $\sim$30 nm spatial resolution for the adlayers with concurrent detection of local chemical polarity. Consequently, we reveal how the nanoscale adlayer structure on a glass surface varies as a function of chemical polarity for 8 different solvents, and discover that a solvent mixture spontaneously decomposes into nanodroplets of varying compositions and sizes on the surface.

3.2 Result and discussion

We employed Nile Red, a polarity-sensitive solvatochromic fluorophore[42] that is effectively non-fluorescent in water but strongly fluorescent in organic phases[90], to achieve SR-PAINT for adlayers of small organic molecules on a glass surface. By illuminating the sample with a total internal reflection (TIR) configuration to excite a depth of $\sim$100 nm from the glass surface, we found that the stochastic insertion of individual Nile Red molecules from an aqueous imaging buffer into the adlayers led to bursts of single-molecule fluorescence with low background (Figure 8a-c). Due to the extreme thinness of the adlayers (a few nanometers; below), single molecules rapidly diffused in (strongly fluorescent) and out (non-fluorescent) of the adlayer. This short timeframe left little chance for lateral diffusion. Consequently, single-molecule fluorescence appeared as diffraction-limited spots with minimal motion blur (Figure 8bc).

The resultant single-molecule fluorescence was split for concurrent recording of position and spectrum in the wide field (Figure 8a)[1,35]. Figures 1b and 1c each show a small region of a single camera frame (9 ms integration) of the recorded data, for adlayers of trichloroethylene (TCE; Figure 8b) and chloroform (Figure 8c), two common organic solvents of contrasting polarity. Similar single-molecule spectra were observed for the same adlayer, whereas a notable redshift was observed for the more polar chloroform (Figure 8d), consistent with

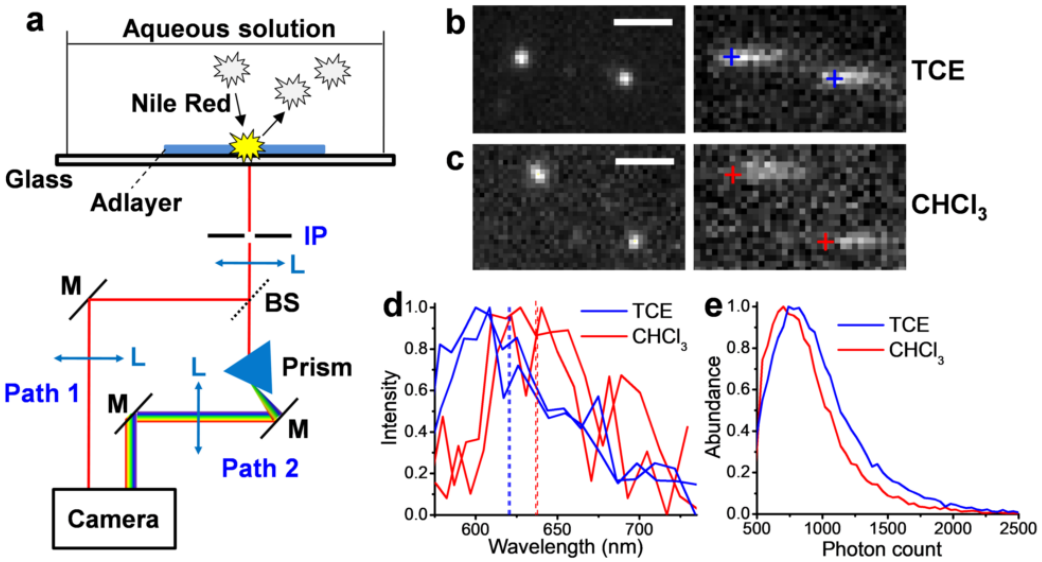

Figure 8: Spectrally resolved super-resolution microscopy of small-molecule adlayers. (a) Experimental setup. The stochastic insertion of individual Nile Red molecules from an aqueous solution into the TIR-illuminated adlayers leads to bursts of single-molecule fluorescence, which is split into two light paths for concurrent recording of the position (Path 1) and the spectrum (Path 2) of each molecule in the wide field. IP: intermediate image plane. L, lens; BS, beam splitter; M, mirror. (b) A small region of the concurrently acquired images (left) and spectra (right) of two single Nile Red molecules inserted into TCE adlayers, obtained in a 9-ms snapshot. Crosses indicate the mapped spectral positions of 590 nm for each molecule. Scale bar is 2 μm. (c) Results of chloroform adlayers. Scale bar is 2 μm. (d) Spectra of the four single molecules in b and c. Dash lines give the spectral mean of each spectrum. (e) Distribution of photon counts in the image channel for single Nile Red molecules in typical data of TCE (blue; average is 984 photons) and chloroform (red; average is 896 photons) adlayers.

the solvatochromic behavior of Nile Red[90,113]. Statistics of the single-molecule fluorescence intensity in the image channel gave asymmetric single-peak distributions (Figure 8e) characteristic of typical STORM, PAINT, and other single-molecule experiments[1,80,114], and the averaged counts were ~900 photons. By integrating the recorded positions and spectra of millions of single molecules over different frames, we mapped out both the morphology and polarity of the adlayers at the nanoscale.

3.2.1 Trichloroethylene and chloroform adlayers

To present the spectral and spatial information of every detected molecule in one image, we calculated the intensity-weighted average of wavelength for each single-molecule spectrum (dash lines in Figure 8d), and used this spectral mean value to assign a color on a continuous scale when plotting the position of each molecule, hence "true-color" SRM images[35]. To cover the spectral behavior of the different adlayers examined in this work, we mapped a spectral range of 616-645 nm to a violet/blue to orange/red color scale (Figure 9, 10 and SI in ref[2]).

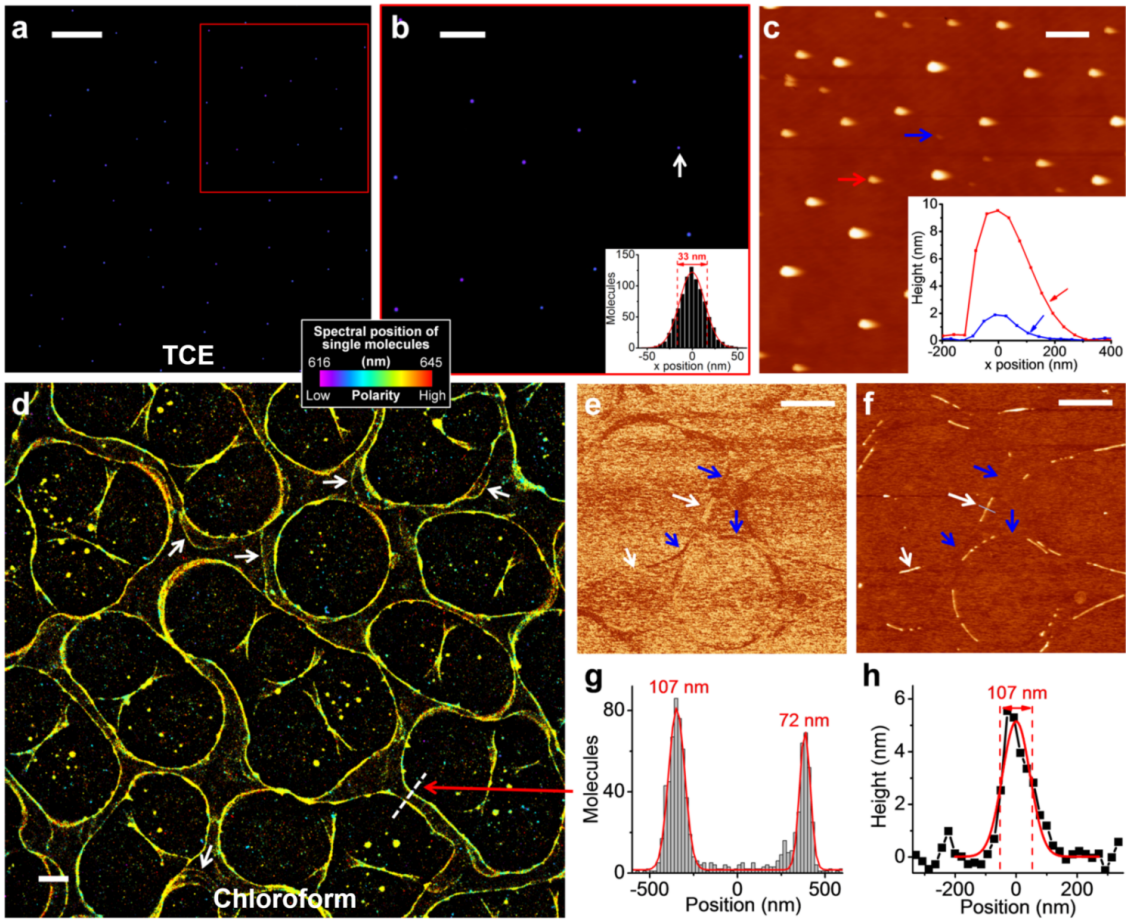

Figure 9: Spectrally resolved super-resolution results of TCE and chloroform adlayers. (a) True-color SR-PAINT image of TCE adlayers, color-coded according to the spectral mean values of single Nile Red molecules, hence an indicator of local polarity (color bar). Scale bar is 5 μm. (b) Zoom-in of the red box in a. Inset: intensity profile for the smallest droplet identified (white arrow). Gaussian fit gives a FWHM width of 33 nm. Scale bar is 2 μm. (c) Soft tapping-mode AFM image of TCE adlayers. Inset: height profiles of two droplets pointed to by the red and blue arrows. Arrows in the profiles point to asymmetry due to dragging. Scale bar is 1 μm. (d) True-color SR-PAINT image of chloroform adlayers, on the same color/polarity scale as a and b. White arrows point to features between parallel edges. Scale bar is 2 μm. (e-f) Soft tapping-mode AFM phase (panel e) and height (panel f) images of the same sample. White and blue arrows point to parts of adlayers that were only visualized in the height and phase images, respectively. Scale bars: 2 μm. (g) Intensity profile along the white dash line in d, crossing two parallel edges. Gaussian fits give 107 and 72 nm for the FWHM widths of the two edge lines, respectively. (h) Height profile for the adlayer pointed to by the white arrow at the center of f. Gaussian fit gives a FWHM width of 107 nm.

In the resultant true-color SR-PAINT SRM images, TCE adlayers consistently appeared as violet-blue colored circular nanodroplets that randomly scattered across the surface (Figure 9a-b and SI in ref[2]). The nanodroplets were often $<\sim$100 nm in diameter (Figure 9a-b), significantly smaller than the optical diffraction limit ($\sim$300 nm), although larger ones up

to several hundred nanometers were also observed (SI in ref[2]). The smallest nanodroplets had apparent sizes of ∼33 nm in FWHM (full width at half maximum) (Figure 9b inset), limited by our image resolution. While the ∼900 photons we detected per molecule (Figure 8e) could theoretically translate to a single-molecule localization precision of ∼17 nm in FWHM[10,115], experimentally a ∼30 nm FWHM localization precision has been found under similar settings[1,86] due to imperfections of the imaging system including pixel nonuniformity and mechanical instability[116]. Deconvolution of this precision/resolution from our SR-PAINT data implies that the true sizes of these smallest nanodroplets were <20 nm.

Markedly different spectral and structural characteristics were observed in the SR-PAINT data of the more polar chloroform. Adlayers appeared yellow on the same spectral scale, indicating higher polarity, and were self-organized into circular networks ∼5 μm in diameter across the substrate (Figure 9d and SI in ref[2]). Edges of the networks were ∼100 nm in width, again significantly below the diffraction limit of conventional optical methods, and often appeared as parallel pairs at ∼1 μm separation (Figure 9g), suggesting a mechanism in which initially ∼1 μm wide adlayer strips gradually dewet into ∼100 nm-wide lines along their two edges. Accordingly, additional residual adlayers were occasionally observed between the parallel edges (white arrows in Figure 9d).

We note that the adlayers were stable with the application of the imaging buffer necessary for our SR-PAINT approach. Among the different adlayers investigated in this work, we found that the TCE droplets could be directly observed by differential interference contrast (DIC) microscopy, albeit at much reduced resolution (∼600 nm) (SI in ref[2]). Adding the imaging buffer did not alter the adlayer structure (SI in ref[2]). Through SR-PAINT, we further confirmed the adlayer nanostructures of both TCE and chloroform to be stable in the imaging buffer over hours, in terms of both nanoscale structure and polarity (SI in ref[2]). The observed high structural stability may be due to the known enhanced adlayer-substrate interactions at the nanoscale, as manifested by drastically reduced contact angles found in previous studies[104,117] and below.

We have compared PAINT results obtained with another dye, Merocyanine 540, which is also characterized by a substantial increase in fluorescence in the organic phases when compared to the aqueous phase[118]. Comparable adlayer structures were observed (SI in ref[2]). However, when compared to Nile Red, Merocyanine 540 exhibits minimal shifts in emission spectrum for solvents of different polarities[118] (SI in ref[2]), and so is not useful for revealing local polarity. Nonetheless, the consistency of results from different dyes indicates that the choice of fluorescent probe has no impact on the image generation process.

We next compared results with AFM acquired in the dry state in air. Soft tapping mode using a probe of low (∼5 $N \cdot m^{-1}$) force constant visualized structures consistent with our SRM results, but strong disturbances to the adlayers were apparent. Specifically, for the TCE adlayers, asymmetric droplet shapes were observed along the scanning direction (Figure 9c), indicative of dragging by the scanning tip. Such artifacts from tip-adlayer interactions8 became more severe when scanning at high magnifications, and so the shape of the smaller (<∼50 nm) droplets was difficult to determine (SI in ref[2]). Typical heights of the nanodroplets were a few nanometers (Figure 9c inset), thus indicating very flat ge-

ometries with contact angles of $<\sim 10^{\circ}$, consistent with the known behavior of adsorbed nanodroplets[105,117]. For the chloroform adlayers, AFM showed fragmented adlayer structures so that the circular networks were, intriguingly, only partly visualized in either the phase (Figure 9e) or the height (Figure 9f) images in a complementary fashion (blue and white arrows), again signifying problems due to tip-adlayer interactions. For regions where height data appeared normal, the network edges were ∼100 nm in width (Figure 9h), consistent with SR-PAINT results (Figure 9g), and a few nanometers in height, again indicating flat geometries. Tapping mode with a standard probe (~ 48 N·m^{-1}) gave reduced adlayer contrast, whereas in contact mode, the AFM tip severely dragged the adlayers along, and so no adlayers were visualized for either TCE or chloroform (SI in ref[2]).

3.2.2 Dependence of adlayer spectral and structural properties on solvent polarity

The contrasting spectral and structural characteristics of TCE and chloroform adlayers revealed by SR-PAINT prompted us to investigate whether universal structural and polarity trends can be established. We thus next examined adlayers of 6 more common solvents, namely tetrahydrothiophene, ethyl acetate, dichloromethane, nitroethane, nitromethane, and ethyl acetoacetate (EAA) (Figure 10a-e and SI in ref[2]). Together with the above-discussed data of TCE and chloroform (Figure 9a,b,d and SI in ref[2]), we found that the single-molecule spectra of Nile Red at different adlayers were largely uniform within adlayers of the same liquid, but redshifted for higher solvent polarity. Plotting the averaged spectral means for single molecules at the different adlayers as a function of the relative polarity of the liquids showed a near-monotonic trend (Figure 10f). These results indicate that the polarity of the adlayers is well correlated with that of the bulk liquid.

Remarkable polarity-dependent trends were also found for adlayer morphology at the nanoscale. The two low-polarity liquids, TCE and tetrahydrothiophene, both showed up as zero-dimensional (0D) nanodroplets across the surface (Figure 9a, 9b, 10a, SI in ref[2]). With increased polarity, adlayers of chloroform and dichloromethane both appeared as intertwined networks of one-dimensional (1D) nano-lines (Figure 9d, 10c, SI in ref[2]). With polarity in between the above two cases, ethyl acetate gave nanoclusters of in-between morphology (Figure 10b and SI in ref[2]). Liquids of relatively high polarity -namely, nitroethane, nitromethane, and EAA, spread well to form large domains of two-dimensional (2D) films micrometers to tens of micrometers in size (Figs. 3d-e and SI in ref[2]). Our results hence establish a model in which adlayer dimensionality at the nanoscale gradually increases with polarity on the hydrophilic glass surface.

We again compared AFM results. Although soft tapping-mode AFM performed adequately for ethyl acetate (SI in ref[2]), it did not visualize any dichloromethane adlayers (SI in ref[2]). This result may be attributed to the very low boiling point of dichloromethane (39.6 °C); the adlayers may thus be too fragile to be probed by an AFM tip. Meanwhile, nitromethane adlayers were barely visible in AFM due to their very small height (∼1 nm) and

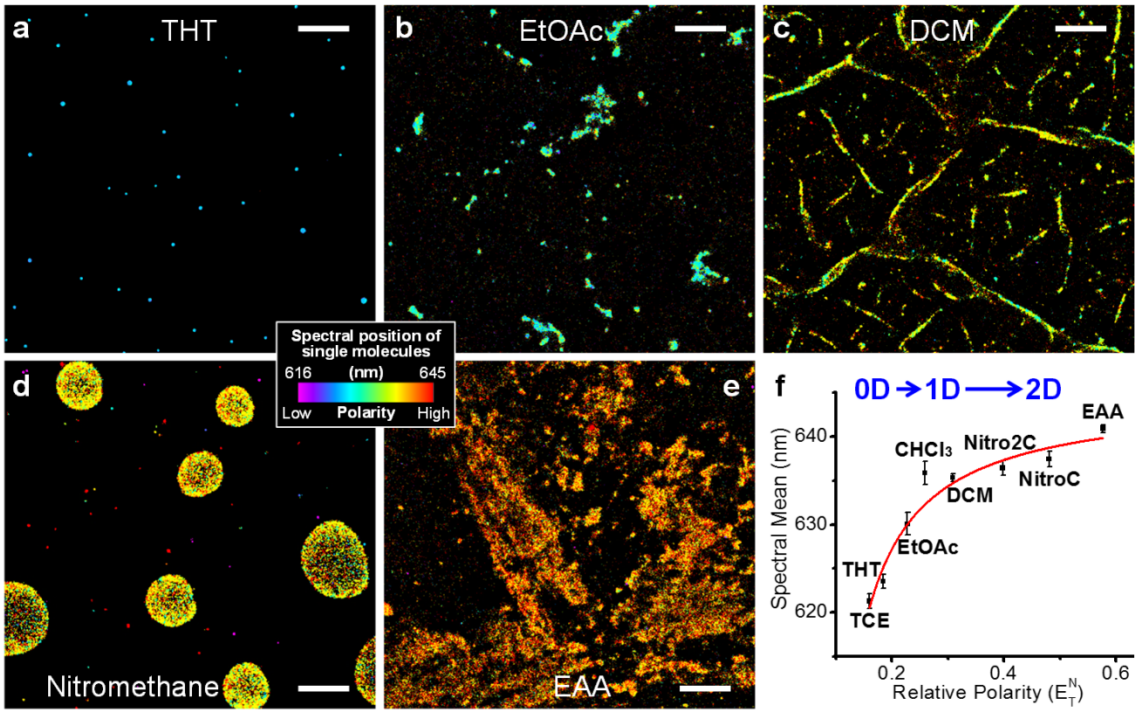

Figure 10: Dependence of adlayer spectral and structural properties on polarity of the liquid. (a-e) True-color SR-PAINT images of adlayers of tetrahydrothiophene a, ethyl acetate b, dichloromethane c, nitromethane d, and EAA e. Images were color-coded according to the spectral mean values of single Nile Red molecules, on the same spectral/polarity scale as Figure 9. Scale bars: 2 μm. (f) Measured spectral mean values of the adlayers versus the relative polarity (normalized Dimroth-Reichardt ET scale30) of the liquids. THT: tetrahydrothiophene; EtOAc: ethyl acetate; DCM: dichloromethane; Nitro2C: nitroethane; NitroC: nitromethane. Each data point is averaged from 9-12 areas of 3-6 different samples, with standard deviations drawn as error bars. Red curve is a guide to the eyes.

tip-adlayer interactions (SI in ref[2]). Overall, our AFM results, acquired in the dry state in air, were generally consistent with our PAINT SRM results, although tip-sample interactions often obscured nanoscale structural features visualized by PAINT.

3.2.3 Spontaneous nanoscale demixing of a two-component mixture

The distinct spectra we resolved in SR-PAINT for adlayers of different liquids suggest a mechanism to distinguish nanoscale adlayers of unknown compositions, e.g., those formed from mixtures. Remarkably, by immersing a glass surface in a 1:3 well-mixed solution of TCE and chloroform, two liquids miscible in bulk, the resultant adlayers showed up as a palette of different colors and nanoscale structures in SR-PAINT images (Figure 11a,b and SI in ref[2]; note that colors are mapped to a narrower spectral range of 620-638 nm). Overall, adlayers appeared as both isolated, large (dia. ~200 nm) nanodroplets of bluer spectra, and smaller

(<100 nm), redder droplets that were arranged into fragmented networks. Both the sizes of the droplets and the separations between the droplets were often substantially smaller than the diffraction-limited resolution of conventional light microscopy (Figure 11b inset). The large nanodroplets had averaged single-molecule spectra that matched well to adlayers of pure TCE (Figure 11c). In the other limit, the reddest small nanodroplets exhibited single-molecule spectra that agreed with that of adlayers of pure chloroform (Figure 11c). Meanwhile, a majority of the small nanodroplets showed intermediate spectra (Figure 11c), suggesting varying compositions. These results indicate that although we started with a well-mixed solution, TCE and chloroform spontaneously demixed on the glass surface to form adlayer nanodroplets of different compositions. Although the nanoscale demixing of miscible liquids has been reported in confined systems[119,120], related effects for surfaces are usually discussed within the context of the dewetting of films[121–123]. The unique capability to resolve local compositions allowed us to reveal nanoscale demixing in surface adlayers.

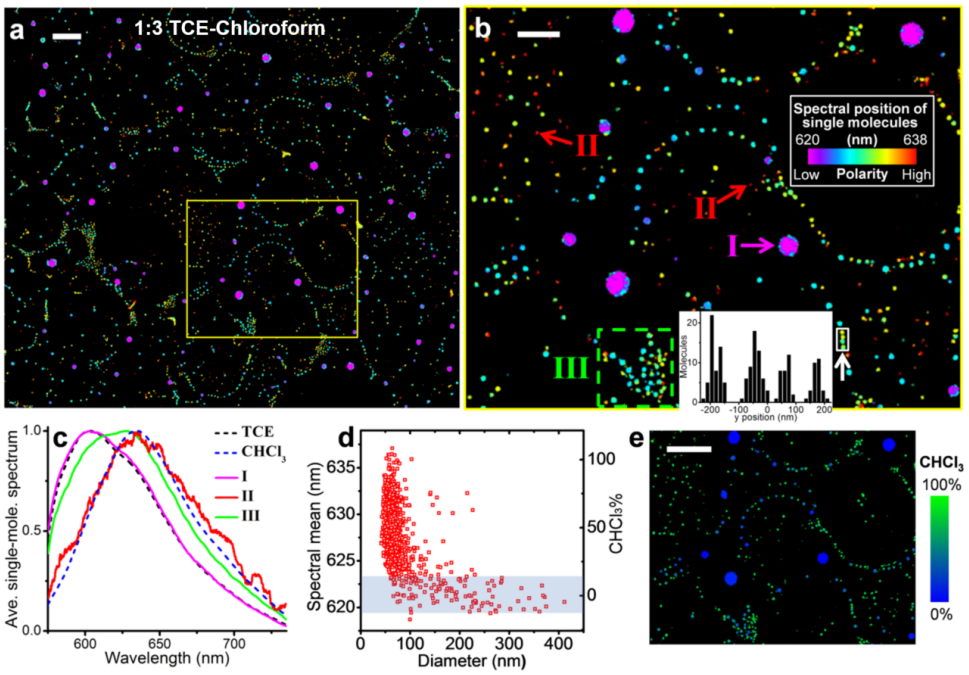

Figure 11: Nanoscale decomposition of a two-component mixture on the surface. (a) True-color SR-PAINT image of adlayers from a 1:3 mixture of TCE and chloroform, drawn on a spectral scale of 620-638 nm. Scale bar is 2 μm. (b) Zoom-in of the yellow-boxed area in a. Inset: intensity profile along the vertical (y) direction for the four closely located nanodroplets marked by the white box. Scale bar is 1 μm. (c) Averaged single-molecule spectra obtained for Regions I (large nanodroplets), II (the reddest small nanodroplets), and III (small nanodroplets with varying color) in b (solid lines), compared to that of adlayers of pure TCE and chloroform (dash lines). (d) Averaged spectral mean value (left y-axis) and corresponding chloroform percentage (right y-axis) of each droplet, as a function of droplet size. Shaded band represents the typical range of nanodroplets of pure TCE adlayers. (e) Recoloring of b by the estimated chloroform percentage of each nanodroplet. Scale bar is 2 μm.

To quantify the composition of every adlayer nanodroplet, we calculated the averaged

spectral mean value for all detected single molecules within each nanodroplet. Plotting this result as a function of the size of the nanodroplets (Figure 11d), both of which were uniquely delivered by SR-PAINT, indicated that most droplets $>\sim$100 nm in diameter had averaged spectra similar to pure TCE adlayers. For the smaller droplets, a very limited fraction attained spectra comparable to that of adlayers of pure chloroform, whereas the others showed a continuous distribution of wavelengths between the two limits. Using a simple linear interpolation (secondary y-axis of Figure 11d), we directly converted the averaged spectral position of each nanodroplet to its mole fraction of chloroform, thus facilitating simultaneous visualization of the nanodroplet composition, size, and location (Figure 11e).

The scattered distribution of large nanodroplets of $\sim$100% TCE is similar to results on adlayers due to pure TCE (Figure 9a-b). Meanwhile, the smaller nanodroplets, with varying fractions of chloroform, were arranged into ring-like network patterns that are reminiscent of adlayers of pure chloroform (Figure 9d), albeit here the networks were broken into nanodroplets. These intriguing results, wherein adlayer composition correlates strongly with the droplet size and location, point to an intricate local balance and/or competition between the vapor pressures and surface interactions of TCE and chloroform at the nanoscale.

We further examined the influence of mixture composition by varying the ratio of TCE and chloroform in the starting solution (Figure 12). For adlayers of a 1:1 TCE-chloroform mixture (Figure 12ab), fewer high-polarity droplets were observed when compared to the adlayers of the 1:3 TCE-chloroform mixture (Figure 11), and small, intermediate-polarity droplets surrounded large low-polarity droplets as opposed to forming fragmented networks. This result is consistent with the lower chloroform concentration in the starting mixture: the vapor pressure of chloroform is 3-fold higher than TCE at room temperature, so it evaporates away faster during adlayer formation. In contrast, for adlayers of a 1:6 TCE-chloroform mixture (Figure 12cd), the low-polarity large droplets disappeared, and segments of nanolines interspersed with small droplets, consistent with the higher chloroform content of the starting mixture. Together, our results on adlayers of different starting mixtures showed trends consistent with the expected physical properties of the two solvents, but uniquely revealed the remarkable evolution of nanoscale structures and composition distributions of this system.

3.3 Conclusion

By recording the fluorescence spectra and positions of millions of single solvatochromic molecules that turn fluorescent in the organic phase, our SR-PAINT approach uniquely allowed for the nanoscale visualization of the morphology and composition of weakly bound adlayers of small organic molecules. Through examination of 8 different molecules, we first established general trends for how adlayer geometry/dimensionality evolves as a function of molecular polarity. Although corresponding AFM results can be interpreted as consistent with our SR-PAINT data, tip-adlayer interactions often disturbed the sample and led to incomplete visualization of the adlayers. The morphology information alone also did not

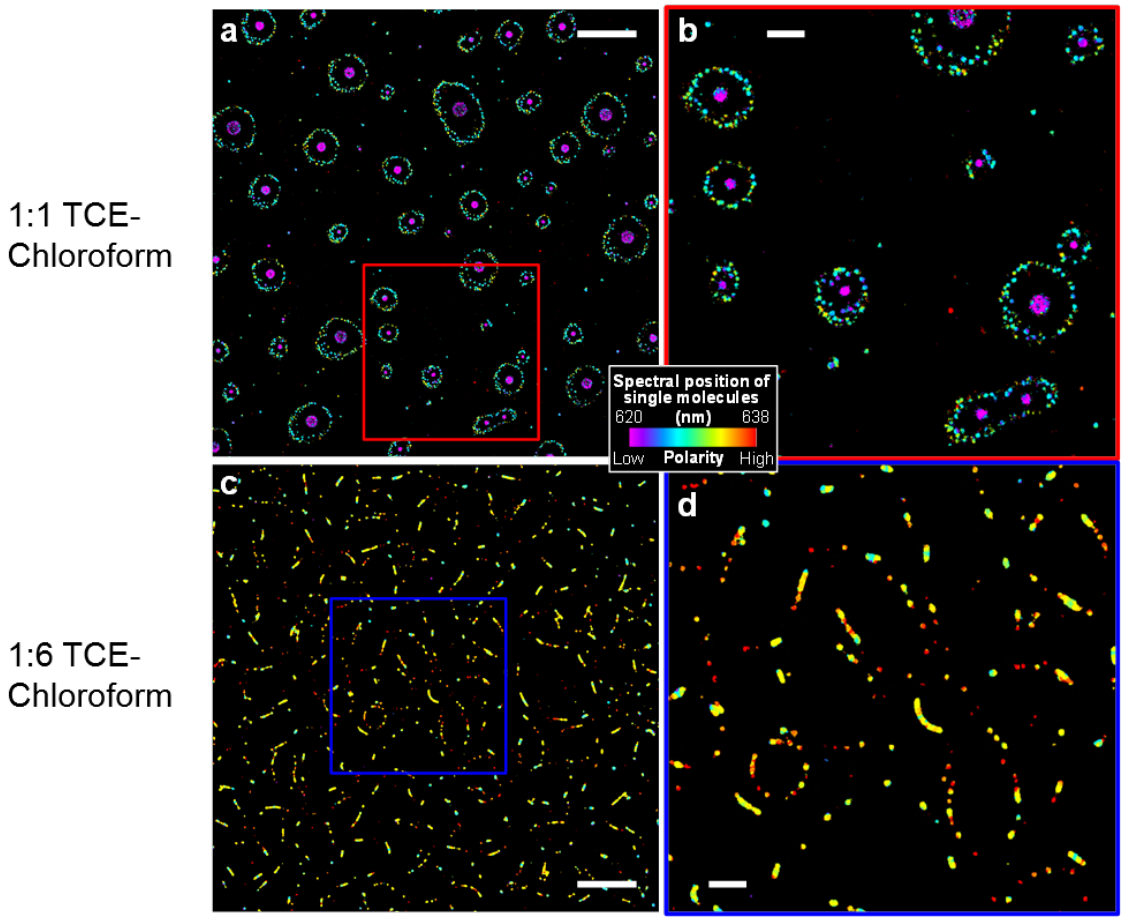

Figure 12: SR-PAINT reveals the effect of mixture composition on adlayer structure and composition for the TCE-chloroform system. (a-b) True-color SR-PAINT images of adlayers from a 1:1 TCE-chloroform mixture. b is a zoom-in of the red box in a. (c-d) True-color SR-PAINT image of adlayers from a 1:6 TCE-chloroform mixture. d is a zoom-in of the blue box in c. Scale bars: 4 μm (a,c) and 1 μm (b,d).

lend confidence to whether all observed structures were due to adlayers. In contrast, with SR-PAINT, we detected uniform single-molecule spectra for adlayers of the same solvent, as well as consistent spectral redshifts for the more polar solvents, thus confirming the identity of the observed structures while also showing that the adlayer polarity is well correlated with that of bulk solvent.

Taking this unique spectral information to the next level, we examined adlayers from a solvent mixture, and revealed that for the miscible TCE-chloroform system, in adlayers the two solvents spontaneously demix into nanodroplets of varying compositions. Notably, the composition correlated strongly with droplet size and location, thus pointing to rich interactions between different factors in determining how adlayers are formed from solvent mixtures. While such capabilities are immediately powerful for probing adlayers due to different chemical and physical processes (e.g., our preliminary results on the influence of

mixture composition on adlayer morphology and composition; Figure 12), our spectrally resolved SRM approach also opens the door to the nanoscale structural and functional interrogation of other similarly challenging surface and soft-matter systems inaccessible to current methods.

3.4 Materials and method

Materials and sample preparation

Trichloroethylene (TCE) (99%), tetrahydrothiophene (98%), nitroethane (98%), nitromethane (98%), ethyl acetoacetate (EAA) (99%), and glycine (99.5%) were from Alfa Aesar. Chloroform (99.8%) was from BDH Chemicals. Dichloromethane (99.5%) was from Sigma-Aldrich. Ethyl acetate (99.9%) was from Fisher Chemical. Nile Red (99%, Acros Organics) was dissolved in dimethyl sulfoxide to form a 3 mM stock solution and kept at $-20\,^{\circ}\mathrm{C}$. Glass coverslips (25 mm circle, VWR) were cleaned with a heated piranha solution (75% sulfuric acid and 25% hydrogen peroxide), and then rinse with Milli-Q water, thus rendering a highly hydrophilic surface. After blown dry with nitrogen, the coverslip was immersed into a chosen liquid for 3 hr, and then let dry in air.

Optical setup

SR-PAINT SRM experiments were performed on a home-built setup (Figure 8a) based on a Nikon Ti-E inverted fluorescence microscope. A 561-nm laser (Coherent) was introduced onto the back focal plane of an oil-immersion objective lens (Nikon CFI Plan Apochromat λ 100x, NA 1.45) via a dichroic mirror (ZT561rdc, Chroma). A translation stage shifted the laser beam toward the edge of the objective so that emerging light reached the sample at an incidence angle close to the critical angle of the glass-water interface to achieve total internal reflection (TIR) wide-field illumination. Emission was filtered by a long-pass (ET575lp, Chroma) and a short-pass (FF01-758/SP, Semrock) filter, and then cropped at the image plane of the microscope camera port to a width of $\sim$4 mm. The cropped intermediate wide-field image was collimated by an achromatic lens (f = 80 mm) and then split into two perpendicular paths with a 50:50 beam splitter (BSW10, Thorlabs). In Path 1, emission was focused by an achromatic lens (f = 75 mm) onto one-half of an EM-CCD (electron-multiplying charge-coupled device) camera (iXon Ultra 897, Andor) to achieve an effective magnification of $\sim$94x for wide-field recording of single-molecule images. In Path 2, emission was dispersed by an equilateral calcium fluoride prism (PS863, Thorlabs) and then focused by an achromatic lens (f = 60 mm) onto the other half of the EM-CCD to generate spectra of the same single molecules in the wide field. Wavelength calibration was performed by using fluorescent beads and narrow bandpass filters[35]. Briefly, 100-nm diameter, four-color fluorescent beads (T7279, Life Technologies) were adsorbed to a glass coverslip at low density, and imaged on the setup with 405 nm, 560 nm, or 647 nm excitation. Beads appeared as diffraction-limited spots in Path 1, and as dispersed 1D spectra in Path 2. Bandpass filters

with ∼10 nm bandwidth were used to determine the spectral positions of different known wavelengths in Path 2 relative to the bead positions in Path 1.

SR-PAINT imaging of adlayers

The coverslip sample was immersed in a 10 mM glycine buffer solution (pH = 9.4) containing ∼3 nM Nile Red, and was continuously illuminated with the 561 nm laser under the abovementioned TIR configuration at an intensity of ∼2 $kW \cdot cm^{-2}$. The stochastic insertion of individual Nile Red molecules from the imaging buffer into the adlayers led to transient bursts of single-molecule fluorescence, whereas the background signal was low due to the very low quantum yield of Nile Red in water and the TIR illumination. Single-molecule fluorescence bursts usually switched off within the same camera frame they appeared, as the Nile Red molecules returned to the aqueous phase or were photobleached. Single-molecule fluorescence emission was concurrently recorded in the wide-field as non-dispersed images (Paths 1) and dispersed spectra (Path 2) (Figs. 1a-c). Sparsity of single-molecule fluorescence was achieved by adjusting Nile Red concentration in the imaging buffer to avoid signal overlapping between molecules. The EM-CCD recorded continuously at 110 frames per second (integration time: 9 ms per frame) for a frame size of 512x256 pixels [256x256 pixels for wide-field single-molecule images (Path 1) and spectra (Path 2), respectively], and typically collected 20,000-40,000 frames (3-6 min) for each experiment. ∼900 photons were collected for each molecule in the image channel (Figure 8e), and the typical signal-to-noise ratio is >25 for each molecule. To correlate the spatial and spectral positions of Path 1 and Path 2, a narrow bandpass filter centered at 590 nm (FF01-590/10, Semrock) was placed before the beam splitter for ∼5,000 frames. Correlation of the single-molecule images in Path 1 and the 590 nm-filtered single-molecule spectral images in Path 2 generated a mapping function between the two channels. Using this mapping function, the super-localized positions of single molecules in Path 1 were projected to the coordinates of Path 2. Single-molecule spectra were obtained through the mapped position of 590 nm and the aforementioned calibration curve. The intensity-weighted average of wavelengths for each single-molecule spectrum was taken as the spectral mean. This value was used to assign the color to the single molecule based on a continuous color scale, hence "true-color" super-resolution images.

AFM characterization

Unless otherwise noted, AFM images were taken in the dry state in air on an Asylum MFP-3D system in soft tapping mode using aluminum-coated probes (Tap150Al-G; BudgetSensors). Nominal values of the force constant, resonance frequency, and tip radius were 5 $N \cdot m^{-1}$, 150 kHz, and <10 nm, respectively. No attempts were made to deconvolve the tip geometry in the presented data. SI in ref[2] Fig. 5d-f were taken in contact mode using the same probes. SI in ref[2] Fig. 5a-c were taken under standard tapping mode using a probe with a nominal force constant of 48 $N \cdot m^{-1}$ (PPP-NCL-50; NANOSENSORS).

Chapter 4

Information-rich localization microscopy through machine learning

4.1 Introduction

In the previous chapters, I discuss how we use multidimensional single-molecule localization microscopy (SMLM) to sample diverse biogically and chemically relevant information at the nanoscale. The spectral dimension can be easily obtained through spectrally-resolved super-resolution microscopy we developed, and often related to chemical/biological environments of the system. When combined with environment-sensitive dyes, intracellular heterogeneity in the local chemical environment can be mapped with few tens of nm resolution[1]. Similarly, I presented how we characterized the structure, compositional heterogeneity, and demixing behavior of weakly bound organic adlayers on glass surface[2].

To date, to extract information beyond the in-plane location, e.g., the emission wavelength and the axial position, of single emitters, would often oblige the explicit encoding of such high-dimensionality information into the diffraction pattern of single molecules (point spread functions; PSFs) through optical aberrations and alterations[4,124], including astigmatism[25], interference[125], wavelength-dependent splitting[29], dispersion[35], and wave-front modification[126]. The resultant, engineered PSF shape and intensity then help establish best-fit models between experimental observables and fluorophore characteristics. Such approaches, each often optimized for a single parameter of interest, inevitably increase the PSF size and/or necessitate the splitting of fluorescence across different channels, and so often incur complicated optics and compromised performances between different parameters. While recent work[127,128] has studied the PSF design for the simultaneous estimation of color and

axial position, added optics and enlarged PSFs are still involved, and proper calibration of such Fourier optics-heavy systems is challenging[129].

We reason that even the simplest PSF obtained from an unmodified microscope is rich in information—in addition to the axial location embedded in the defocused PSF, which has been examined in recent work[130,131], the emission wavelength of a fluorophore also sets the scale of PSF in all three dimensions[132]. Contributions from the two sources are distinct yet subtle, and would be hard to decouple via simple models given the difficulties in fully characterizing all system-specific properties. Although recent work[131,133] leveraging spline models may help account for the subtleties in realistic PSF images and thus potentially decipher this extra information, the construction of such models usually requires "ideal" reference PSF stacks, e.g., bright fluorescent beads of precisely determined 3D positions (see our analysis in Figs. 1 and 2 below).

In this work, we present a data-driven approach in which the relationship between a PSF image, obtained from an unmodified commercial microscope, and the underlying multidimensional characteristics of an emitter is directly established by a supervised machine learning algorithm. A related approach has been recently used in astronomy for stellar classification[134]. Although SMLM faces additional challenges associated with the vast range of axial positions (as opposed to stars always at infinity), it benefits from the ready access to arbitrary amounts of experimental PSFs that may be acquired under identical conditions, which has motivated several recent works that leveraged deep learning in SMLM[135,136]. By training generic learning models using such datasets, an end-to-end framework from raw, noisy PSF images to the molecule characteristics can be constructed.

4.2 Result and discussion

4.2.1 Construction of color-separating and axial-localization artifical neural networks (ANN)

To demonstrate this concept, we developed a method for machine learning-based 3D multicolor SMLM (Figure 13 and Methods). With typical experimental pixel sizes (∼100 nm), the dimensionality of the PSF images is moderate (modeled as 13x13 pixels), and thus artificial neural networks (ANN) with multiple hidden layers[137] were directly used as our learning model. ANN is beneficial here as it possesses excellent representational power, with no requirement of domain-specific knowledge on the input data to construct nonlinear models. Moreover, as long as a sufficient amount of input training data is provided to the ANN, noise in the data averages out during training process given proper regularization, and ANN eventually manages to extract underlying structures[138]. Consequently, it is well-suited for the limited photon budget and heavy pixelation in SMLM. Finally, ANN training only requires the ground truth of the parameter of interest. Namely, it gradually establishes the relationship between the raw input and the inference target (e.g., color or axial position) in a flexible, end-to-end fashion while being insensitive to other parameters (e.g., x/y position).

In contrast, for approaches in which parametric models are constructed by fitting to "real" PSFs[133,139], experimental images always need to be tied to precisely determined 3D positions. Reference PSFs are thus usually acquired using bright fluorescence beads, which may not accurately represent the PSFs of single molecules in SMLM experiments.

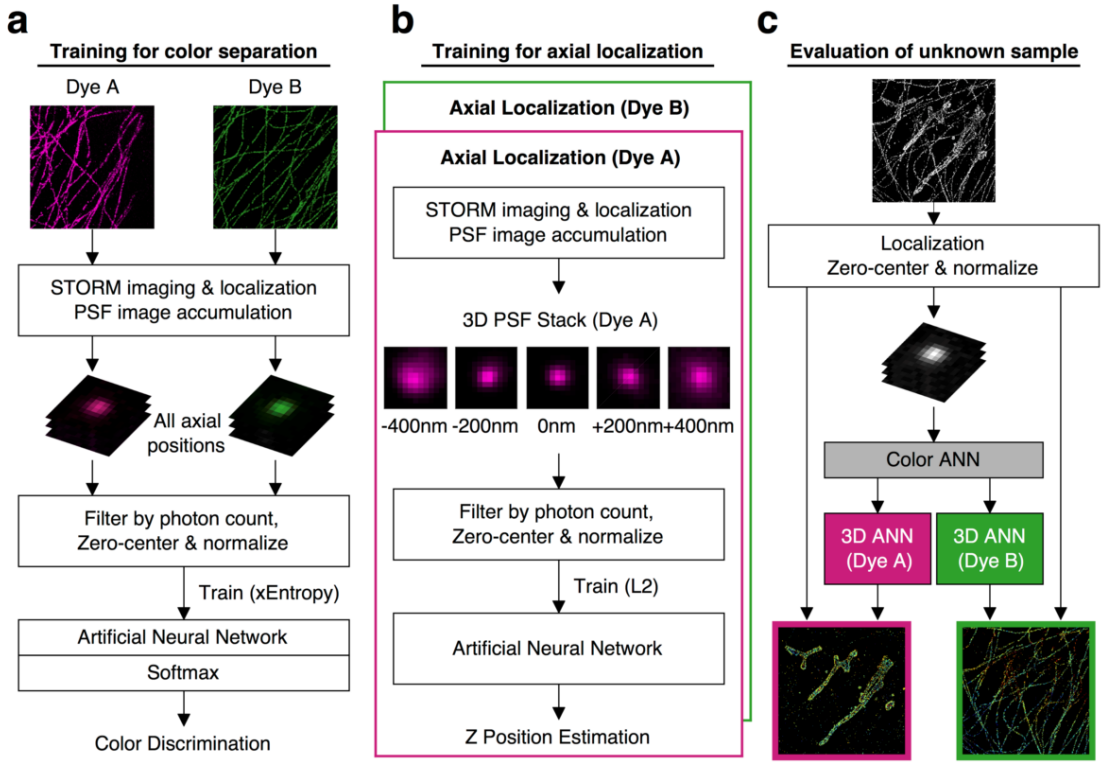

Figure 13: Workflow of the machine learning-based multidimensional SMLM. (a) A color-separating ANN is trained using samples each singly labeled by one known fluorophore, in which PSFs at different axial positions are well-represented. (b) ANNs for resolving the axial position are separately trained for each fluorophore using PSFs of known axial positions. (c) For the analysis of unknown samples, single-molecule images are localized in 2D, and first fed into the color-separating ANN described in (a). The color-separated single-molecule images are then separately fed into the axial-localization ANNs trained with the corresponding fluorophores, as described in (b). The resultant color and axial position information are then combined with the 2D localization of each molecule to generate the final multidimensional SMLM data.

One ANN with a final Softmax layer was first trained using cross-entropy loss to determine the emitter color of each PSF. Once trained, the final Softmax output provided an estimate for the conditional probability distribution of the fluorophore color, which enabled the classification of each PSF image with known confidence (Figure 13a and Methods). For this color-separating ANN, training data for different fluorophores were separately prepared from multiple imaging sessions performed under the same experimental conditions as the final sample, but using only one known fluorophore at a time. The training data contained sufficient samples for fluorophores at different axial positions within the depth of field (∼

±500 nm of the focal plane), so that the ANN was trained to recognize fluorophores for all axial positions.

In parallel, ANNs for resolving the axial position of the emitter were separately trained for each fluorophore using L2 loss so that the final output was a scalar value[140] corresponding to the decoded axial position (Figure 13b). Training data for these axial-localization ANNs were collected by step-scanning samples each containing one specific fluorophore, as is typically performed for the calibration in existing 3D SMLM methods[25].

Once both trainings were completed, SMLM data from unknown samples were localized in 2D, and the single-molecule images were first fed into the above color-separating ANN (Figure 13c). The resultant, color-separated single-molecule images were then separately fed into the above axial-localization ANNs trained with the corresponding fluorophores (Figure 13c). Multidimensional SMLM data were thus obtained by integrating the ANN-inferred color and axial information with the initial 2D-localization results.

4.2.2 Performance of the color-separation ANN

We first examined the performance of the color-separating ANN using simulated yellow (600 nm wavelength) and red (700 nm wavelength) PSFs that account for index discontinuity in the sample area[132] (SI in ref[3]). For comparison, we also modeled the PSF with cubic splines[133], and determined color through maximum likelihood estimation (MLE) by minimizing the likelihood error in the MLE fitting to the PSF stacks of the two different emission wavelengths. For both training the neural networks and the construction of the cubic-spline model, we used a PSF reference stack of 10000 simulated photons over ±600 nm axial (z) range in 20 nm steps. For the analysis of "unknown" PSFs, the PSF was either directly fed to the trained neural networks, or for MLE, fitting was performed twice with negative and positive initial z values, respectively, and the result with a lower likelihood error was selected, so as to overcome the limitation of MLE being sensitive to initial parameters[131]. At a fixed simulated background of 10 photons/pixel, we found that at 5000 simulated photons, both ANN and MLE achieved near-perfect color separation [Figure 14a for accuracy and Figure 15 for root mean square error (RMSE) of the fit]. At 2000 simulated photons (Figure 14b and 15), ANN slightly outperformed MLE for the yellow PSFs, especially for z=0 nm, whereas MLE performed bit better for the red PSFs.

For experiments, we used two types of 40-nm dia. fluorescent beads that differed by 45 nm in emission wavelength ("yellow" and "orange"), and images were acquired over ±400 nm around the focal plane in 50 nm steps (Methods and SI in ref[3]). When the beads were at the focal plane, fitting to simple Gaussian models yielded PSF sizes (2σ) that were directly proportional to the emission wavelength, as expected, and this difference gave adequate separation of the two colors (Figure 14c). However, this separation quickly fell apart when results from different axial positions were mixed: unsurprisingly, defocusing led to substantially increased PSF sizes, and so this parameter no longer offers useable color separation (Figure 14d).

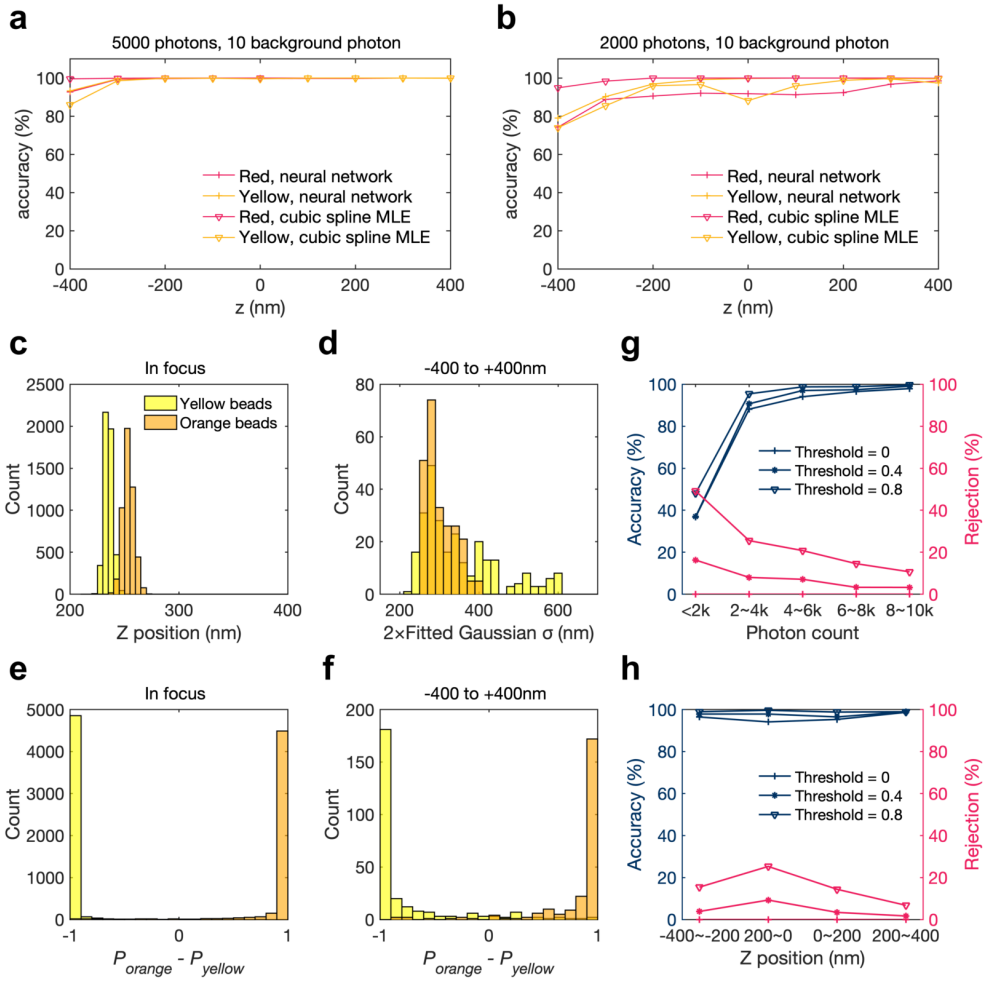

Figure 14: Performance of the color-separating ANN. (a-b) Comparison of the color-separation performance of the ANN and cubic-spline MLE for simulated PSFs of yellow (600 nm) and red (700 nm) point sources with 5,000 (a) and 2,000 (b) emitted photons. (c,d) PSF size (2σ of 2D Gaussian fitting) distributions of experimental images of "yellow" and "orange" beads emitting 4000 photons, when the beads are at the focal plane (c) and as the focus is uniformly scanned over ± 400 nm (d). (e,f) Outputs of the color-separating ANN for the same PSFs in (c,d), presented as the distribution for the differences in the evaluated probabilities of each bead being "orange" vs. being "yellow". (g-h) Accuracy of classification (left axes) and rejection rate (right axes) in the presence of defocusing, as a function of photon count for all z-positions (g) and as a function of z-position for beads brighter than 4,000 photons (h), for confidence thresholds of 0, 0.4, and 0.8.

In contrast, our color-separating ANN recognized the nuances in the PSF patterns due to differences in color vs. differences in axial position, and thus offered excellent color separation both in the absence and presence (± 400 nm range) of defocusing (Figure 14ef). As mentioned, the output of this ANN gives the conditional probabilities of each given single-molecule image being classified as certain types of fluorophores. In the binary yellow-orange system, the results can be simplified as the difference Δ between the evaluated probabilities

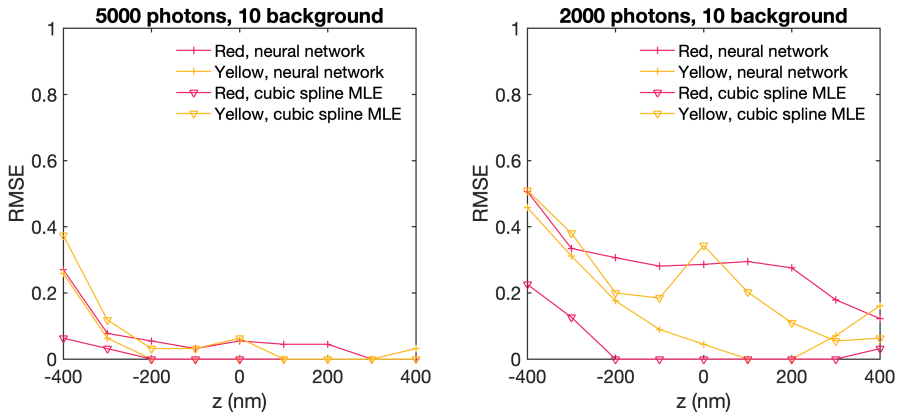

Figure 15: Root mean square error (RMSE) curves for color classification on simulated PSFs. Here RMSE is calculated by assigning +0.5 to "red" and -0.5 to "yellow" PSFs, respectively.

of being orange and being yellow for every image (Figure 14ef). Even in the presence of defocusing, simple classification based on $\Delta > 0$ and $\Delta < 0$ gave excellent identification for beads brighter than 4000 photons (Figure 14fg), with little dependence on the axial position within the ± 400 nm focal range (Figure 14h). Note in STORM experiments, an average of >5000 photons is often obtainable for single molecules[24,25]. Reducing the photon count to the range of 2000-4000 photons led to a decrease in accuracy to 88% (Figure 14g), but this result was improved to 95.4%, by only keeping classifications with $|\Delta|$ above the confidence threshold of 0.8, at the expense of rejecting 25% classifications (Figure 14g). Our ANN approach can thus be tuned for experiments that emphasize color-separation accuracy vs. experiments that emphasize the retention of molecules.

4.2.3 Performance of the axial-localization ANN

We next characterized the axial-localization ANN and compared with MLE results based on cubic-spline PSF models. Results on simulated PSFs of a 700 nm wavelength emitter (Figure 16a-c) showed that both the ANN and cubic-spline MLE results generally followed the trend of the Cramer-Rao lower bound (CRLB), although a somewhat deteriorated performance was found at z=-200 nm for the particular MLE fitter we used. For experimental PSFs acquired with bright fluorescent beads, ANN achieved comparable results as cubic-spline MLE, but showed a lower performance for z=0 nm (Figure 16d-f).

Together, our results showed that ANN achieves good color separation and axial localization for unmodified PSFs, and its performance is generally comparable to the state-of-the-art parametric PSF models. However, for experimental implementation, the construction of ideal parametric PSF models relies on ideally measured PSFs, like those obtained above from bright beads, for which the 3D positions of each PSF can be precisely determined. In comparison, ANN should readily extract the underlying structures from a large number of "non-ideal" PSFs of unknown positions, like single-molecule data from SMLM experiments

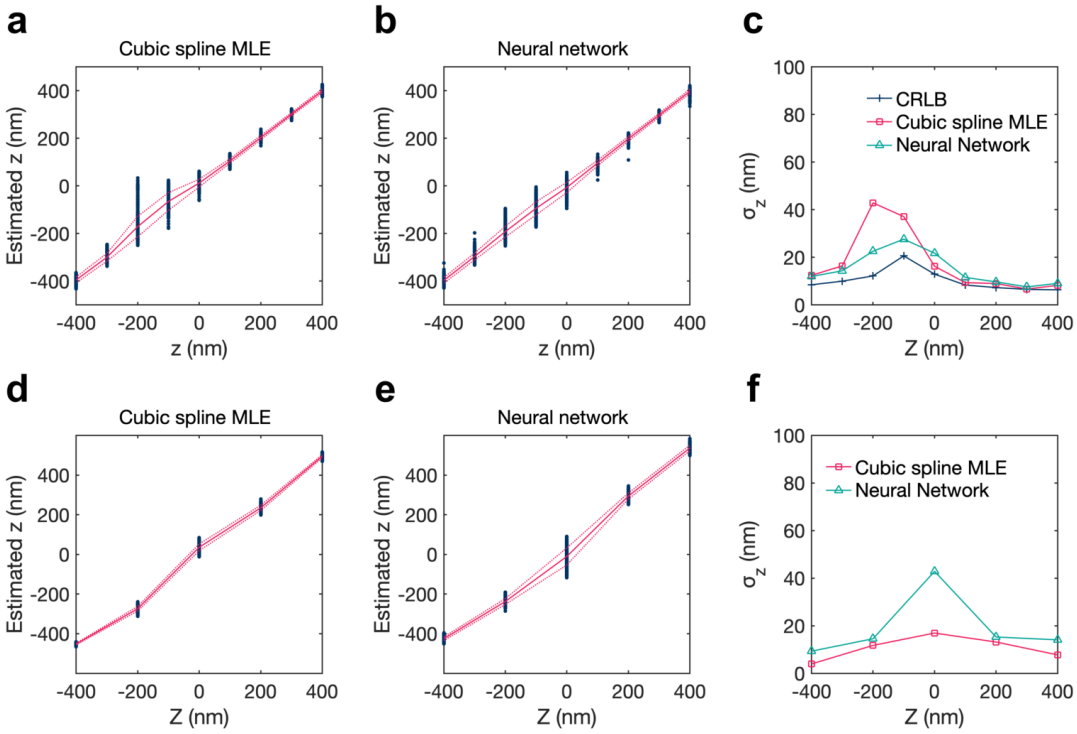

Figure 16: Comparison of the results of the axial-localization ANN with cubic-spline MLE and with the Cramer-Rao lower bound. (a-b) Estimated z positions vs. the ground truth over ±400 nm of the focal center for simulated point sources of 700 nm wavelength at a brightness of 5000 photons, using (a) MLE with a cubic-spline model and (b) ANN estimation. The scattered data points represent estimated z positions at each true z position, and the red solid and dash lines give the corresponding mean and standard deviation. (c) z precision from (a-b), compared with the Cramer-Rao lower bound calculated from the cubic-spline model. (d-f) Corresponding results on experimental images of red fluorescent beads (typical photon count: 15,000).

of cell samples.

4.2.4 Application of ANN to single-molecule localization microscopy of cells

To test this possibility, we immunolabeled the microtubules and the outer membrane of mitochondria in adherent COS-7 cells with two STORM dyes, CF568 and Alexa Fluor 647 (AF647). Both dyes were excited within the same STORM imaging session, and resultant single-molecule fluorescence was collected in one single optical path after a multi-notch filter. For training of the color-separating ANN, COS-7 cells singly-labeled by CF568 and AF647 for microtubules were STORM-imaged on the same setup, which naturally contained single molecules at all possible axial positions within the depth of field. For training of the axial-localization ANN, dye-labeled antibodies were attached to the coverslip for step-scanning in

the axial direction (Methods).

Figure 4a presents the acquired STORM image colored by the fitted Gaussian width (2σ) of the PSF of each molecule. Here a brightness threshold of 3000 photons was applied, and ∼40% of the identified single molecules met this criterion. This rejection of dimmer molecules may be compensated by collecting more (currently 20,000) frames of raw STORM data. Whereas it is clear that all the narrowest widths belonged to microtubules, which were stained by the shorter-wavelength dye CF568, larger widths were found at both microtubules and mitochondria (e.g., cyan arrows in Figure 17a). This result is similar to what we saw in the bead data (Figure 14d): defocusing broadens the PSF width, and so this simple parameter can no longer be used to separate colors. Remarkably, our color-separating ANN achieved excellent color separation for the entire image independent of axial position (and thus defocusing) (Figure 17b-d), and consistent results were obtained on different cells over repeated experiments (SI in ref[3]). Quantification of color classification accuracy, as separately determined using fixed cells singly labeled by CF568 (Figure 17j) and AF647 (Figure 17k), indicated that at ∼5000 photons, excellent accuracies of 98.2% were achieved for both dyes at the confidence threshold of 0.8. At ∼3000 photons, the accuracy for CF568 did not vary noticeably (Figure 17j), whereas the accuracy for AF647 dropped to ∼90.4% (Figure 17k). Lowering the confidence thresholds led to accuracy drops by a few percentage points (Figure 17jk). Previous work28 has shown that for dyes in these two color channels, through traditional sequential imaging using different optical filter sets, a ∼8% crosstalk occurred from the 561-nm excited dye into the 647-nm excited dye, whereas crosstalk in the opposite direction was ∼1%. Our accuracies thus appear to outperform at ∼5000 photons, a value often obtained in STORM experiments[24,25]. Moreover, in our case, all data were collected within the same optical path in a single STORM session, so we avoided the major difficulties in aligning images from different filter sets.

Based on our successful color classification, two axial-localization ANNs, each trained for AF647 and CF568, were next used to separately decode the axial positions of the molecules in the two color channels, the results of which were recombined into one image for presentation (Figure 17e and SI in ref[3]). This showed the expected result that the cell edges, thinner in height, were dominated by small z values, whereas for regions far away for the cell edges, the cells became thicker and had increased z values. White arrows in Figure 17ae further point to regions of microtubules, labeled by the same CF568 dye, where similarly increased PSF widths were noted, but the ANN correctly identified one being below the focal plane whereas the other above. Vertical cross-sectional views of the data correctly showed the hollow structure of the mitochondrial outer membrane (Figure 17fg), and distributions of the z-positions for the AF647-labeled mitochondrial outer membrane and the CF568-labeled microtubule both showed standard deviations of 30-40 nm (Figure 17hi). We further note that as the two color channels are successfully separated, they may also be separately fed into other recent methods that extract axial positions from unmodified PSFs[130,131].

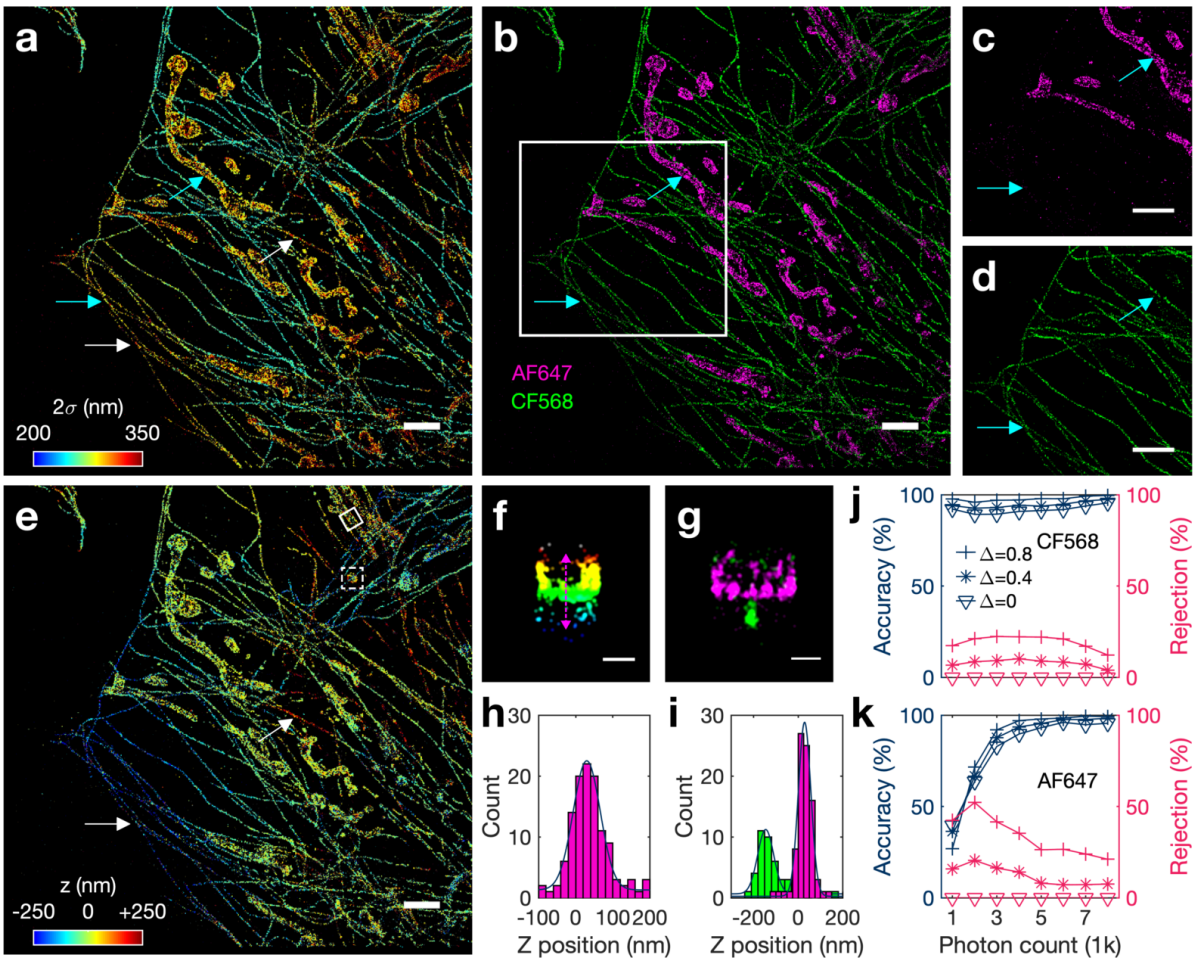

Figure 17: ANN-resolved multicolor 3D SMLM in cells based on unmodified PSFs. (a) STORM image of CF568-labeled microtubules and AF647-labeled mitochondrial outer membrane in a fixed COS-7 cell, colored by the fitted Gaussian width (2σ) of the PSF of each molecule, for molecules brighter than 3,000 photons. (b) Result of the color-separating ANN for the same dataset, at a confidence threshold of 0.8. (c-d) The separated AF647 (c) and CF568 (d) channels for the boxed area in (b). Cyan arrows in (a-d) point to two regions where molecules of similar PSF widths are correctly determined as different colors by the ANN. (e) The merged 3D STORM image after separately determining the axial position of every single molecule based on ANNs respectively trained for AF647 and CF568. Color here presents the axial position (z), with blue being closest to the substrate and red being the farthest away. White arrows in (a) and (e) point to two regions of the CF568 microtubule labeling that showed similar defocusing effects, but determined by ANN as being on opposite sides of the focal plane. (f-g) Vertical cross-sectional views for the (f) solid boxed area (colored by z) and (g) dashed boxed area (color separated by the ANN) in e. (h) Histogram of the axial (z) position along the magenta line in f (σ of the fitted Gaussian: 36 nm). (i) Histogram of the axial (z) position of the microtubule and the bottom membrane of the mitochondrion in g (σ of the fitted Gaussian: 36 and 28 nm, respectively). (j-k) Classification accuracy (left axis) and rejection rate (right axis) of the color-separating ANN as a function of photon count, for cells singly labeled by CF568 (j) and AF647 (k), at confidence thresholds of 0, 0.4, and 0.8. Scale bars, 2 μm (a-e), 200 nm (f-g).

4.2.5 Discussion

Our finding highlights the rich, multidimensional information concealed in the details of the diffraction-limited image of a fluorophore, which was unleashed in this work through machine learning algorithms. Not having to modify the PSF shape or divide single-molecule fluorescence between different optical paths, or to image sequentially, not only simplify experimental implementation, but more importantly, preclude the deterioration in SMLM performance due to enlarged PSFs and/or split channels, as well as the need to align localizations from different channels. Moreover, once trained, evaluation was straightforward and fast ($>3.3\text{x}10^5$ molecules/s with GPU acceleration) for both the color-separating and the axial-localization ANNs.

One limitation of our current work is good training samples for the z position. In the presence of index mismatch and supercritical angle fluorescence, PSFs acquired from coverslip-attached single molecules would be different from those labeled inside cells. While this is a common challenge for 3D-SMLM, recent work has shown the possibility to overcome such limits through imaging single molecules attached to known structures such as microspheres[140], as well as fluorescent beads encapsulated in an agarose gel[131]. Incorporating such approaches would help improve z precision.

Finally, we note that our end-to-end framework may be further extended to determine more parameters. As a first step, we evaluated the performance of lateral position (x/y) estimation using ANNs with simulated PSF images and achieved good precision when compared to the CRLB (Figure 18). The difficulty of applying such ANN analysis for lateral positions, as well as for other possible parameters, including the signal and background levels, however, resides with the difficulty in constructing good training sets with known"ground truth". Together, we expect the co-evolution of our data-driven end-to-end framework with ongoing efforts on PSF engineering[124] should lead to new improvements, and conceivably, new types of imaging modalities, for multidimensional SMLM.

4.3 Conclusion

In this chapter, we proposed a new multidimensional SMLM method through a data-driven approach. As unmodified PSFs already contain rich information such as emission color and axial position, we could extract the parameter of interest through the neural networks. Compared to the most up-to-date model based approach, maximum likelihood estimation of cubic spline PSF model, our approach exhibited comparable performance in color separation and axial localization. The capability and potential of this method are not limited to a specific parameter, thus we also demonstrated the lateral localization of simulated PSFs, and achieved good precision.

From experimentalists' point of view, such data-driven approach offers certain level of flexibility in designing the experiment. Not having to modify the optical or measurement setup or calibrating the system with numerous efforts, the parameter of interest is directly

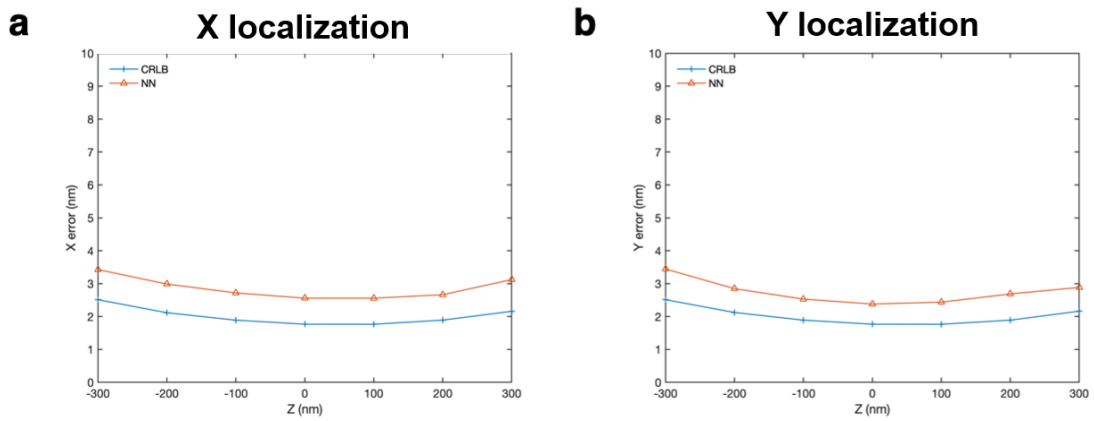

Figure 18: Localization precisions of the ANN-based estimation of (a) x and (b) y for simulated PSFs (5000 photons, 10 background photons/pixel, z=0), compared with the Cramer-Lao lower bound calculated from the cubic-spline model.

estimated. From theorists or data scientists' point of view, SMLM would be attractive in a sense that arbitrary amount of data can be acquired quickly, which is not the case most of the time. With ongoing efforts in PSF engineering as well as various machine learning approaches, we expect the data-driven approach in SMLM would lead superior performance and fascinating applications.

4.4 Materials and Method

Optical setup

STORM and bead experiments were performed on a Nikon Ti-E inverted fluorescence microscope using an oil-immersion objective lens (Nikon CFI Plan Apochromat λ 100x, NA 1.45) and the native 1.5x magnification on the microscope, without any modifications to the imaging path. Lasers emitting at 644, 561, and 488 nm were introduced to the back focal plane of the objective lens via a multi-line dichroic mirror (ZT405/488/561/640rpc-uf2, Chroma). A translation stage shifted the laser beams toward the edge of the objective lens so that they entered slightly below the critical angle, illuminating <1 μm into the sample. Emission was filtered by a multi-notch filter (ZET405/488/561/640m, Chroma) and recorded by an EM-CCD camera (iXon Ultra 897, Andor). Effective magnification and pixel size were $\sim$150x and $\sim$107 nm, respectively.

Beads samples

For bead experiments for color-classification (for both the training of the ANNs and the analysis of unknown samples), 40 nm dia. fluorescent beads from Invitrogen (F10720; "yellow" and "orange" FluoSpheres with emission peaks at 515 and 560 nm, respectively) were

diluted in Dulbecco's phosphate buffered saline (DPBS), mixed, and sealed between a glass slide and a pre-cleaned #1.5 thickness coverslip, and imaged with the above optical setup. The 488-nm and 561-nm lasers were used to excite the two types of beads to similar levels of brightness. To record images at different axial positions, the objective lens was scanned by the built-in motor over a range of -400 to +400 nm of the focal plane in 50 nm steps. To compare the performance of the axial-localization ANN with cubic-spline MLE, 40 nm dia. fluorescent beads from Invitrogen (F8789; "dark red" FluoSphere with an emission peak at 680 nm) were similarly prepared as described above, excited with the 644-nm laser, and scanned from -400 nm to +400 nm in 50 nm steps.

Cell samples

For STORM experiments (training of the color-separating ANN and the ANN analysis of unknown samples), COS-7 cells were plated on #1.5 coverslips to reach a confluency of ∼50% in ∼1.5 days, and fixed with 0.1% glutaraldehyde and 3% paraformaldehyde in DPBS at room temperature. The sample was quenched with 0.1% sodium borohydride in DPBS and rinsed with DBPS three times. Primary and secondary antibodies were diluted in a blocking buffer (3% BSA + 0.1% Triton X-100 in DPBS) and labeled as described previously[25]. Primary antibodies were mouse anti-tubulin (Abcam ab7291) for microtubules and rabbit anti-Tom20 (Santa Cruz sc-11415) for mitochondrial outer membrane. Secondary antibodies were AF647-labeled goat anti-mouse IgG1 (Invitrogen A21240), AF647-labeled goat anti-rabbit IgG (Invitrogen A21245), and donkey anti-mouse IgG (Jackson ImmunoResearch) conjugated with a CF568 succinimidyl ester (Biotium 92131). Samples for training the color-separating ANN were singly labeled for microtubules with CF568 or AF647, whereas for the two-color unknown samples, microtubules and the mitochondrial outer membrane were respectively labeled with CF568 and AF647. The sample was mounted in a STORM buffer [10% (w/v) glucose, 120 mM cysteamine, 0.8 mg/mL glucose oxidase, and 40 μg/mL catalase in Tris-HCl (pH 7.5)] and imaged using the optical setup described above. For consistent experimental conditions, all cell samples were imaged at comparable depths with the focal plane being ∼300 nm away from the coverslip surface. The sample was illuminated with the 561 and 644 nm lasers at ∼2 kW/cm^2, which led to the photoswitching of CF568 and AF647 single molecules. Fluorescence was recorded by the EM-CCD for a frame size of 256x256 pixels at 55 frames per second. Each movie was typically recorded for 20,000 frames.

Antibody samples

For training of the dye-specific axial-localization ANNs of AF647 and CF568 single molecules, the above AF647- and CF568-labeled secondary antibodies were separately diluted in DPBS to ∼2 μg/mL. Pre-cleaned #1.5 coverslips were separately incubated in either solution for ∼5 min, briefly air-dried, rinsed with distilled water, and mounted and imaged as described above for cells. To record single-molecule images at different axial positions, the objective

lens was scanned in the range of -700 to +700 nm of the focal plane in 50 nm steps. Note that two separate set of scanned images are attained, each for AF647 and CF568. This enables independent neural network training for the two types of dyes, eliminating chromatic errors by design.

Preprocessing of single-molecule images for ANNs

Single-molecule fluorescence in raw STORM and bead data was first identified and localized in 2D using established methods1. Here the goal was merely to obtain isolated single-molecule images as raw inputs of the ANNs, and similar results were obtained when using Insight3 (Dr. Bo Huang at University of California, San Francisco and Dr. Xiaowei Zhuang at Harvard University) or ThunderSTORM[141] (Dr. Martin Ovesny at Charles University in Prague and Dr. Guy M. Hagen at University of Colorado, Colorado Springs, available at https://github.com/zitmen/thunderstorm) (SI in ref[3]). Single-molecule PSF images were cropped as 13x13 pixels surrounding the 2D localizations. Here we rejected molecules that were too close to each other (<1 μm), and excluded abnormal single-molecule images with fitted widths (2σ) of $<\sim$400 nm. The cropped PSF images were zero-centered, and their L2/Euclidean norm was normalized before being used as inputs for ANNs.

Simulation of the PSF images

Realistic PSFs that account for the index discontinuity in the sample area were generated using the PSF generator package from EPFL31 (http://bigwww.epfl.ch/algorithms/psfgenerator) using the Gibson-Lanni (G-L) model19. Input parameters for the G-L model: NA=1.45, immersion layer index=1.51, sample layer index=1.33, working distance=130 μm, particle position=1 μm. The emission wavelength was set to be 600 nm and 700 nm for two-color classification, and 700 nm for z estimation. For all experiments, PSF stack was firstly generated with 20 nm axial step size over $\pm$600 nm range and at 5 nm lateral resolution. For the final image, this high-resolution PSF stack was down-sampled into 100 nm pixel grid, and the total sum of the values within 24x24 pixel region-of-interest is matched to the given photon count and offset by the background photons. Lastly, detector shot-noise was modeled as the Poisson process with the rate matched to the mean photon counts within each pixel.

Cubic-spline model-based maximum-likelihood estimation/classification

Openly available software from Zhuang group at Harvard University was used to generate cubic-spline models for the simulated and experimental PSFs, calculate Cramer-Rao lower bounds (CRLBs)[139], and MLE for z position (https://github.com/ZhuangLab/storm-analysis20). Since z estimation using MLE in relatively symmetric PSFs is prone to local minima problem18, we performed two MLE fit with different initial z value (+300nm/-300nm) and picked one that yields lower error. To perform MLE-based color classification, multiple error values, each from MLE fitting with one of the cubic spline models constructed

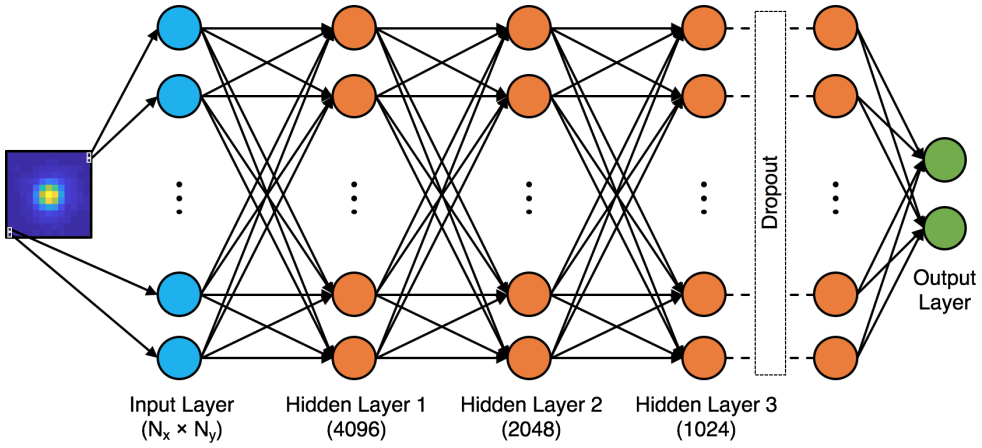

Figure 19: Architecture of the artificial neural network used in the paper.

with PSF stacks of the two different emission wavelengths, were returned and then compared to pick the color that finally minimizes the likelihood error (again MLE fitting for each color actually includes two fitting with different initial z, resulting in four MLE runs in total). As for obtaining the PSF image stack for the spline models, while the ground truth of the 3D positions of the simulated PSFs are known by definition, for experiments on fluorescent beads (∼15,000 photons), the in-plane positions were estimated through Gaussian least-squares fitting, and axial positions were from z scanning.

Design and implementation of neural networks

An ANN architecture comprising multiple hidden layers was implemented using the Tensorflow framework on a computer with 32GB RAM, Intel i7-7800X CPU, and Nvidia GTX-1080Ti GPU. The same architecture was used for both the color-separating and axial-localization ANNs (4 total layers of 4096-4096-2048-1024 neurons, respectively; Figure 19). Each hidden layer was fully connected, and rectified linear units were used as their activation function. For color discrimination, Softmax function and cross-entropy were used for loss calculation, the weights in the network were not directly included for regularization, and a dropout layer was inserted before the final layer to prevent over-fitting. For axial/lateral localization, the output of the final layer was set to be a scalar value, and L2 norm was used to calculate the learning loss for each batch. In this case, L2 norm of the weights in each layer was added to the loss function for regularization, and dropout was not used. Network hyper-parameters such as the number of neurons in each layer (given above), the dropout ratio (0.5 for the color-separating ANN), and the regularization factor (0.01 for the axial-localization ANNs) were adjusted for optimized performance. The codes for our ANN implementation are available online (https://github.com/ann-storm/ann-storm).

Nerual network training

Since the network is subject to handling input images with various noise levels, it was essential to maintain a consistent noise level within the training dataset regardless of the classification class or axial location. Therefore, experimental PSF images with comparable photon counts of 4500-5500 were used throughout the training process, and molecules with photon counts higher than this range were used for the validation during the training process to check the generalization of the trained network. The weights initialized by the Xavier method32 are trained using the Adam optimization algorithm. An initial learning rate of 10^{-4} and 10^{-3}, and a batch size of 64 and 32 were used for the color-separating and the axial-localization ANNs, respectively. The learning rate was set to decrease by ∼5x after every 1,000 iterations. The sizes of the training sets were ∼10,000 and ∼6,000 per fluorophore type for the color-separating and the axial-localization ANNs, respectively. The networks converged within ∼10 epochs (training time: 231.9 s for the color-separating ANN, and 488.5 s for the axial-localization ANNs).

Nerual network inference

At the inference stage, input single-molecule PSF images were first plugged into the color-separating ANN. This ANN provides a conditional probability distribution corresponding to the input image. Specifically, when the size of each input image is N by N pixels, and there are M different molecule color classes, the final output from the Softmax layer for the ith input image is

$$P(y_i|x_i),\ x_i \in R^{N\times N},\ y_i \in \{Dye\ 1, \cdots, Dye\ M\} \tag{4.1}$$

From this distribution, the ANN makes the decision in a maximum a posteriori (MAP) manner : through training, ANN provides the posterior distribution, and the molecule color class with the highest probability is chosen. This, in turn, implies that we can use this distribution to quantify the classification confidence. For example, in a simple binary classification problem, the confidence for the color assignment of the ith input image can be evaluated as:

$$|\Delta_i| = |P(Dye\ 1|\ x_i)\ -\ P(Dye\ 2|\ x_i)| \tag{4.2}$$

By setting a finite confidence threshold δ to reject molecules with low classification confidences ($|\Delta i| < \delta$), improved classification accuracy may be obtained (Figs. 2gh and 4jk). This parameter may thus be adjusted by the user to balance the classification accuracy and rejection rate. Once the color of the molecule is determined, the single-molecule image is plugged into the axial-localization ANN trained for that particular color to evaluate the axial position. With GPU acceleration, both inference steps (passing the forward path of the neural networks) were extremely fast: only ∼300 ms was used to infer 100,000 molecules for both the color-separating and the axial-localization ANNs.

Chapter 5

Spectrally resolved and functional super-resolution microscopy via ultrahigh-throughput single-molecule spectroscopy

The work in this chapter was conducted in collaboration with Rui Yan, Samuel J. Kenny, and Ke Xu. It is in part reproduced here from ref[4] with permission from all coauthors.

5.1 Introduction

In the previous chapters, we looked into the working principles of spectrally-resolved super-resolution microscopy (SR-SRM) and its application in the biological system and the surface chemistry. To conclude this part, we summarize the rationale, design, and results of recent efforts towards the integration of the spectral dimension of single-molecule fluorescence with SMLM to achieve SR-SMLM and functional SRM (f-SRM) in this chapter.

The diffraction-imposed, ∼300 nm resolution limit of light microscopy has been surmounted in the past decade by super-resolution (fluorescence) microscopy/nanoscopy (SRM)[106,142]. While offering remarkable spatial resolution of ∼10 nm and profound impacts across multiple research fields[83,106,143], SRM typically provides monochrome images. The lack of spectral information complicates efforts of multicolor/multi-target SRM; common approaches rely on the false-color superimposition of images obtained from different filter channels, for which image alignment and signal crosstalk are often challenging. Moreover, colorless images only convey spatial information and leave little room beyond structure and shape.

By tapping into the often overlooked, yet extremely informative dimension of fluorescence spectrum, we have recently realized spectrally resolved SRM for highly multiplexed imaging. By encoding functional information into this new spectral dimension with environment-

sensing probes, functional SRM further enables the interrogation of local physicochemical parameters at the nanoscale. These remarkable results are achieved by integrating the spatial, temporal, and spectral dimensions of single-molecule fluorescence.

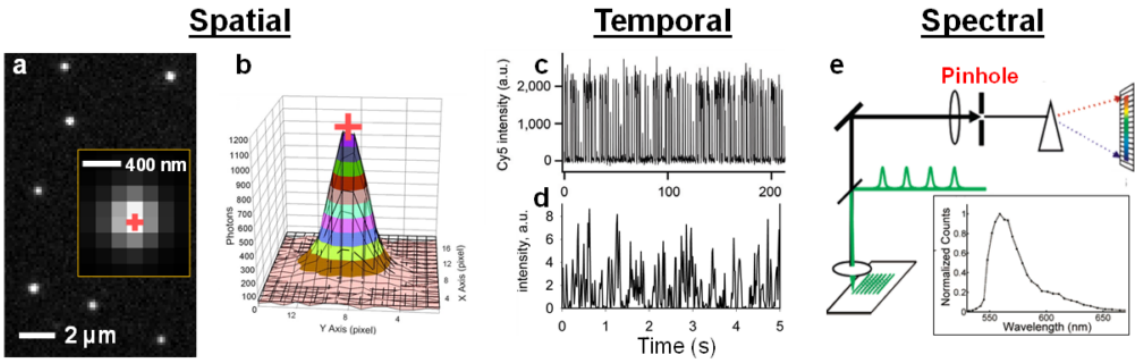

Figure 20: The spatial, temporal, and spectral dimensions of single-molecule fluorescence. (a): Wide-field fluorescence image of single AF647 molecules. (b): Intensity distribution of a Cy3 molecule as recorded by a camera. Red crosses in (a,b) mark peak positions. Adapted with permission from ref[11]. (c): Laser-induced reversible fluorescence photoswitching of a Cy3-Cy5 dye pair. Adapted with permission from ref[7]. (d): Fluorescence bursts due to the binding/unbinding of single Nile Red molecules to a lipid vesicle. Adapted with permission from ref[9]. Copyright 2006 National Academy of Sciences. (e) Scanning-based single-location spectroscopy for single molecules. Adapted with permission from ref[34].

Fluorescence detection provides a non-invasive and target-specific means to probe single molecules[32,33,144,145]. Figure 20a shows a typical wide-field fluorescence image of single Alexa Fluor 647 (AF647) molecules. Due to diffraction, single molecules appear as ∼300 nm-sized spots. However, it is recognized that the position of a single molecule can be determined with nanometer-precision by fitting the intensity distribution of its image (Figure 20b) to known functions[10,11]. The ability to thus "super-localize" the position of a molecule is crucial for experiments that utilize the spatial information of single molecules.

Time trajectories of intensity represent another important aspect of single-molecule fluorescence. In particular, the integration of on-off intensity dynamics (fluorescence switching; Figure 20c,d) with the aforementioned ability to super-localize single molecules has led to the invention[7,8,146] of a major class of SRM methods generally known as single-molecule localization microscopy (SMLM). In one such implementation, STORM (stochastic optical reconstruction microscopy)[7], fluorescent molecules are first photoswitched to a non-emitting state. Small, random subsets of the non-emitting molecules are then photoswitched (Figure 20c) back to the emitting state and super-localized over different camera frames to construct an SRM image. In another SMLM approach called PAINT (points accumulation for imaging in nanoscale topography)[9], the reversible binding/unbinding of fluorescent molecules to the sample (Figure 20d) is utilized to achieve single-molecule localization. Chemical reactions can also achieve on-off switching via the in situ generation of fluorescent molecules; super-localizing the product molecules enables super-resolution mapping of local reactivity[143,145,147].

Spectrum measurement is another key component of single-molecule fluorescence, but one that is also highly challenging. Whereas the recording of total light intensity suffices for examining the spatial and temporal dimensions of single-molecule fluorescence, to scrutinize the spectral dimension would necessitate the wavelength-dependent detection of light. The use of a dichroic mirror to split fluorescence into long- and short-wavelength components offers a facile way to estimate the emission wavelength of single molecules by calculating the intensity ratio of the two components[26,27], and this "ratiometric" approach has been successfully incorporated with SMLM[29–31]. However, actual spectra are not obtained, and the result is subject to sample background and performance of the dichroic mirror (Table 1 below).

To truly resolve single-molecule spectra, previous work has often employed spatially confined illumination and detection for spectral dispersion of the fluorescence from a single spot of the sample[28,32–34,87,148,149]. Sample scanning then enables the mapping of the positions and spectra of sparsely distributed molecules at different locations with limited throughput (Figure 20e). Although multiplexed arrays of confined illumination and detection spots have enabled the parallel measurement of single-molecule spectra with high throughput[150], such approaches are difficult to apply to imaging and still rely on the sparse distribution of molecules.

5.2 Spectrally resolved super-resolution microscopy via ultrahigh-throughput single-molecule spectroscopy

To overcome these limits in the context of SMLM, we reasoned[35] that sparsely distributed single fluorescent molecules are discrete, self-confined point sources (Figure 21a). Consequently, to collect their spectra, it appears unnecessary to impose further spatial confinement in illumination or detection as done in previous studies. Instead, using a prism, the emission of many molecules in the same field of view may be simultaneously dispersed into spectra and recorded with a camera (Figure 21b). Although analogous wide-field spectroscopy approaches are occasionally used in astronomy for stellar spectra[151], their direct application to single-molecule experiments has been limited to sparse systems[85,152]. We found that by integrating SMLM[7–9,146] with our wide-field spectroscopy scheme, a few-millisecond snapshot could readily capture the emission spectra of $\sim 10^2$ randomly distributed single molecules. Via photoswitching (for STORM) or reversible labeling (for PAINT), we then stochastically lit up different populations of molecules over consecutive camera frames, and obtained the spectra of $\sim 10^6$ single molecules in a densely labeled sample within minutes. In contrast with previous scanning-based single-location imaging/spectroscopy approaches in which a few molecules are probed per minute, we deem this wide-field approach "ultrahigh-throughput".

A hidden pitfall of the above wide-field scheme is that the spatial and spectral information of a randomly located molecule is coupled[35]: the dispersed spectrum of a redder molecule may appear identical to that of a bluer molecule physically located further to the right. An

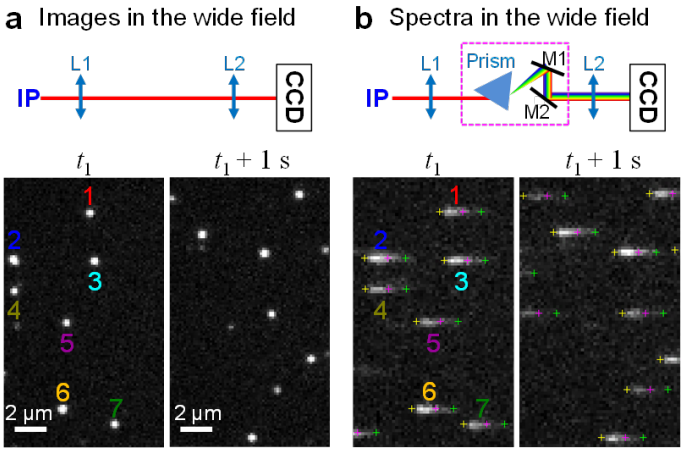

Figure 21: Wide-field fluorescence spectroscopy for single molecules. (a) Top: Wide-field image is relayed through lenses L1 and L2. IP: intermediate image plane of microscope. Bottom: A small part of the acquired images of single immunolabeled AF647 molecules in a fixed cell in two 9-ms camera frames separated by 1 s. (b) Top: A prism is placed at the Fourier plane between L1 and L2. Bottom: The dispersed spectra for the same molecules in (a), recorded in the wide-field concurrently with the images in (a). Yellow, magenta, and green crosses: spectral positions of 647, 700 and 750 nm for each molecule, mapped based on calibration obtained using narrow bandpass filters and lasers of known wavelengths. Adapted with permission from ref[35].

independent reference image is thus necessary to decouple the spatial and spectral dimensions and produce the final result of spectrally resolved SMLM (SR-SMLM; including SR-STORM and SR-PAINT).

In our initial work[35], we employed a dual-objective scheme in which the sample is sandwiched between two opposing objective lenses, so that separate objectives are dedicated to the positional (Figure 22a, Path 1) and spectral (Figure 22a, Path 2) measurements of the same single molecules. This design achieves excellent light efficiency: the image channel of Path 1 is unmodified when compared to regular SMLM setups, whereas the spectral information from Path 2 is added on "for free". The major drawback is that samples need to be thin and transparent to allow imaging from the backside, and the mounting geometry is unfavorable for live-cell experiments.

Mlodzianoski *et al.*[81] reported an SR-SMLM system based on an inverted microscope with a single objective lens. A beam splitter divided the fluorescence collected by the objective lens into two paths for separate positional and spectral detections of single molecules. We employed a similar strategy (Figure 22b) in our recent work on live cells[1]. Although dividing the signal into two paths reduces the available photons for each path, this system imposes fewer sample constraints and is simpler in design.

Recent work has also reported SR-SMLM through concurrent positional and spectral recording via the zeroth and first diffraction orders of a grating[36,82], a strategy used in earlier single-molecule/single-particle studies[85,152]. Although gratings could in principle provide higher resolving power over prisms and offer the benefit of linear dispersion, they achieve

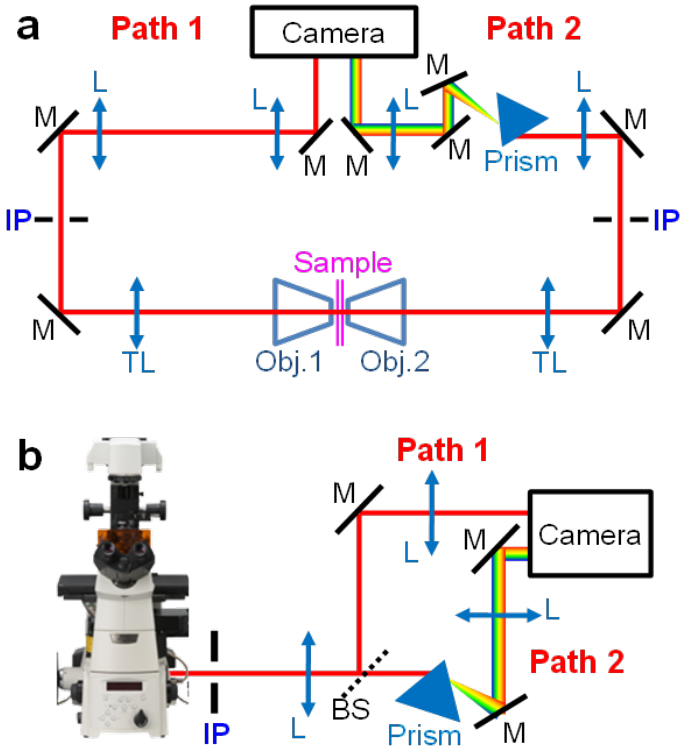

Figure 22: Concurrent positional and spectral measurement of single molecules. (a) System based on two opposing objective lenses. (b) System based on an inverted microscope with a single objective lens. Obj., objective lens; TL, tube lens; M, mirror; L, lens; BS, beam splitter; IP, intermediate image plane. For both schemes, Paths 1 and 2 provide unmodified images and dispersed spectra of single molecules, respectively.

limited light efficiency, which could be a concern given the restricted photon budget for single molecules. Their strong dispersion also reduces the signal-to-noise ratio of each pixel and exacerbates overlapping between the dispersed spectra of different molecules, making it difficult to probe densely labeled two-dimensional structures.

Another strategy encodes the spectral information of single molecules into the shape of single-molecule images (point spread functions; PSFs)[127,154,155]. Although such approaches remove the need for a reference image, they do not provide actual spectra. The spatial light modulator or phase mask involved also limits light-use efficiency. Color separation is thus only demonstrated for large wavelength differences. See Table 1 for a summary of different approaches and their major limitations.

5.3 Spectrally resolved super-resolution microscopy for multiplexed imaging

One immediate application of SR-SMLM is multiplexed SRM. To determine how well different fluorophores can be distinguished, we first characterized the intrinsic spectral variation

Method	Demonstrated multicolor SMLM	Major limitation	Ref
ratiometric detection	4 fluorophores at ∼20 nm separation	spectra not obtained; results subject to dichroic mirror	[29–31]
dual-objective + prism	4 fluorophores at ∼10 nm separation	thin, transparent samples only	[35, 153]
beam splitter + prism	3 fluorophores at ∼20 nm separation	photons split over two channels	[1, 81]
diffraction grating	2 fluorophores at ∼20 nm separation	low light efficiency; signal spread over too many pixels	[36, 82]
PSF engineering	2 fluorophores at >100 nm separation	spectra not obtained; low light efficiency	[127]

Table 1: Spectroscopic approaches for SMLM

between individual molecules of the same fluorophore[35]. Previous studies reported substantial spectral variation (standard deviation ∼10 nm) for single dye molecules immobilized at solid surfaces (e.g., Figure 23a)[32,87,148,149]. Meanwhile, ratiometric SMLM of dye-labeled biological samples[29,30] found relatively high uncertainty in fluorophore identification (∼20% crosstalk for 4 dyes at ∼20 nm spectral separation), and it was unclear how much of the uncertainty is due to intrinsic spectral variation between single molecules.

Remarkably, with SR-STORM, we found that in typical buffers, single immunolabeled dye molecules exhibit highly uniform fluorescence emission in cells (Figure 23bc)[35]. Statistics of the spectral mean, calculated as the intensity-weighted average of wavelengths of each molecule[87], gave a standard deviation of 2.6 nm for the ∼6x10^5 individual AF647 molecules detected in the sample shown in Figure 21, with the brighter molecules (>10,000 detected photons) converging to an extremely small standard deviation of 1.4 nm (Figure 23c). Notably, a previous study measured the emission spectra of 220 single AF647 molecules electrokinetically trapped in an aqueous buffer, and it also noted a narrow distribution of emission wavelength (standard deviation ∼3.5 nm)[154]. Together, these results suggest that in aqueous buffers, single dye molecules may be characterized by much narrower emission distributions when compared to surface-trapped molecules. To generalize this finding, we investigated fourteen 647-nm-excited far-red dyes and found homogeneous single-molecule spectra for all (standard deviations of 2.5-4.5 nm in single-molecule spectral mean; Figure 23d). Meanwhile, substantial spectral differences were detected for different dyes (Figure 23d).

Our method, consequently, should reliably distinguish single molecules of different dyes that differ minimally in emission spectrum. To show this, we performed SR-STORM on cells in which four distinct subcellular structures were immunolabeled by four 647-nm-excited far-

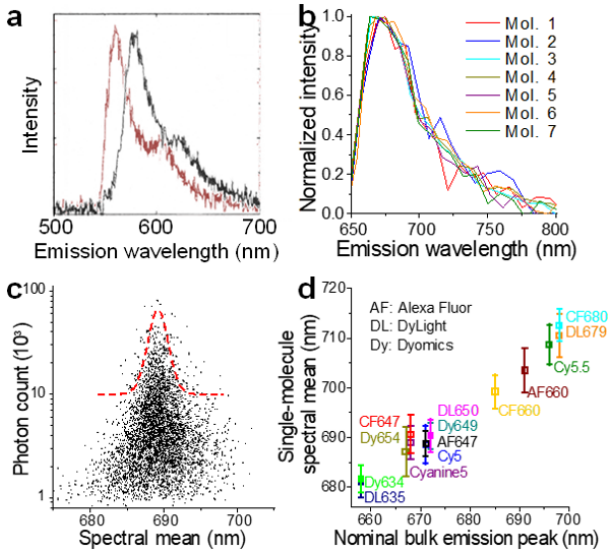

Figure 23: Variation in single-molecule fluorescence spectra. (a) Spectra of two DiIC12(3) molecules at a PMMA-air surface. Adapted with permission from ref[149]. (b) Spectra of the individual AF647 molecules labeled as 1-7 in Figure 21. (c) Measured spectral mean vs. photon count for 6,406 single AF647 molecules detected within 3 s. (d): Single-molecule spectral mean distribution of 14 different dyes, each obtained through SR-STORM from 10^6 molecules. Error bars represent standard deviation between single molecules. (b-d) Adapted with permission from ref[35].

red dyes just 10 nm apart in emission wavelength[35]. By color-coding each detected single molecule according to its measured spectral mean on a continuous scale, we found that in the resultant "true-color" SR-STORM images, molecules of different dyes were readily distinguishable, so that distinct colors showed up for the four differently labeled subcellular structures (Figure 24a). Classification of the spectrum of each single molecule into the four dyes gave excellent separation (Figure 24b) and negligible ($<\sim$1%) misidentification (Figure 24c). Meanwhile, locally averaged single-molecule spectra for the different sub-diffraction-limit structures showed good agreement with corresponding dyes (Figure 24d). It is also apparent from Figure 24d that as the emission spectra are so heavily overlapping between the four dyes, color separation would not have been possible with conventional approaches using bandpass filters.

We further integrated our approach with 3D-STORM[25] by encoding depth information into the shape of single-molecule images (Figure 25). The resultant four-dimensional (1D spectral + 3D spatial) information of every molecule allowed us to achieve crosstalk-free four-color 3D SRM in which the 3D images of all labels were collected in the same coordinates. We thus circumvented the major challenge of aligning different SRM channels in 3D, as faced by many traditional approaches. Meanwhile, as the spectral information was provided by a second objective lens, the photon counts and spatial resolution of the image channel remained typical of regular SMLM setups[35].

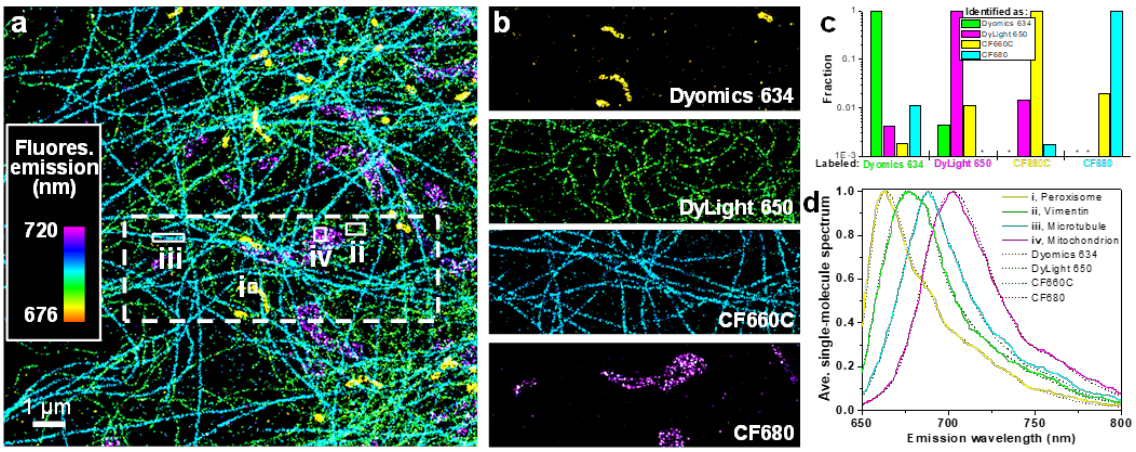

Figure 24: SR-STORM for four-color SRM. (a) "True-color" SR-STORM image of 4 subcellular targets immunolabeled by four far-red dyes at 10 nm spectral separation. Color presents the measured spectral mean of each molecule on a continuous scale (inset). (b) Separation of the four dye channels for the dash-boxed area in (a). (c): Identification/misidentification of the four dyes based on the measured single-molecule spectra (asterisks: $<10^{-3}$) (d) Averaged single-molecule spectra for the different nanoscale subcellular structures (i-iv) marked in (a), compared to that individually measured for the four dye molecules. Adapted with permission from ref[35].

5.4 Functional super-resolution microscopy

With the success of SR-SMLM for multiplexed SRM, our next challenge was[35] to further integrate fluorophores that are spectrally responsive to local environments, so as to utilize the new, spectral dimension of single-molecule fluorescence to probe local functional parameters, hence functional SRM (f-SRM). By "functional", we emphasize the possibility to advance beyond the"structural" information available to typical SRM techniques, and reveal the spatiotemporal distribution of physicochemical parameters, e.g., chemical polarity, pH, ion concentrations, and viscosity, with nanoscale spatial resolution and single-molecule sensitivity.

Although many fluorescent probes have been developed to report local environments through spectral changes[41,44,75], conventional detection methods provide limited spatial resolution, which, in turn, leads to reduced sensitivity to local spectral differences. Being able to scrutinize the spectral response of every probe molecule one at a time may help achieve the ultimate sensitivity for local environment. Earlier, pioneering single-molecule spectral studies of environment-sensing probes were limited to low molecule counts in sparse samples[26,113]. With the ultrahigh throughput of SR-SMLM, it now appears possible to map out functional parameters at the nanoscale with millions of individual probe molecules. The observation that single molecules ~10 nm apart in emission wavelength are readily distinguished from each other (Figure 24) further suggests high sensitivity.

Bongiovanni *et al.*[82] combined Nile Red, a solvatochromic dye, with SR-PAINT to enable hydrophobicity mapping of unilamellar lipid vesicles, in vitro protein aggregates, and cell

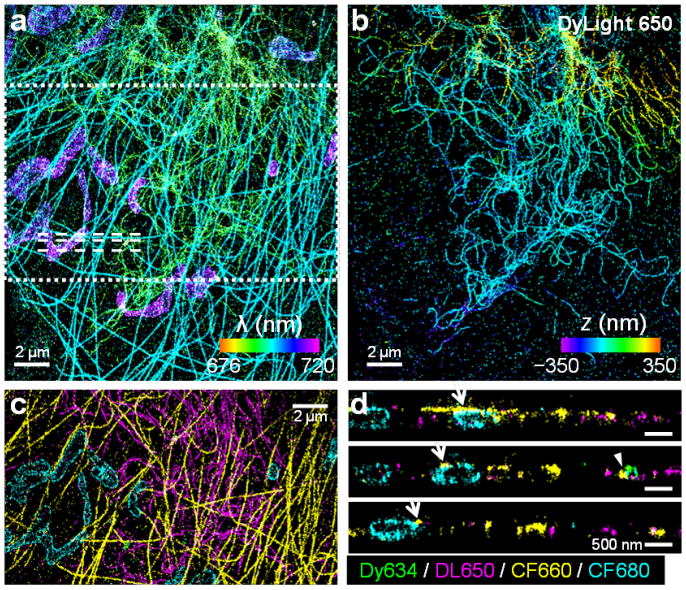

Figure 25: SR-STORM for 3D-SRM. (a) True-color SR-STORM image of a cell similar to that in Figure 24. (b) The isolated channel of one of the four dyes, recolored according to depth (z) (color bar). (c) Virtual in-plane (xy) cross-section for the boxed area in (a), at the center of the mitochondria. Here each molecule is categorized as one of the four dyes and accordingly false-colored. (d) Vertical xz-sections along the three dashed lines in (a). Adapted with permission from ref[35].

surfaces. However, as experiments were based on the zeroth and first diffraction orders of a grating (discussion above), the strong dispersion did not allow for the probing of dense two-dimensional structures like in-plane views of the cell.

5.4.1 Application of functional-SRM to biological system

As discussed in chapter 2, we achieved Nile Red-based SR-STORM and SR-PAINT f-SRM for the membranes of live mammalian cells, and thus revealed their compositional heterogeneity at the nanoscale[1]. This was implemented with a single objective, prism-based beam-splitting design to accommodate for the sample type (live cells) and desirable (weaker in this case) dispersion. By collecting the spectral and spatial information of $\sim 10^6$ membrane-bound, 561-nm excited Nile Red molecules, we again assigned a color to each molecule based on its spectral mean.

Remarkably, the resultant true-color SRM images revealed striking spectral differences between the plasma membrane and the membranes of intracellular organelles, and such differences were maintained as the cellular membranes rearranged at the nanoscale. The averaged single-molecule spectra were identical for mitochondrial and endoplasmic reticulum (ER) membranes, but redshifted by $\sim$20 nm when compared to the plasma membrane. Based on the solvatochromic behavior of Nile Red, the redder spectra of intracellular membranes suggest that they are more polar and thus more flexible and permeable, in agreement with

their expected functions[61]. These results are also in line with recent, diffraction-limited ratiometric and lifetime imaging studies employing UV- and violet-excited probes of stronger solvatochromic effects[44,66,67].

We next determined that the striking polarity differences we found for the organelle and plasma membranes were driven by their known disparity[61] in cholesterol level. A comparison with SR-PAINT f-SRM results of supported lipid bilayers indicated that the organelle and plasma membranes were spectrally analogous to cholesterol-free and cholesterol-added bilayers, respectively. In cells, we found that depleting cholesterol significantly redshifted single-molecule spectra at the plasma membrane, so that the spectral difference between the plasma membrane and organelle membranes was largely removed, as evidenced by both true-color SRM images and locally averaged single-molecule spectra. Conversely, the addition of cholesterol led to significant blueshifts of all cellular membranes. Together, these results indicate that cholesterol, known to play key roles in packing lipid bilayers into more ordered and less hydrated phases[61,73], drives the polarity differences we found between the plasma and organelle membranes.

Intriguingly, for cholesterol-added cells, in addition to an overall blueshift, f-SRM further revealed nanosized (∼100 nm) domains of strongly blue-shifted spectra across the plasma membrane. This result suggests the presence of a new, highly nonpolar phase at the nanoscale, reminiscent of the long-hypothesized cholesterol-rich, raft-like nanodomains in cell membranes[69,73]. Following this lead, we found that similar low-polarity nanodomains can also be induced by cholera toxin B-subunit (CTB), a common lipid-raft marker and stabilizer. Through comparisons of both f-SRM images and the distributions of single-molecule spectra from f-SRM data, we further concluded that such low-polarity membrane phases are likely absent in untreated native cells. We thus revealed rich nanoscale heterogeneity in live-cell membranes, both between organelle and plasma membranes and within the plasma membrane itself. Please refer to chapter 2 for more details.

5.4.2 Application of functional-SRM to non-biological systems

Whereas SRM has been first realized and popular in life science field, its application now extends to non-biological systems such as surface chemistry[2], and 2D materials[156]. Chapter 3 describes one application in surface chemistry, where morphology and chemical polarity of organic adsorbed layers (adlayers) on surface were characterized by f-SRM. Being extremely thin and fragile, characterization of the adlayers has been challenging, especially in optical means. Despite of the importance of the adlayers in wide-ranging applications from semiconductor industry[95] to crude-oil production[99], the characterization relies on rather low-throughput and perturbing methods, like atomic force microscopy (AFM).

We employed Nile red-based f-SRM to probe nanoscale structures and composition of the adlayers on surface. By using Nile red as a fluorescent probe and a local polarity reporter, our f-SRM provides good resolution (∼30 nm) as well as their composition. Although this information is accessible with AFM measurement to some extent, the interaction between an AFM tip and the adlayer may change and perturb the original morphology[2]. We charac-

terized morphology of common organic solvents of varying chemical polarity, and observed that the overall structures of the adlayers have dependence on the solvent polarity. Whereas non-polar solvent such as trichloroethylene (TCE) forms droplet-like structures, moderately polar solvents such as chloroform form line-like structures.

We also resolved the composition of the adlayers through spectrum of individual Nile red molecules detected. This suggests that we could reveal the composition of mixture through the spectral analysis. Remarkably, we observed spontaneous demixing behavior of two solvents, TCE and choloroform, on a glass surface. Although the two solvents mix well in bulk, they demix on the surface and form heterogeneous structures. We noted large (dia. $\sim$200 nm) nanodropets of bluer spectra, and smaller ($<$100 nm), redder droplets in fragmented line-like structures. From their spectra, we identified that the larger droplets are mainly comprised of TCE while the smaller droplets are mixture of the two solvent in varying ratio. Please refer to chapter 3 for more details.

Recently, interesting application of SR-SMLM to 2D material was reported. Comtet *et al.* utilized SR-SMLM to characterize optically active point defects in hexagonal boron nitride (hBN)[156]. With $\sim$6 eV band gap ($\sim$206 nm), a perfect hBN would not be responsive to excitation laser at 561 nm (2.21 eV). The point defects on hBN might change the electronic structure locally, thus making some of such defects optically active under the same circumstance. SMLM enables spatial mapping on such defects at nanometer scale, while the spectrum of emitters tells us about the nature of such defects. Note that this method relies on autofluorescence from the defects, without employing a fluorescent reporter. Compared to transmission electron microscopy (TEM), also used to characterize the point defects, this approach is high throughput and non-destructive. To summarize, these works demonstrate the potential of SR-SMLM as a powerful analytical tool in chemistry and material science, providing good spatial resolution and high throughput while being non-invasive.

5.5 Spectrally resolved super-resolution microscopy reveals reaction pathways of single molecules

The integration of SMLM with the spectral measurement of single molecules has also proven valuable for investigating single-molecule reactions[153]. Recent studies have established fluorescence microscopy as an important tool to study single-molecule chemical reactions[143,145,147]. In particular, for fluorogenic reactions, monitoring when (temporal dimension) and where (spatial dimension) individual fluorescent product molecules are generated has provided rich information on reaction dynamics and enabled reactivity mapping at the super-resolution level. Further incorporating the fluorescence spectrum could provide a powerful means to identify and characterize product molecules. However, as the reactant molecules are often non-fluorescent and so undetectable before the reaction occurs, it is naturally difficult to follow single-molecule reactions with traditional single-position spectroscopy approaches. In contrast, the wide-field nature of SR-SMLM offers a direct means to capture the fluo-

rescence spectra of single molecules that sporadically switch into the fluorescent state at random locations (Figures 2 and 10), and can thus deliver the missing spectral dimension of single-molecule reactions.

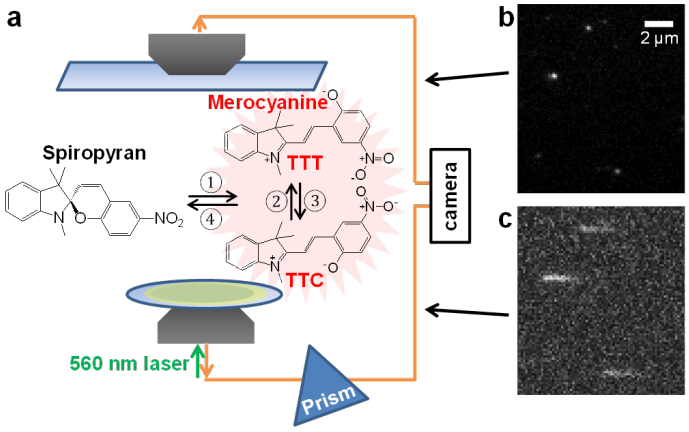

Figure 26: SR-SMLM investigation of the ring-opening (1), ring-closure (4), and cis-trans isomerization (2,3) reactions of single spiropyran molecules. (a) Schematic of the system. (b,c) A small region of the concurrently acquired fluorescence images (b) and spectra (c) of three single product molecules, obtained in a 33-ms snapshot. Adapted with permission from ref[153].

To demonstrate this possibility, we studied the fluorogenic ring-opening reaction of the photochromic spiropyran 1',3'-Dihydro-1',3',3'-trimethyl-6-nitrospiro[2H-1-benzopyran-2,2'-(2H)-indole] (6-nitro BIPS)[153].This reaction generates two major fluorescent cis-trans merocyanine isomers, TTC and TTT (Figure 26a)[157], but with bulk measurements it is difficult to separate their respective spectral contributions to the product mixture.

With SR-SMLM, we obtained the spectra and locations of thousands of individual fluorescent product molecules stochastically generated from the ring-opening of surface-adsorbed 6-nitro BIPS (Figure 26). Remarkably, we identified two populations that were comparable in brightness but distinct in spectral mean (Figure 27a-c) and spectrum (Figure 27d), attributable to the TTC and TTT isomers. Moreover, we found a strong solvent polarity dependence for the relative population of the two products (Figure 27a-c,e), signifying the importance of solvent in determining the reaction pathway.

By examining the spectral time traces of individual molecules, we next identified various single-molecule reaction processes, including stable isomers (Figure 28a), isomerization between the two isomers (Figure 28bc), ring-closure reaction back to the spiropyran form (Figure 28de), as well as more complex behaviors involving multiple processes (Figure 12f). For these results, the capability to super-localize single molecules with high precision was instrumental in ascribing multiple fluorescence signals to the same molecule. We thus demonstrated that the spectrum-resolving capability of SR-SMLM could unveil rich, multi-path pathways for single-molecule reactions.

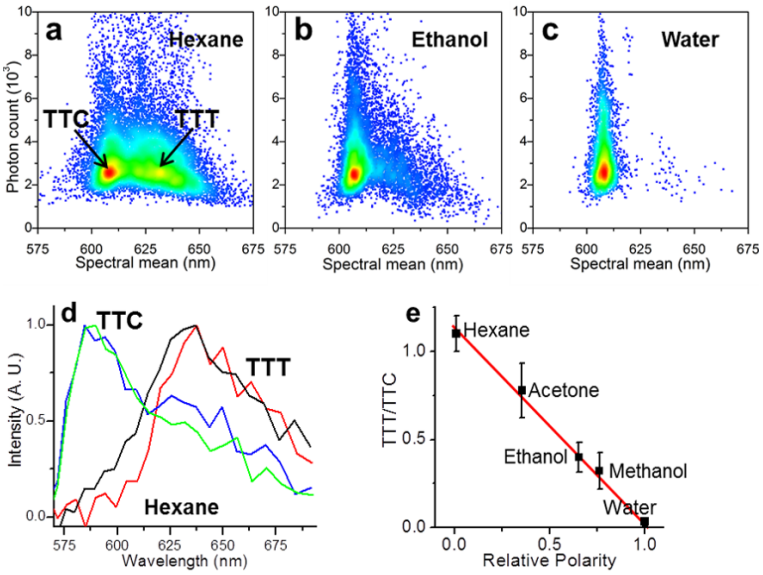

Figure 27: Statistics of single-molecule spectra reveals two spectrally distinct products for the ring-opening of 6-nitro BIPS. (a-c) Distribution of the measured single-molecule spectral mean and photon count in n-hexane, ethanol, and water. (d) Representative single-molecule spectra of the two isomers in n-hexane. (e) Dependence of the TTT/TTC ratio as a function of solvent polarity. Adapted with permission from Ref 35.

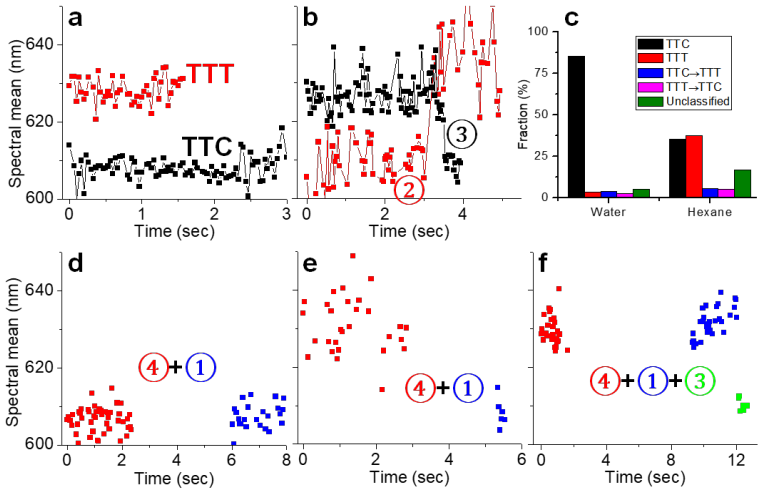

Figure 28: Monitoring the reaction pathways of single molecules through spectral time traces. (a) Time traces for two spectrally unvarying TTC (black) and TTT (red) product molecules. (b) Time traces showing TTC → TTT (red) and TTT → TTC (black) isomerizations. (c) Statistics of ∼1,000 single-molecule spectral time traces in water and hexane as stable isomers or isomerization processes. (d-f) Time traces involving reversible on/off single-molecule fluorescence switching attributable to ring-closure. Circled numbers in (b, d-f) correspond to the different reaction pathways in Figure 26a. Adapted with permission from Ref[153].

5.6 Conclusion and Outlook

By integrating the spatial, temporal, and spectral dimensions of single-molecule fluorescence through a wide-field scheme, our SR-SMLM approach has merged and expanded the capa-

bilities of SRM and single-molecule spectroscopy.

For multiplexed SRM, as we have achieved near-zero color-crosstalk between 4 far-red dyes ∼10 nm apart in emission wavelength, it is conceivable that more fluorophores may be included in the same far-red emission window (to be excited by a single red laser) at the expense of modest crosstalk between channels. The combination of different excitation lasers (we have so far demonstrated 560 and 647 nm) could enable even more color channels over wider spectral windows, although attempts to record too many dyes simultaneously could make it difficult to achieve the desired single-molecule sparsity.

For f-SRM, we have shown how measuring the fluorescence spectra of millions of polarity-sensing single molecules can reveal nanoscale compositional heterogeneity in live-cell membranes. The ultimate sensitivity achieved through scrutinizing the spectral response of individual molecules may also be harnessed to probe other parameters, e.g., local pH, viscosity, and protein activity, in cells and other biological systems. Major challenges in exploring these possibilities lie in the identification or construction of suitable fluorescent probes that are both environmentally sensitive and SMLM-compatible. Meanwhile, the specific tagging of sensing fluorophores to target (bio)molecules would be highly valuable in constraining environment probing to specific (subcellular) structures.

We also have shown that application of f-SRM is not necessarily limted to biological system, but could extend to non-biological systems such as surface chemistry and material science. f-SRM has successfully characterized the morphology and composition of the adlayers on surface. Furthermore, the recent work demonstrated the optical inspection of the point defects on hBN, where the positions of the defects were super-localized and their properties were characterized through emission spectrum. f-SRM in non-biological systems provide unique benefits, being faster and non-invasive.

For single-molecule reactions, we have demonstrated SR-SMLM as a powerful tool for resolving the multi-path reaction pathways of single spiropyran molecules. The capability to capture the spectra of randomly generated single fluorescent molecules over large areas may also be utilized to study other reactions and dynamic processes. For now, however, applications may be restricted to processes involving bright fluorescent molecules, and the achievable time resolution is limited to milliseconds.

In conclusion, by adding remarkably rich spectral and functional dimensions to the already powerful SRM, spectrally resolved and functional SRM opens up exciting new ways to probing biological and chemical systems at the single-molecule and nanoscale levels. We look forward to the continued development of related methods, as well as their application to a broad spectrum of research fields and scientific questions.

Part II

New microscopy approaches based on & for graphene

No microscopy technique is perfect by itself: it is thus possible to boost the performance by combining two or more methods. Correlative microscopy is an attempt to look at the sample with multiple microscopy methods for better understanding. In chapter 6, I present an easy correlative light-electron microscopy where the same specimen is investigated with fluorescence microscopy for molecular specificity and electron microscopy for superior spatial resolution. Graphene was employed to make the transition from light microscopy to electron microscopy seamless, as a protective layer that protects the samples under vacuum, and as a conductive layer for the electron microscopy.

The choice of fluorescent molecules (organic dyes or protein) is critical in fluorescent microscopy. The quality of a final image is determined by the performance of the dye, such as blinking kinetics and the brightness. In chapter 7, I present a strategy to broaden the choice of fluorescent molecules in live cell imaging. Here we introduced a graphene-based electroporator for adherent cell lines where organelle-specific fluorescent molecules are delivered into the cells. We also present the delivery of dye molecules in spatially-controlled manner, where a part of adherent cells were labelled selectively.

In chapter 8, I present re-engineering of old microscopy for the graphene itself. Due to its superb optical property, i.e. nearly transparent, it is hard to examine graphene and its defects on optical microscopy. We utilized Interference reflection microscopy (IRM), one of reflection-based microscopy that relies on reflection and interference to generate the image contrast. Although it was often used to study cell-substrate contact sites, it lost the popularity after 1980s due to the complexity of the sample. Here we optimized IRM for quantitative analysis of graphene on transparent substrate, and characterized nanoscale defects with superior contrast and high throughput.

Chapter 6

Graphene-enabled electron microscopy and correlated super-resolution microscopy of wet cells

The work in this chapter was conducted in collaboration with Michal Wojcik, Meghan Hauser, Wan Li, and Ke Xu. It is reproduced in part here from ref[6] with permission from all coauthors.

6.1 Introduction

As we discussed in Part I, fluorescence microscopy has been a popular choice for biological samples. Not only being a relatively easy and non-perturbing way of inspecting bio samples, it also provides molecular specificity through organelle-specific stains such as fluorescent proteins or antibodies. However, a major drawback of fluorescence microscopy is low spatial resolution. The conventional fluorescence microscopy provides few hundreds of nm resolution, often not enough to resolve a delicate sub-cellular target such as cytoskeleton. Despite of the advent of super-resolution microscopy in the last decade, the spatial resolution of optical microscopy is still few tens of nm, worse compared to that of other types of microscopy such as electron microscopy (EM).

To overcome the limitation, attempts to adopt strengths of other type of microscopy have been made. Correlative light-electron microscopy (CLEM) is such attempt to bridge light microscopy and electron microscopy, and takes advantage of the two methods. In CLEM, a sample is examined under a light microscopy (e.g. fluorescence microscopy) and electron microscopy, then the two images are carefully overlayed and correlated. Light microscopy provides an image of target with high specificity, but with lower resolution. Electron microscopy provides much a high-resolution image of cellular ultrastuctures, but often lacks

molecular specificity. The combination of two offers multidimensional insight of the sample and improved spatial resolution. Recent development of super-resolution microscopy further empower CLEM, as the spatial resolution of SRM, ∼20 nm, provides more meaningful correlation results[83].

A major challenge in the application of EM to biological samples has been faithful preservation of cellular ultrastructure during the laborious dehydration and embedding/coating procedures required for sample preparation[158–160]. The harsh procedures are also detrimental to fluorescence[161], thus introducing difficulties for correlating structural EM information with molecular specificity from high-resolution fluorescence microscopy, including super-resolution methods.[8,161–163] Quick freezing, as performed in cryo-EM methods, circumvents the need for dehydration[164,165], but requires dedicated equipment and is challenging for whole animal cells. Micro-fabricated liquid enclosures enable direct EM of hydrated cells[164,166–170], but such devices are difficult to fabricate, and the relatively thick (>∼50 nm) suspended viewing windows employed often limit the obtained contrast and resolution. Furthermore, the special substrates used in cryo-EM and liquid enclosures are difficult to adapt to oil-immersion lenses[170] for correlation with high-resolution optical microscopy methods.

Here we utilize graphene, a single-atom thick honeycomb lattice of carbon atoms[47], as an impermeable and conductive membrane to uniquely enable EM and correlated super-resolution microscopy of wet and untreated, or fixed mammalian cells cultured on conventional coverglass with exceptional ease. Despite being at the ultimate limit of membrane thinness, graphene is impermeable to gas and liquid[171–174], electrically and thermally conductive[47], and chemically inert. We previously reported the use of graphene for sealing surface-adsorbed molecules to interrogate their nano-structures with atomic force microscopy[103,104], and noted that graphene can seal nanoscale water droplets in ultra-high vacuum[175]. Other studies showed that graphene serves as an excellent transparent support film for EM[176,177], and can be used to entrap nanometer-scaled liquid to allow for EM of nanocrystals and protein in liquid[178–180]. EM of multilayer graphene oxide-wrapped bacteria has been achieved via mixing of liquid suspensions of bacteria and micrometer-sized graphene oxide flakes[174,181], but such approaches are difficult to apply to the much larger animal cells, and the sharp edges of graphenic flakes tend to penetrate the cell membrane and lead to internalization[182].

We report that monolayer graphene can hermetically seal and protect large areas of mammalian cells, cultured on conventional coverglass, from external environments, including the high vacuum typically encountered in an electron microscope. This protection, combined with the high electrical and thermal conductivity of graphene and its ultimate thinness, enables facile EM of wet and untreated cells with excellent contrast and resolution, as well as correlated super-resolution microscopy directly on the culturing substrate. In particular, individual actin filaments are resolved in wet cells through electron microscopy and well correlated with super-resolution results.

6.2 Result and discussion

6.2.1 Graphene insulates cells from the external environment

Graphene was produced by chemical vapor deposition (CVD) growth on copper foil and wet-transferred to cover large (∼10x10 mm^2) areas of cells conventionally cultured on coverglass (Figure 29a). Commercially available and homegrown graphene performed similarly in our experiments. Deposited graphene was identified in bright-field microscopy as a continuous, slightly darkened film (Figure 29b). Meanwhile, no noticeable impact is observed for the labeled fluorescence in cells (Figure 29c). Raman spectroscopy confirmed that the deposited graphene was a high quality monolayer (Figure 29d and Online Methods). The spectrum on graphene-covered cells had high background due to the labeled fluorescence in cells, but the 2D and G peaks of graphene[183] are nonetheless clearly resolved (Figure 29d).

To evaluate whether the monolayer graphene membrane can satisfactorily insulate cells from the external environment, fluorescently labeled cells were covered with graphene and then immersed in 0.1% sodium borohydride, a reducing agent commonly used to bleach fluorescence in biological samples, for 60 s (Figure 29ef). Cells not covered by graphene were bleached (e.g., white arrows), whereas cells protected by graphene retained fluorescence. This result indicates that graphene provided a hermetic seal for cells. Long-term (16 h) insulating capability was further confirmed through dye labeling experiments (SI in ref[6]).

6.2.2 Graphene enables electron microscopy of wet cells

Having verified that graphene can provide a hermetic seal for cells, we moved forward to examine its applicability to EM of wet cells under high vacuum conditions. Graphene sheets were deposited onto wet cells cultured on coverglass such that most of the coverglass surface was overlaid with graphene. Silver paint was used to contact a corner of the deposited graphene sheet to the sample holder for dissipation of electric charge during EM (Figure 30a, "Ag"). The sample was then loaded into a conventional scanning electron microscope (SEM) operated under standard secondary electron mode. Normal operational vacuum ($5x10^{-7}$ - $2x10^{-5}$ torr, depending on the particular system) was readily reached during pump down.

We first examined fixed cell samples that were briefly stained with a 0.5% uranyl acetate solution but otherwise remained fully hydrated. Under SEM, the non-covered, non-conductive parts of the sample rapidly accumulated electric charge, leading to excessively bright and unstable signals (Figure 30ab). Zoomed-in images (Figure 30b) displayed limited contrast and abnormal cell morphology attributable to structural deformation under vacuum. In contrast, graphene-covered regions are characterized by stable SEM signal with no indication of charge accumulation (Figure 30c). Graphene-covered cells can thus be imaged with good contrast over the entire field of view (Figure 30a) and at higher magnifications (Figure 30cd). Cell morphology was free of visible artifacts in all cases examined, indicating good preservation of cellular structures in vacuum. For cells that were fixed and membrane-extracted for preservation of the actin cytoskeleton[60,158,159], the obtained SEM

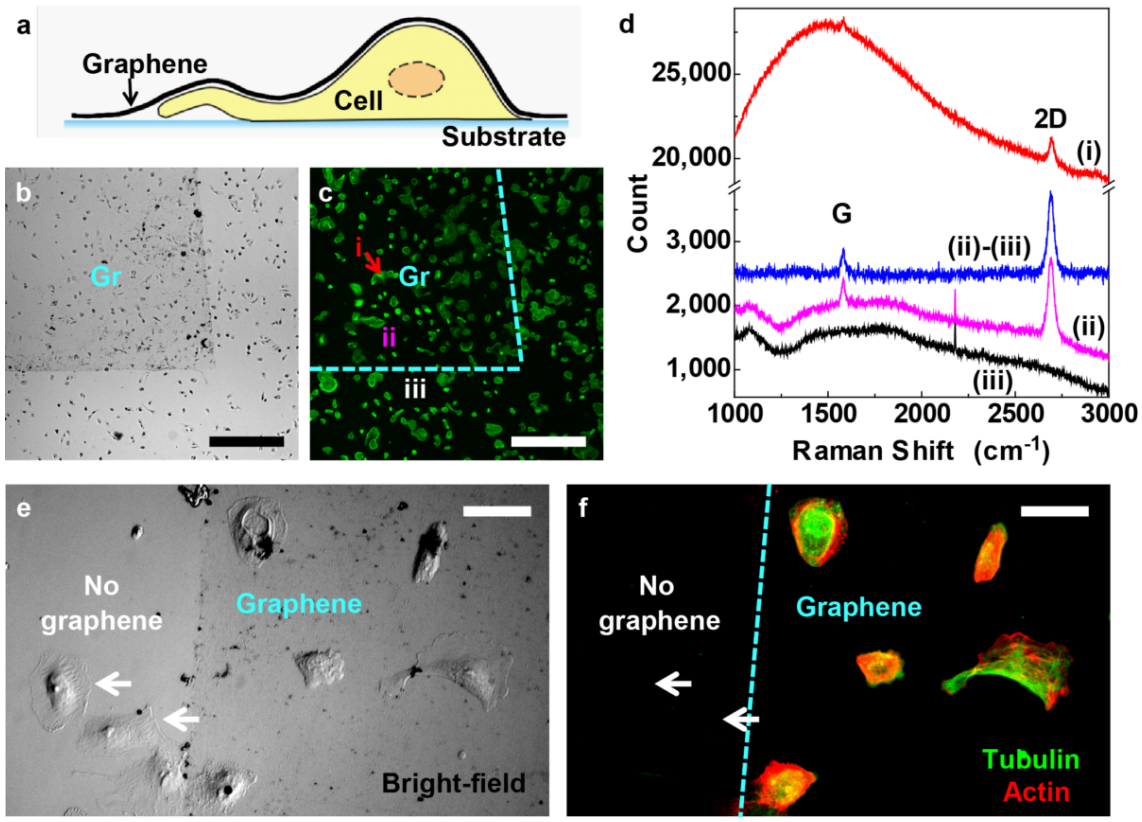

Figure 29: Graphene insulates cells from the external environment. (a) Schematic of our approach. (b,c) Graphene covering a region (Gr) of Alexa Fluor 488-phalloidin-labeled BS-C-1 cells on coverglass. (b) Bright-field microscopy. (c) Fluorescence microscopy of Alexa Fluor 488. (d) Raman spectroscopy for different areas of the sample: Graphene on top of cell (i), graphene off cell (ii), and substrate not covered by graphene (iii). (ii)-(iii) denotes spectrum (ii) after subtraction of spectrum (iii). (e,f) Graphene-covered (right 2/3) and non-covered (left 1/3) labeled (Green: Alexa Fluor 647-labeled tubulin; Red: Alexa Fluor 555-labeled actin) BS-C-1 cells, after exposure to a sodium borohydride bleaching solution. (e) Bright-field image. (f) Fluorescence image of the labeled tubulin (green) and actin (red). Scale bars: 0.5 mm (b,c); 50 μm (e,f).

images correlated well with conventional fluorescence images of phalloidin-labeled actin (SI in ref[6]) while providing finer structural details.

We then applied the same strategy to untreated live cells. At an accelerating voltage (V_0) of 3 kV, substantial contrast was obtained for the internal structure of the graphene-covered, untreated cells (Figure 30e). Void structures with low electron density, typically 200 nm – 2 μm in size, are observed in cells, likely corresponding to vesicle-like organelles that physically exclude the cytosol. Lower V_0 (2 kV) led to less transparent images, but was helpful in outlining the overall cell morphology (Figure 30f). At higher V_0 (5 kV), the untreated cells became overly transparent with only the nuclei providing contrast (Figure 30g). Previous studies using polyimide or silicon nitride membranes as imaging windows for EM of wet cells necessitate the use of high V_0 (>10 kV) to penetrate the relatively thick (>$\sim$50 nm) membranes, thus providing limited contrast on unstained animal cells10-12. As

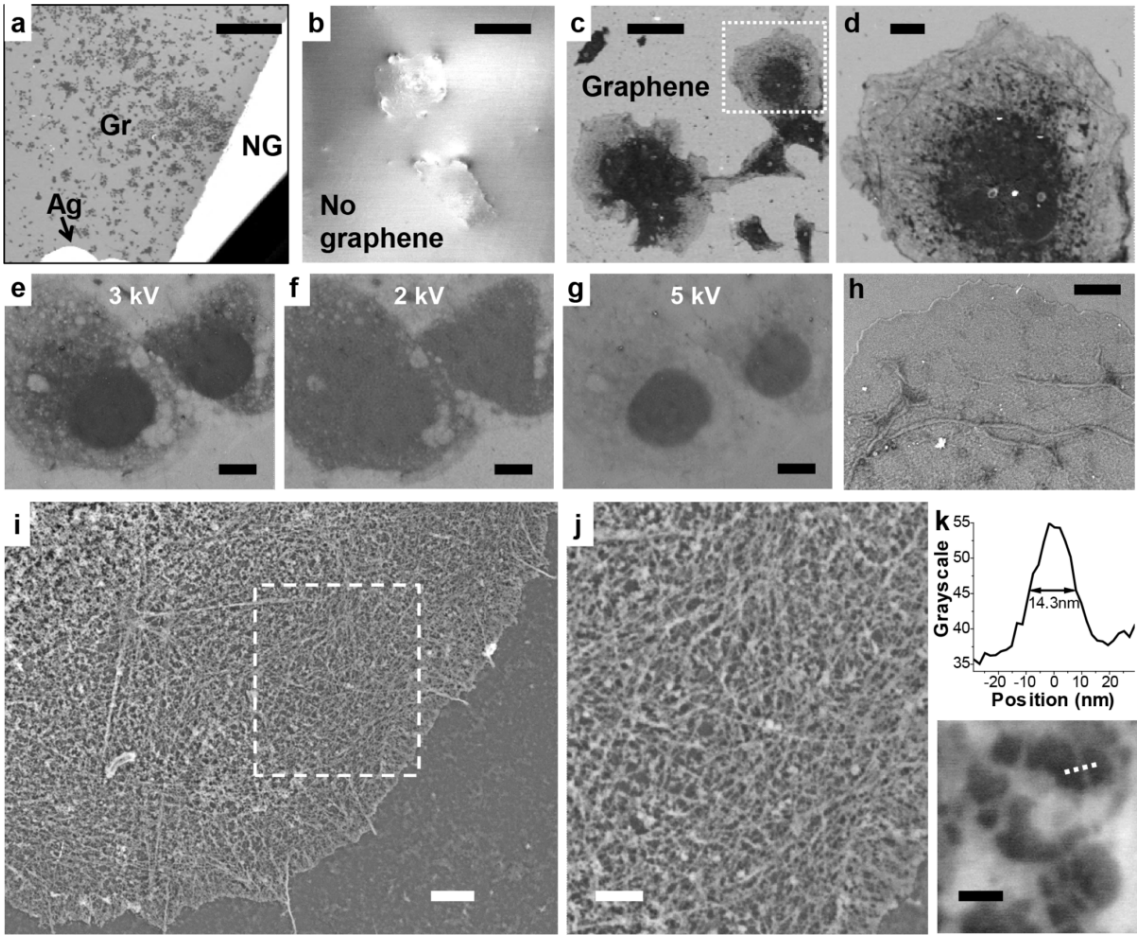

Figure 30: Graphene-enabled electron microscopy of wet cells. (a) Zoom-out SEM image of graphene-covered (Gr) and non-covered (NG), fixed and lightly stained wet COS-7 cells on coverglass. (b) Non-covered cells at higher magnification (V_0 = 2 kV). (c) Graphene-covered cells in the same sample, image taken under the same conditions as b. (d) Zoom in of c. (e-g) SEM images of graphene-covered, untreated live COS-7 cells, taken at V_0 = 3, 2, and 5 kV, respectively. (h) SEM image of a graphene-covered, fixed wet COS-7 cell that was stained with 2% uranyl acetate (V_0 = 4 kV). (i) SEM image of a graphene-covered, wet COS-7 cell that was fixed and membrane-extracted for preservation of the actin cytoskeleton and stained with tannic acid and uranyl acetate. V_0 = 5 kV. (j) Zoom-in of i. (k) Close-up of a sparse region, and cross section through one filament along the dotted line. Scale bars: 1 mm (a); 50 μm (b,c); 10 μm (d-g); 4 μm (h); 2 μm (i); 1 μm (j); 100 nm (k).

an ultrathin membrane, graphene interacts minimally with the electron beam[176,177] and thus allows for cell imaging at much lower V_0. The fact that graphene is an excellent thermal and electrical conductor further reduces damage by the electron beam so that the same unfixed cells can be imaged multiple times and under different conditions without noticeable structural changes (Figure 30e-g).

Enhanced image contrast was obtained for wet samples that were suitably fixed and stained. For fixed cells that were not membrane-extracted, staining with a 2% aqueous

solution of uranyl acetate revealed the structural details of the plasma membrane and mitochondria (Figure 30h). For samples fixed and membrane-extracted for preservation of the actin cytoskeleton[60,158,159], a two-step staining with tannic acid and uranyl acetate solutions[159,166] led to excellent contrast under graphene, enabling EM of individual cytoskeletal actin filaments in hydrated samples for the first time (Figure 30ij and SI in ref[6]). Line scans over single filaments produced cross-sectional widths of ∼14 nm (Figure 30k), close to the known diameter of actin filaments (8 nm) and limited by the achievable resolution of the SEM systems we used. The obtained outstanding resolution and contrast are again attributed to the ultimate thinness of graphene. As a uniform, single layer of carbon atoms, graphene causes minimal electron scattering[176,177] and is thus instrumental in revealing the detailed structures of the covered cells.

6.2.3 Correlative super-resolution and electron microscopy

Due to its compatibility with wet samples on standard coverglass, our method can be readily extended to allow for correlative[8,161,162] super-resolution and electron microscopy. Here we used three-dimensional stochastic optical reconstruction microscopy (3D-STORM)[7,25] to first resolve actin filaments in fixed wet cells on coverglass[7,25,101], and then uranyl-stained the sample and applied graphene for correlated SEM imaging. Comparison of the 3D-STORM and graphene-SEM images shows good correspondence of actin ultrastructure, enabling correlation of individual actin filaments between super-resolution and EM images (Figure 31ab and SI in ref[6]). Excellent correlative STORM/graphene-SEM results were also obtained for the cell membrane in unstained cells (Figure 32) and for mitochondria in stained cells (Figure 31c and SI in ref[6]). Figure 3d further shows a case in which actin filaments and mitochondria are both visualized in the same sample. Two-color STORM images show good correlation with SEM for both structures. Furthermore, good agreement is obtained between the scale bars obtained from STORM and SEM measurements in all cases, confirming preservation of volume and size of wet cells in vacuum (Figure 31, 32, and SI in ref[6]). Taken together, these results indicate preservation of fine structural details in graphene-covered wet samples.

6.3 Conclusion

A considerable obstacle in EM of cell samples has been achieving proper preservation of fine cellular structure during the conventionally required sample dehydration procedures. Both air- and freeze-drying lead to major distortions (e.g., SI in ref[6])[158,159]. Dehydration through a graded series of organic solvents followed by critical-point drying and platinum/carbon deposition has been successful, but is technically challenging and time consuming[159]. By taking full advantage of the extraordinary properties of graphene as the thinnest membrane that is impermeable and conductive, our approach allows for direct EM of wet cells through a simple, one-step sample preparation. No special substrate, device, or equipment is involved, and good contrast and resolution are achieved with conventional SEM. Its ready application to

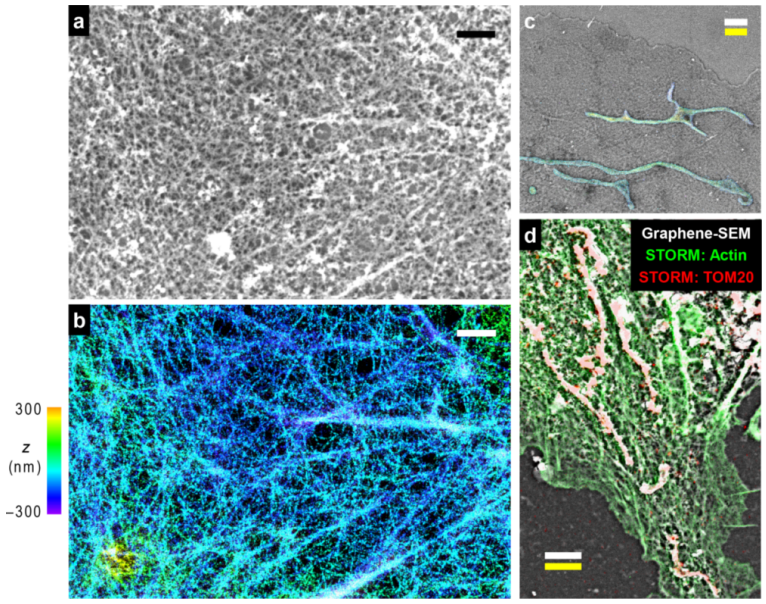

Figure 31: Graphene-enabled correlated super-resolution and electron microscopy of wet cells. (a,b) Correlated graphene-SEM (a) and 3D-STORM (b) images of the actin cytoskeleton in a wet, fixed and membrane-extracted COS-7 cell. (c) Correlated and overlaid graphene-SEM and 3D-STORM images of a wet, fixed COS-7 cell that was not membrane-extracted (Figure 30h). For STORM, the sample was immunolabeled for TOM20, a mitochondrial outer-membrane marker. (d) Correlated and overlaid two-color STORM (green for actin; red for TOM20) and graphene-SEM (white) images for another membrane-extracted fixed cell. Color scale in b is used to indicate height (z) in b,c. Scale bars: 1 μm (a,b); 2 μm (c,d). White and yellow scale bars in c,d correspond to scales obtained from graphene-SEM and STORM, respectively.

cells cultured on standard coverglass further permits facile correlation with super-resolution microscopy for multiple targets in unstained and stained cells. Our approach thus opens up new ways to examine biological samples at the nanoscale in their native, hydrated state.

6.4 Materials and Method

Cell culture and immunofluorescence labeling

Mammalian cells (BS-C-1, COS-7, HeLa; ATCC) were cultured on common glass coverslips (typically 12 mm dia.) following standard tissue culture protocols. For live cell experiments (Figure 30e-g), cells were left untreated before the application of graphene. For correlated STORM and graphene-SEM of unstained cells (Figure 32), live cells were labeled with a CM-DiI cell membrane-labeling solution (Invitrogen V-22888) at 20 μM in DMEM for 5 min, and then fixed by 4% paraformaldehyde for 10 min. For experiments aimed at visualizing the actin cytoskeleton (Figs. 2a-d, 2i-k, 3abd, SI in ref[6]), cells were initially fixed and extracted for 1 min with a solution of 0.3% (v/v) glutaraldehyde and 0.25% (v/v) Triton X-100 in cytoskeleton buffer (CB, 10 mM MES, pH 6.1, 150 mM NaCl, 5 mM EGTA, 5 mM

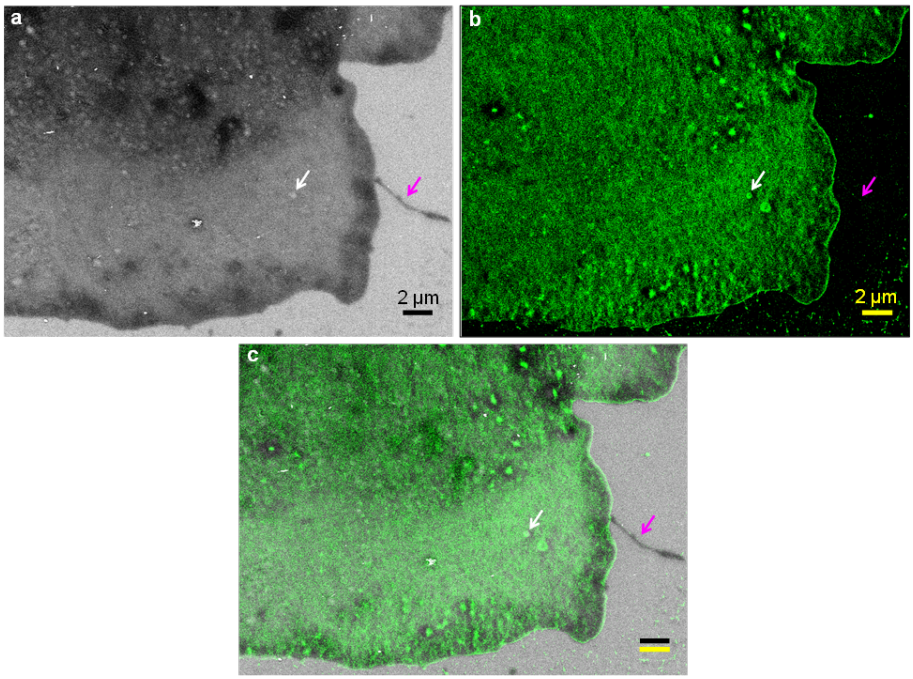

Figure 32: Correlated STORM and graphene-SEM results for an unstained wet cell. Live COS-7 cells were labeled with a DiI cell membrane-labeling solution (Invitrogen V-22885) at 20 μM in DMEM for 5 min, and then fixed by 4% paraformaldehyde. a, Graphene-SEM image. V0 = 2 kV (for best contrast of cell shape). b, Correlated STORM super-resolution image of the labeled DiI, imaged with a 560 nm laser. c, Overlaid image. Black and yellow scale bars correspond to scales obtained from graphene-SEM and STORM, respectively. White arrow points to a vesicle that is visualized in both the graphene-SEM and STORM images: This is likely due to the local internalization of the cell membrane (e.g., endocytosis) during dye labeling of the live cell. Meanwhile, many other vesicles are observed in the graphene-SEM image but not in the STORM image: these are likely internal vesicles that are not labeled by the DiI solution. Occasionally observed clusters in the STORM image are attributed to undissolved DiI aggregates. Magenta arrow points to a structure that is visualized in graphene-SEM but barely visible in STORM due to the low labeling of DiI therein.

glucose and 5 mM $MgCl_2$), and then post-fixed for 20 min in 2% (v/v) glutaraldehyde in CB[60,158,159]. For other fixed-cell experiments, cells were fixed in 3% formaldehyde and 0.1% glutaraldehyde in phosphate buffered saline (PBS) for ∼10 min. For immunofluorescence labeling, cells were first blocked with a solution of 3% bovine serum albumin and 0.1% Triton X-100 in PBS, and then stained with corresponding primary and secondary antibodies. Primary antibodies used were mouse anti-tubulin (Sigma T5201; 1:400) for labeling of microtubules and rabbit anti-Tom20 (Santa Cruz sc11415; 1:200) for labeling of mitochondria. For single-color and two-color STORM imaging of mitochondria, AF647-conjugated and Cy3B-conjugated34 secondary antibodies (at 5 μg mL_{-1}) were used to label Tom20, respectively. For fluorescent labeling of actin filaments, samples were incubated[60] with AF488-conjugated phalloidin (Invitrogen A12379; for Figure 29c), AF555-conjugated phalloidin (Invitrogen A34055; for Figure 29f), or AF647-conjugated phalloidin (Invitrogen A22287; for all other data) at a concentration of ∼0.4 μM.

Staining for EM

For data presented in Figure 30a-d and SI in ref[6], fixed and membrane-extracted cells were stained with 0.5% uranyl acetate (SPI 02624) in water for 5-10 minutes, washed three times with water, and kept in water prior to graphene deposition. For imaging of mitochondria and plasma membrane (Figs. 30h, 31c), fixed cells were stained with 2% uranyl acetate in water for 1 h. For improved contrast of the actin cytoskeleton (Figs. 30i-k, 3ad), samples were treated with 5% tannic acid (Sigma 403040) in water for 5 min, followed by a solution of 2% uranyl acetate in water for 2 hours. Samples were thoroughly washed with water and kept in water prior to graphene deposition.

Graphene deposition

CVD graphene on copper foil[184] were grown at Cornell NanoScale Science & Technology Facility (CNF) or purchased from Graphene Supermarket (Calverton, NY). Similar results were obtained using graphene from the two sources. The CVD graphene on copper foil was spin-coated with a ∼150 nm layer of polymethyl methacrylate (PMMA), and cut into pieces slightly smaller than the size of the coverslip. After the copper was removed in 10% ferric chloride, the graphene-PMMA stack was transferred to a fresh water bath so it floated on the water surface. Water bath transfer was repeated three times to remove traces of ferric chloride. To cover cells with graphene, the hydrated coverslip containing the cells was used to scoop up the graphene-PMMA stack floating on water. The stack was allowed to adhere to the sample for ∼10 min in air. To remove PMMA, the sample was dipped in anisole or acetone for 2 min, and rinsed off briefly in isopropyl alcohol. Deposited graphene was identified in bright-field microscopy as a continuous, slightly darkened film (Figure 29b), likely due to the known absorption of graphene to 2.3% of white light[185]. Near 100% yield was achieved. Quality of graphene was evaluated via Raman spectroscopy. Raman spectra were recorded with a Renishaw InVia micro-Raman system using a 488 nm laser and a 2400 lines/mm grating. A confocal microscope with a 50x objective lens was used to record spectra at a spatial resolution of ∼2 μm. Raman spectroscopy confirmed that the graphene used in this study was high quality monolayer (Figure 29d and SI in ref[6])[183]. We have also found that small amounts of bilayers do not notably affect our results, but low-quality graphene with excessive bilayers and defects is not optimal for obtaining the best results with our method (SI in ref[6]).

SEM imaging

The graphene-covered coverslip was mounted on a standard metallic sample mount with carbon tape, and a small amount of silver colloid paint (Ted Pella 16031) was used to create a conductive bridge between graphene and the sample mount. SEM imaging was performed under standard secondary electron mode on a FEI Quanta 3D FEG system or a JEOL JSM-6340F system. Normal operational vacuum (5x10 $^{-7}$-2x10 $^{-5}$ torr) was readily reached during

pump down. Calibration of magnification was verified with a replica of a 2,160 lines/mm waffle-pattern diffraction grating (Ted Pella 604-A).

Correlative STORM/Graphene-SEM imaging

To facilitate location of the same cells under STORM and SEM, a diamond scribe was used to make a scratch mark (e.g., $\sim$1 mm^2 triangular) at the center of the coverslip, which was readily identifiable both under optical microscope and in SEM under the coverage of graphene. 3D STORM imaging[7,25] was first performed on a homebuilt setup based on a Nikon Eclipse Ti-U inverted optical microscope using an oil immersion objective (Nikon CFI Plan Apochromat λ 100x, NA 1.45). Briefly, lasers at 647 nm (MPB Communications), 560 nm (MPB Communications), and 405 nm (Coherent) were coupled into an optical fiber after an acousto-optic tunable filter and then introduced into the sample through the back focal plane of the microscope. Using a translation stage, the laser beams were shifted toward the edge of the objective so that emerging light reached the sample at incidence angles slightly smaller than the critical angle of the glass-water interface. Continuous illumination of 647-nm laser ($\sim$2 kW cm^{-2}; for STORM of AF647) or 560-nm laser ($\sim$2 kW cm^{-2}; for STORM of Cy3B and CM-DiI) was used to excite fluorescence from labeled dye molecules and switch them into the dark state. Concurrent illumination of the 405-nm laser was used to reactivate the fluorophores to the emitting state. The power of the 405-nm laser (typical range 0-1 W cm^{-2}) was adjusted during image acquisition so that at any given instant, only a small, optically resolvable fraction of the fluorophores in the sample were in the emitting state. For 3D STORM imaging, a cylindrical lens was inserted into the imaging path so that images of single molecules were elongated in x and y for molecules on the proximal and distal sides of the focal plane (relative to the objective), respectively[25]. Imaging buffer used was Tris-Cl containing 100 mM cysteamine, 5% glucose, 0.8 mg mL^{-1} glucose oxidase, and 40 μg mL^{-1} catalase. After STORM imaging, the coverslip was stored in PBS before processing for graphene-based SEM imaging (as described above). To align the obtained STORM and SEM images, the STORM image was mapped to the coordinate system of the SEM image through a two-dimensional affine spatial transformation (MATLAB) on the basis of corresponding features (control points). About 20 control points were selected in each dataset for inferring an averaged, global, affine transformation matrix.

Chapter 7

Spatially controlled electroporation on graphene substrate for live-cell imaging

The work in this chapter was conducted in collaboration with Wan Li and Ke Xu.

7.1 Introduction

In fluorescence microscopy, choice of fluorescent marker is critical as a means of achieving molecular specificity and a high-quality image. For bioimaging, it is often necessary to incorporate exogenous genes or probes to visualize a target of interest. In particular, for the emerging field of super-resolution microscopy (SRM) of live cells, reliable fluorescent labeling of intracellular targets remains a challenge[186]. Although the intracellular gene expression of fluorescent proteins (FPs) is relatively straightforward, FPs offer limited photostability and photon counts, and so generally do not perform as well for SRM when compared to organic dyes[187]. On the other hand, high-performance dye-based probes for SRM often do not readily cross the strong barrier created by cell plasma membrane[188], and thus rely on membrane-disruption techniques for intracellular delivery[189,190].

Although chemical permeabilization, including the use of mild detergents[191–193] and toxins[194,195] provides relatively easy means of intracellular delivery, recovering membrane integrity is often challenging and requires special attention[193,195,196]. Microinjection[197,198] provides a controlled means for intracellular delivery through physical penetration, but is limited in throughput and highly dependent on operator's skill. Sonoporation[199,200] and electroporation[201,202] create small, resealable pores on the cell membrane via sonic waves and electric fields, with the latter being now routinely used for transfection owing to its high efficiency and low cell toxicity[203,204]. However, electroporation are typically performed for detached and (re-)suspended cells. For the delivery of external fluorescent probes, the long ($>\sim$10 h) subsequent re-plating time, which is essential for the cells to re-adhere to the substrate for high-resolution imaging, is inconvenient and potentially gives rise to undesired side effects

due to the prolonged introduction of probe molecules.

Recent advances in nanotechnology and microfluidics have led to the exciting development of numerous new intracellular-delivery methods[205–211]. However, implementation is often difficult, and above all, they often do not enable high-resolution microscopy on the same device immediately after the delivery.

Here we introduce a graphene-based facial approach for the direct, high-throughput delivery of fluorescent probes into adherent cells to enable *in situ* live-cell SRM on the same device within minutes. Recent years have witness great research interest in interfacing graphene, a monolayer of bonded carbon atoms, with cell biology[212–214]. We recenly demonstrated the use of graphene to encapsulate mammalian cells to enable correlated electron microscopy and SRM[6]. In this work, we utilized the outstanding mechanical, electrical, and optical properties of graphene to enable cell culturing, electroporation-based probe delivery, and SRM imaging all on the same device. ∼90% delivery efficiency is thus demonstrated for free dye molecules as well as dye-labeled affinity probes, short peptides, and whole antibody. Moreover, we demonstrate unique spatial and temporal controls through the easy patternablity of graphene, achieveing spatially selective delivery of two different probes for different regions of the same substrate.

7.2 Result and discussion

7.2.1 Graphene-based electroporator delivers a small organic dye into cells with excellent efficiency

Monolayer graphene, as produced by chemical vapor deposition on copper foils[215], was deposited onto regular glass coverslips as ∼8x10 mm^2 square pieces, sealed with a small plastic tube, and contacted at the edges with silver paint. Two-point measurement showed resistance of a few kΩ across the as-prepared devices. Interference reflection microscopy (IRM) was employed to further confirm that graphene in the final device to be continuous monolayers with minimal defects[5]. Adherent mammalian cells (A549 and PtK2 cells) were cultures on the graphene surface under standard tissue culturing conditions. Previous work ahs shown the graphene surface to be suitable for cell growth[216,217]. Meanwhile, the measured graphene resistance increased moderately to ∼10 kΩ after ∼1 day growth (Figure 33c).

At the time of probe delivery, the culture medium is replaced with a commercial electroporation buffer solution that contained the fluorescent probes for delivery. Counter electrode was made out of a metal pin-stub mount commonly used in scamming electron microscopy (SEM), which was mounted upside-down with the application of ∼400 μm-thick Teflon tape on the rim as an insulating spacer. This counter electrode was gently placed into the device, and the device was mounted onto an inverted fluorescence microscope (Figure 33a). Scanning the focus of the microscpe indicated that the distance between the counter electrode and graphene surface was ∼500 μm.

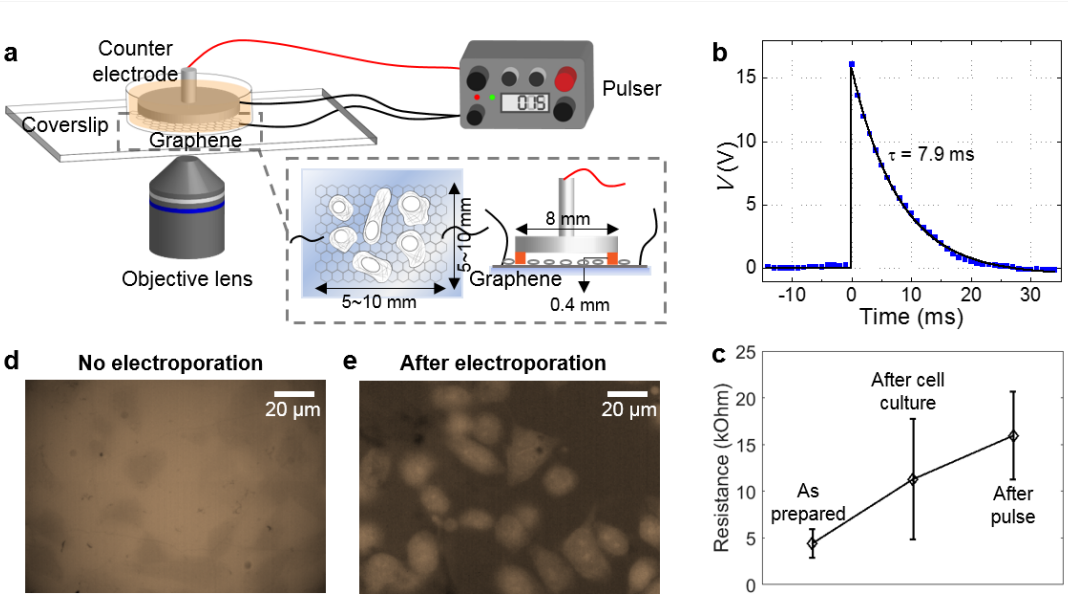

Figure 33: Electroporation of adherent cells on a graphene-covered glass coverslip. (a) Schematic of the experimental setup. (b) A representative pulse shape, as measured from an oscilloscope. (c) Measured two-point resistance of graphene for the as-prepared device, after culturing of adherent cells, and after electroporation (N = 4 measured devices). (d) Fluorescence micrograph of PtK2 cells incubated in a medium containing SR101 for 10 minutes; cells appear as darker regions due to the physical exclusion of the dye. (e) Fluorescence micrograph of PtK2 cells grown on the graphene surface after the application of the voltage pulse, 10 min incubation time, and wash out of free dyes.

For electroporation, we applied a voltage pulse across the graphene and counter electrodes through capacitor discharging using a commercial electroporator. Remarkably, efficient probe delivery (below) was readily achieved at low voltages (∼10-15 V) using a small (10 μF) capacitor, at typical pulse halftimes of ∼5-10 ms (Figure 33b). The very low voltages, in comparison to the often >1000 V voltages used in commercial electroporation protocols, were attributed to the small (∼500 μm) distance between the two electrodes, as well as the fact that here the cells adhered to the graphene electrode surface. A mild increase in graphene resistance was noted after the electroporation process (Figure 33c), and IRM showed the generation of minor cracks in graphene.

We started with the delivery of a free organic dye, Sulforhodamine 101 (SR101, molecular weight: 606.7). As SR101 is not normally taken up by PtK2 cells, microscopy of cells in a medium containing this probe showed lower local fluorescence for cell-occupied areas owing to physical exclusion (Figure 33d). After electroporation in the graphene device, 10 min of incubation, and washout of free dyes with the culture medium, we found the cytoplasm of most cells became fluorescent due to the incorporation of SR101 (Figure 33e).

7.2.2 Delivery of fluorescent probes for super-resolution microscopy

We next tested dye-tagged probes that bind to specific intracellular targets, starting with phalloidin-Alexa Fluor 488, a small (∼1.3 kDa), highly specific fluorescent marker for the actin cytoskeleton. As expected, the probe itself was non-permeable for A549 cells, and so cells initially appeared as darker regions in fluorescence micrographs due to physical exclusion (Figure 34a). After the application of electroporation voltage pulse, the cells quickly lightened up within ∼1 min (Figure 34bd), and continued to rise in fluorescent signal over time (Figure 34cd). Low-magnification images showed, over large areas, most cells on the graphene surface to be efficiently labeled, whereas in the same view, cells on the bare glass substrate remained unlabeled (Figure 34i).

We next turn to the challenging task of dye-tagged whole immunoglobulin G (IgG) antibodies. Whereas antibody fluorescence labeling (immunofluorescence) is routine and favorable for SRM of fixed and permeabilized cells for its versatility, its use in live-cell microscopy and SRM has been rare due to difficulties in delivering the sizeable (∼155 kDa) IgG molecules into the cell. We found graphene-based electroporation enabled efficient delivery of dye-tagged IgGs, *e.g.* Alexa Fluor 647-tagged IgG against vimentin (Figure 34e-g), although the increases in intracellular labeling were slightly slower (Figure 34e-h) when compared to that of phalloidin, possibliy attributable to the lower diffusion rates of IgGs owing to their heavy molecular weight. Low-magnification images further showed that similar to that with phalloidin, highly efficient and selective labeling was achieved for cells grown on the graphene surface (Figure 34j). Correlating transmission and fluorescence micrographs showed ∼80-90% of cells on the graphene surface to be successfully labeled (Figure 34k) for the cases of phalloidin, anti-vimentin IgG, SR101, as well as Cy5-tagged Lifeact, a 17-amino-acid peptide that reversely bind to actin filaments[218]. Together, we thus have shown our graphene-based electroporation allowed for the intracellular delivery of small to big non-permeable probes into adherent cells with high efficiency and good spatiotemporal control.

Based on the above good delivery results, we next demonstrate the use of our system for *in situ* live-cell STORM SRM in the same device immediately after probe delivery. For this experiment, we expect to utilize the unique properties of graphene that although it is highly conductive, it is just a single layer of atoms and is highly transparent to light, so that we should be able to perform high-resolution microscopy directly through the graphene electrode with minimal issues. Thus, after electroporation delivery of STORM-compatible probes, we replaced the cell medium with a live-cell STORM imaging buffer[188], and mount the device on a 3D-STORM system equipped with a 100x, oil-immersion objective lens.

Conventional epi-fluorescence images taken at low illumination powers, e.g., for vimentin filaments labeled in live A549 cells through the graphene-electroporation delivery of AF647-tagged IgG, showed no signs of distortion when imaging through the graphene electrode (Figure 35a). By next increasing the illumination power, we photoswitched most of the labeled probe molecules into a non-emitting dark state. The reversible photoswitching of these molecules between the dark and emitting states led to well-resolved, bright single-

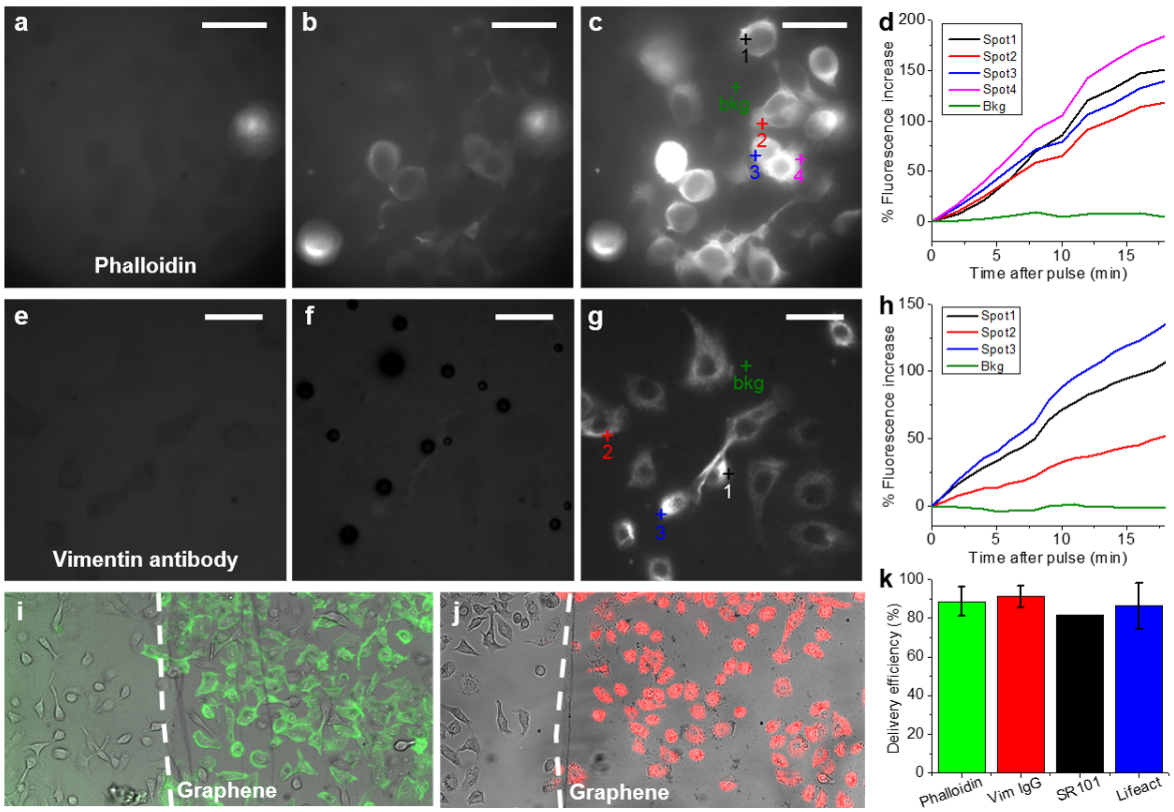

Figure 34: Delivery of dye-tagged probes that bind to specific intracellular targets. (a-c) Delivery of phalloidin-AF488 into A549 cells through graphene electroporation. (a) Fluorescence micrograph of the sample before the application of the voltage pulse. (b,c) Fluorescence micrographs for the same area 1 min (b) and 20 min (c) after the voltage pulse. (d) Increase in local fluorescent intensity over time after the voltage pulse, for the different spots marked in (c). (e-g) Delivery of AF647-conjugated anti-vimentin full IgG antibody into A549 cells. (e) Fluorescence micrograph before the voltage pulse. (f,g) Fluorescence micrographs for the same area 1 min (f) and 20 min (g) after the voltage pulse. (h) Increase in local fluorescent intensity over time after the voltage pulse, for the different spots marked in (g). (i) Merged transmission (grayscale) and fluorescence (green) micrographs for the spatially controlled delivery of phalloidin in A549 cells adhered to graphene (to the right of the dashed line) vs. no delivery to cells on the bare glass surface without graphene (left of the dashed line). (j) Similar results for the spatially controlled delivery of anti-vimentin IgG (red). (k) Percentage of cells being labeled for phalloidin (N = 7), anti-vimentin IgG (N = 4), SR101 (N = 1), and Lifeact (N = 4), as determined from correlated transmission and fluorescence micrographs. Error bars: standard deviation between samples. Scale bar 20 μm

molecule fluorescence (Figure 35b) that "blinked" stochastically in space and time, for which we recorded continuously at 110 frames per second. Analysis of the distribution of photon counts of all single molecules (Figure 35d) gave an average of 4,800 photons, in agreement with that typically obtained with AF647. Integrating the 3D localizations[142] obtained for ~47,000 frames of single-molecule images led to 3D-STORM SRM images of high resolution (Figure 35c). For the single vimentin intermediate filament pointed to by the red arrow in

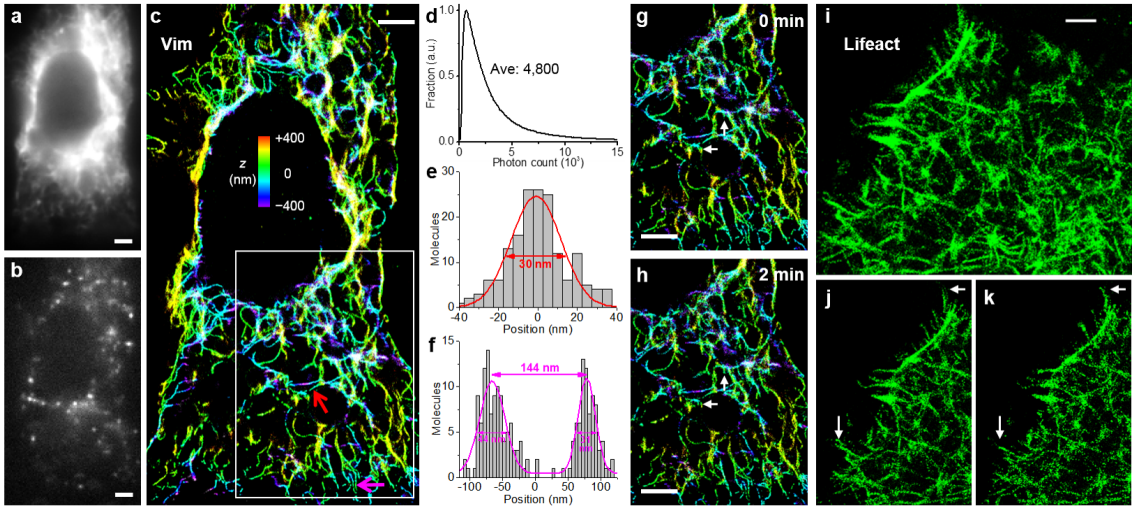

Figure 35: STORM SRM through fluorescent probes delivered by graphene electroporation. (a) Diffraction-limited image of vimentin in live A549 cells labeled through the graphene-electroporation delivery of an AF647-tagged IgG antibody. (b) A typical frame of single-molecule images during STORM acquisition. (c) Resultant 3D-STORM image. Color presents the depth (z) information (color scale bar). (d) Distribution of the photon count for each single AF647 recorded in the data. (e) Cross-sectional profile of the single vimentin filament pointed to by the white arrow in (c). Fit to a normal distribution gave FWHM of 30 nm. (f) Cross-sectional profile for two adjacent filaments pointed to by the magenta arrow in (c). (g,h) A sequence of two STORM images at 0 min (g) and 2 min (h). Arrows point to structural changes at the nanoscale. (i) STORM image of actin filaments in live A549 cells labeled through the graphene-electroporation delivery of Lifeact-Cy5. (j,k) A sequence of two STORM images at 0 min (j) and 1.5 min (h). Arrows point to structural changes at the nanoscale. Scale bar 2 μm

Figure 35c, cross-sectional profile gave a FWHM (full width at half maximum) width of 30 nm (Figure 35e), consistent with a convolution of the ∼20 nm spatial resolution of STORM with the ∼20 nm diameter of vimentin filament labeled by IgG. Figure 35f further shows a case in which two filaments are clearly resolved at a center-to-center distance of 144 nm, well below the diffraction limit. Subdividing the collected frames of single-molecule images to construct a sequence STORM images further enabled the scrutiny of nanoscale structural changes over time (Figure 35gh). Good live-cell STORM SRM was also achieved in live A549 cells for the actin cytoskeleton labeled by Lifeact-Cy5 (Figure 35i-k) and phalloidin-AF647.

7.2.3 Spatially controlled, patterned delivery of fluorescent probes

We next further exploit the spatial and temporal control of our graphene-based approach to enable patterned delivery of two different probes. As a first demonstration, we made a ∼20 μm-wide scratch at the center of graphene to divide it into top and bottom halves (Figure 36a-d), which were each separately contacted by a metal wire. Conductance measurements indicated that the two halves were electrically isolated. After similarly plating the cells, we replaced the culture medium with an electroporation buffer that contained

AF647-conjugated anti-vimentin antibody, and applied a 15 V pulse only to the bottom half of the graphene electrode against the counter electrode. After ∼15 min incubation, the cells were allowed to recover in a medium containing 2 mM ATP and 2% glucose at 37 °C for ∼20 min[195]. Medium was then replaced by another electroporation buffer that contained phalloidin-CF568, and a 15 V pulse was applied to the top half of the graphene electrode. Remarkably, the above sequential electroporation procedure enabled patterned delivery, so that fluorescent micrographs taken in the AF647 and CF568 channels showed that the former was specifically delivered to cells on the bottom half of the graphene electrode (Figure 36e-g;k-m), whereas the latter was specifically delivered to cells in the top half of the device (36h-m). Interestingly, we further found that the spatial specificity for the second probe relied on the proper recovery (sealing) of the plasma membrane after the first electroporation step. Skipping this recovery step led to nonspecific delivery into the unsealed cells due to the first electroporation step.

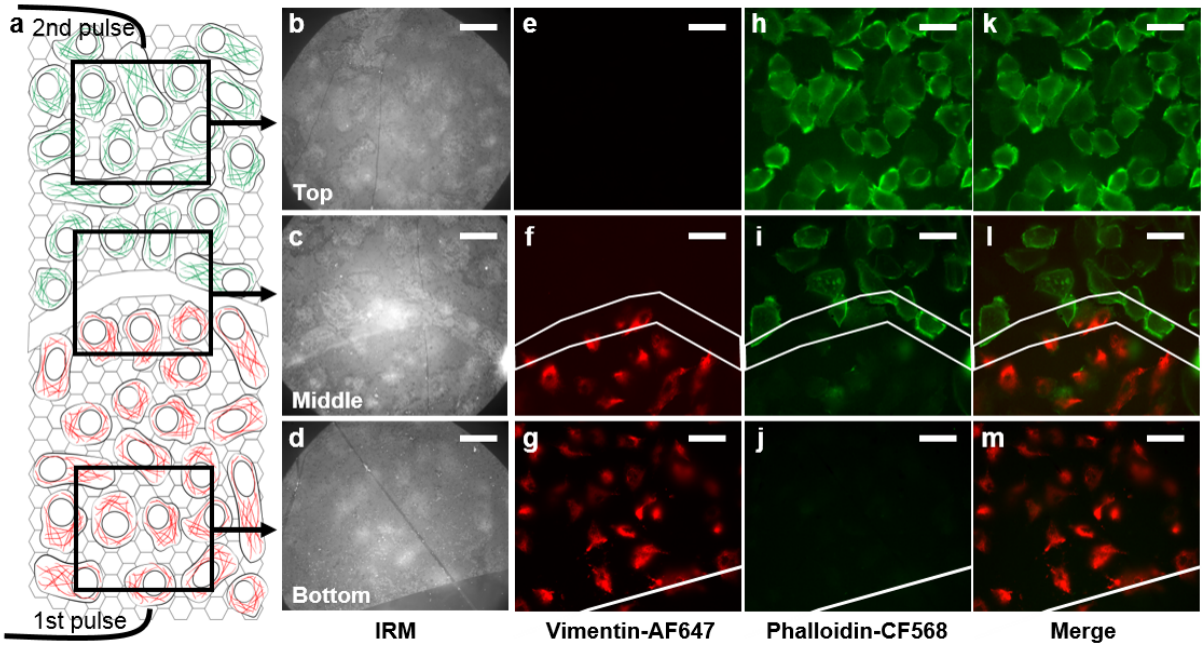

Figure 36: Patterned delivery of two different probes for cells adhered to different regions of the same substrate. (a) Schematic of the sample with a scratch through the graphene electrode that divided it into two halves. A voltage pulse was first applied to the bottom half in the presence of the first (red) fluorescent probe, cells were recovered for 30 min, and then a second voltage pulse was applied to the top half in the presence of the second (green) fluorescent probe. (b-d) IRM images of graphene and A549 cells for the top (b), middle (c), and bottom (d) parts of the sample, as schematized in (a). (e-g) Fluorescence micrographs for the same areas as (b-d), for the channel of the first fluorescent probe (AF647-tagged anti-vimentin IgG antibody). White lines in (f) mark the edges of the top and bottom electrodes. (h-j) Fluorescence micrographs for the second fluorescent probe (phalloidin-CF568) for the same areas. (k-m) Merge of the two color channels. Scale bar 20 μm

7.3 Conclusion

In summary, we have developed an integrated system that enables the facile electroporation delivery of fluorescent probes into adherent mammalian cells for immediate single-molecule detection and SRM on the same platform. High (∼90%) delivery efficiency was achieved with low pulse voltages for from free dye molecules up to full IgG antibodies, and the outstanding optical properties of graphene enabled high-quality fluorescence microscopy with oil-immersion objectives. Moreover, we demonstrated unique spatial and temporal controls, achieving patterned delivery of two different probes for different regions of the same substrate with high selectivity. By removing the need to detach and then re-adhere the cells to coverslips for high-resolution microscopy, as required by typical electroporation methods, our *in situ* approach greatly expedites labeling and reduces the potential adverse effects due to prolonged retention of external probes inside live cells. Finally, whereas in this work we have focused on probes based on organic dyes for their ease of visualization, our approach may also enable the delivery of other probes or chemicals, including drugs, into live cells. By being able to deliver different chemicals to different, spatially predefined subsets of cells on the same substrate under the same conditions, a well-controlled, multiplexed platform may thus be constructed for the quantitative examination of drug effects with high-resolution microscopy.

7.4 Materials and Method

Graphene deposition and assembly for cell culture

CVD graphene was transferred on glass substrate by wet-transfer method with PMMA (polymethyl methacrylate) protection as previously described[5]. CVD graphene on a copper foil was purchase from Graphene supermarket and was spin coated with ∼100 nm layer of PMMA. The graphene-PMMA stack was cut into a small square piece (∼8 x 8 mm), and the copper was removed in an etching solution (5% HCl + 20% $FeCl_3$). The stack piece was transferred to a fresh water bath to remove traces of ferric chloride for three times. The graphene-PMMA film is then transferred to a pre-cleaned glass coverslip (24 x 60 mm, Thickness #1.5), and air-dried for ∼30 min. PMMA layer was dissolved and removed in anisole and acetone for 3∼5 min, and residues were further rinsed in isopropanol for 3∼5 min. Sample was completely dried under nitrogen gas. To connect graphene device to a pulser and external circuit for further quantification, silver paint was applied on the edge of the graphene piece. Silver paint was allowed to air-dry, and resistance across the graphene piece was measured with a multimeter (VC97+, AideTek) to ensure the conductivity. Finally, a clean plastic tube (cut from 1.6 ml Eppendorf tube, inner diameter was ∼9 mm) was glued with Cytoseal (8310-16, Richard-Allan), so that it can hold medium for cell culture. Then the sample was air-dried, then sterilized under UV lamp for $>$ 30 minutes.

Cell culture on a graphene surface

A549 and PtK2 cells were cultured following standard protocol. In brief, A549 cells were cultured in Dulbecco's Modified Eagle's Medium (DMEM) with GlutaMAX-I (10566-016, Gibco) supplemented with 10% fetal bovine serum (FBS). Cells were kept in a T25 flask, at 37 °C in 5% CO2 humidified incubator and passaged 2∼3 times in a week. Similarly, PtK2 cells were kept in DMEM with GlutaMAX-I and 10% FBS and passaged ∼2 times a week. 16 hours before electroporation, cells were detached with trypsin (12065-010, Gibco) and harvested. For A549 cells, 75k cells were plated on the graphene device. This gives 90∼95% confluency after 16∼24 h. For PtK2 cells, ∼50k cells were plated 16∼24 hour ahead of the electroporation.

Assembly of an electroporation vessel

A copper wire was laid on silver paint, gently fixed by small pieces of tapes. A drop of silver paint was added on the copper wire to connect the graphene and the copper wire, and dried. The copper wires were later used to connect the device to a sourcemeter or a pulser. An electrode was assembled from a small metal stub. A copper wire was wrapped around the metal stub for a few times and fixed with scotch tape. Connectivity between the metal stub and the copper wire was ensured with a multimeter. A Teflon tape was used to cover the edge of the metal stub, to give a space between the metal surface and the graphene. The thickness of the Teflon tape was ∼400 μm.

Before delivering dyes, the resistance across the graphene was measured. Copper wires on the device were hooked up with an oscilloscope clip and plugged into a Keithley 2400 sourcemeter. The source voltage was set to be 10 mV and linearly swept, and corresponding current was recorded. The resistance was calculated from the slope of the I-V curve.

Once the conductivity was confirmed from the I-V curve, the copper wires were plugged into a pulser (Z375969, BRL Life Technologies). Cell culture medium was gently replaced with electroporation buffer (1652676, Bio-Rad) containing fluorescent probes. ∼150 μl of the buffer was used in each run. The electrode was gently submerged in a chamber and positioned properly. The copper wire on the electrode was connected to the pulser as well. To electroporate the cells, the pulser capacitor was set to 10 μF and charged until it reached ∼15 V and triggered.

Fluorescent probes

Phalloidin-Alexa fluor 647 (A22287, Invitrogen) was diluted in the electroporation buffer at ∼1/50 (final concentration ∼2 μM). Phalloidin-Alexa fluor 488 (A12379, Invitrogen) was diluted in the same buffer at 1/100∼1/200. Similarly, phalloidin-CF568 (00044-F, Biotium) was diluted in the buffer at ∼1/100. Lifeact-Cy5 was custom-ordered from Sigma-Aldrich. For electroporation, it was diluted in the electroporation buffer to ∼42 mM. Vimentin-AF647 (9856S, Cell signaling technology) was diluted at 1/50∼1/100. All dye dilutions were freshly prepared before electroporation and kept dark at room temperature.

Microscopy setups

Fluorescence imaging was performed on a conventional Olympus IX73 inverted wide-field epifluorescence microscope that was equipped with a standard lamp for fluorescence microscopy (U-HGLGPS). Three different filter cubes were used for deep red, orange, and green fluorescent channel, respectively. For deep red dyes such as Alexa fluor 647 or Cy5, the filter cube was configured with 60-nm band pass filter as excitation filter (ET620/60x), a dichroic mirror (zt647rdc-UF1), and an emission filter (ET700/75m). For orange dyes such as CF568, filter cube was equipped with a 25-nm band pass filter (ET545/25x) as an excitation filter, a dichroic mirror (zt561rdc-UF1), and an emission filter (ET605/70nm). For the green channel, filter cube was configured with a 40-nm band pass filter (ET470/40) as an excitation filter, a dichroic mirror (T495LPXR), and an emission filter (ET525/50m). Interference reflection microscopy (IRM) was performed on a same setup with a different filter cube, as previously described.1 Fluorescent and IRM images were obtained with either Olympus UplanSapo 60x water-immersion objective lens (NA 1.2), or UplanSapo 20x objective lens. Images were recorded with Andor Zyla 4.2 sCMOS camera at 2048 x 2048 pixels with ∼100 ms integration time. The effective pixel size was 65 nm for 60x, and 195 nm for 20x lens.

Live-cell STORM imaging was performed on a homebuilt setup based on a Nikon Eclipse Ti-E inverted optical microscope with a Nikon CFI Plan Apochromat λ x 100 objective lens (NA 1.45, oil) as previously described[6]. A 647-nm laser (MPB Communications) and 405-nm laser (Coherent) were coupled into an optical fiber and introduced into the sample through the back focal plane of the microscope. A translational stage was added to shift a laser beam towards to the edge of the objective to achieve a TIRF illumination. Continuous illumination of 647-nm laser (∼2 kW) was used to excite fluorophores and make them switch on and off. 405-nm laser was used to assist photoswitching. For 3D STORM, a cylindrical lens was added to the optical path. Emission was filtered with a dichroic mirror (Di01-R405/488/561/635) and a notched filter (ZET405/488/561/640). Data was recorded with an EM-CCD camera (iXon Ultra 897, Andor) at ∼9 ms integration time for 50000∼100000 frames, depending on the targets. The effective pixel size was ∼160 nm with this configuration.

Cell permeability test for fluorophores

A549 and Ptk2 cells were plated and grown on an 8 well chamber (LabTek) for 16∼24 hr. Organic dye dilution was prepared in electroporation buffer, at concentration that is comparable to the electroporation experiments. Culture medium was aspired and replaced with the organic dye dilution. Cells were allowed to uptake dyes for ∼30 min at room temperature (A549) or 37 °C (PtK2). After 30 minute, the dye solution was rinsed with warm Leibovitz's medium (L-15, 11415064, Gibco), and cells were imaged under fluorescence and bright field channel.

Live cell STORM imaging

Live cell STORM imaging was performed on the setup previously described. After electroporation, electroporation buffer was replaced with live cell STORM buffer (L-15 + 2% glucose + 5 mM MEA + 1% gloxy). Samples were imaged at room temperature, ambient condition.

Patterned electroporation

A CVD graphene was transferred to a pre-cleaned glass coverslip as previously described. Silver paint was applied on the edge of the graphene for resistance measurement. The resistance was measured across the graphene. A scratch was made at the center of graphene, with a P20 micropipette tips. Resistance measurement was performed again to see if the graphene was scratched as intended. After scratched, the resistance soared to a few mega Ω. The device was assembled, cells were cultured overnight, and copper wire was connected as previously mentioned. To deliver fluorescent probes specifically to one side, only one copper wire on the device was connected to the pulser. Then the first probe was added into the well, and delivered by an electrical pulse. The remaining probes in the solution was rinsed with pre-warmed L-15, and the second dye solution was added. The second pulse was applied on the other side without or after recovery. To achieve good selectivity, recovery between two pulses were required. Recovery media was prepared by adding 2% glucose (w/v) and 2 mM ATP (BSA04, Cytoskeleton) to culture medium. Cells were allowed to reseal their membrane in the recovery buffer at 37°C for 20∼30 min.

Chapter 8

Direct optical visualization of graphene and its nanoscale defects on transparent substrates

The work in this chapter was conducted in collaboration with Wan Li, Michal Wojcik, and Ke Xu. It is reproduced in part here from ref[5] and with permission from all coauthors.

8.1 Introduction

As discussed in the previous chapters, the unique properties of graphene could be used in optical microscopy in multiple ways. Being nearly unseeable, this thin layer above or underneath the sample provides the superior conductivity to the samples, but does not interfere with optical microscopy measurement. Therefore, it is not surprising that optical visualization of graphene is challenging up to date. With 2.3% absorption, very low optical contrast is achieved for graphene.

For this reason, the optical inspection of graphene was performed on specialized substrates like oxide-capped silicon substrates[48,219]. The ∼10% optical contrast of graphene on such substrates, together with the high-throughput and non-invasive features of optical microscopy, have greatly facilitated graphene research for the past decade[47,219,220]. However, transparent and flexible electronics, which currently stand as key commercial applications of graphene[49–52], are incompatible with these substrates. Direct optical visualization of graphene on transparent substrates remains a challenge[53–59,221]: limited contrast is achieved and local number of graphene layers is difficult to quantify, even with sophisticated setups. Visualization of nanoscale defects in graphene, e.g., voids, cracks, wrinkles, and multilayers, formed during either growth or subsequent transfer and fabrication steps, represents yet another level of challenge for most device substrates. Scanning electron microscopy (SEM), atomic force microscopy (AFM), and Raman spectroscopy are low in throughput,

prone to sample damage, and impose stringent requirements on substrate properties[57,58]. Fluorescence quenching microscopy[57,58,222–224] provides a powerful optical means to visualize graphene, but a fluorescent coating is required, and nanoscale defects are still difficult to detect. With interference reflection microscopy (IRM), we here report experimental optical contrast of up to 42% for monolayer graphene on transparent substrates, and further achieve outstanding sensitivity for nanoscale defects, thus enabling direct, high-throughput inspection at 4x video-rate.

8.2 Result and Discussion

IRM is a facile, label-free optical microscopy method originated in cell biology[225–227]. A collimated beam of filtered lamp light passes through the substrate and is reflected off interfaces between the substrate, culture medium, and cell membrane: the resultant reflection interference provides outstanding contrast for cell adhesion sites (SI in ref[5]). While offering a unique means to study nanoscale cell-substrate interactions, quantitative interpretation of results has been difficult due to complex cell geometries[225–227].

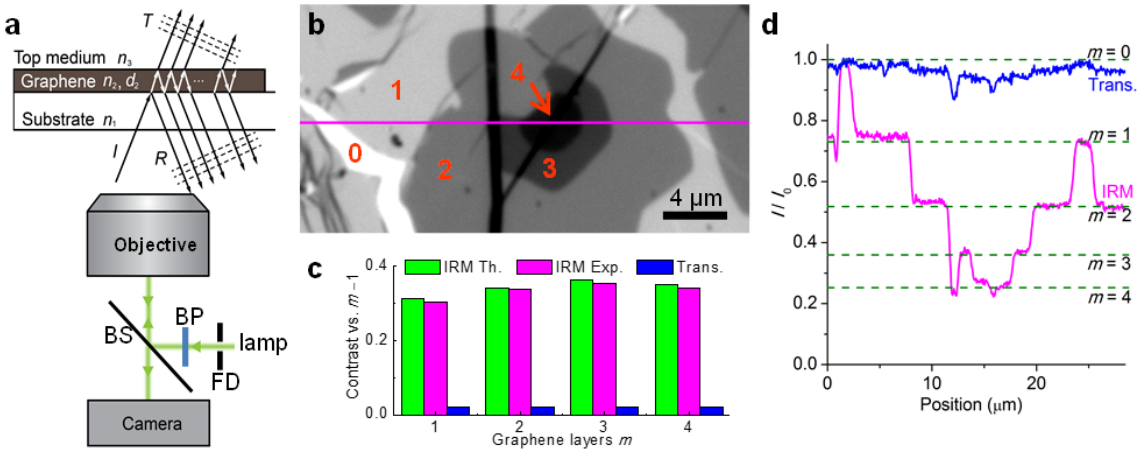

Figure 37: IRM visualization of graphene. (a) Schematic of setup. FD: field diaphragm; BP: band-pass filter; BS: beam splitter. (b) IRM image of graphene multilayers on a glass substrate. Red numbers indicate local layer numbers. (c) The theoretical (green) and experimental (magenta) IRM signal contrast on glass for m-layer graphene vs. (m-1)-layer graphene, in comparison to that of transmission light microscopy (blue). (d) Intensity profile along line in (c) (magenta), in comparison with the theoretically predicted IRM intensity (dotted lines) and experimental result from transmission microscopy (blue).

8.2.1 Interference reflection microscopy (IRM) visualizes multilayered graphene with excellent contrast

By repurposing IRM for imaging graphene, we experimentally achieved excellent contrast for graphene of different layers and provided quantitative explanation to our results. A standard

inverted fluorescence microscope with oil- and water- immersion objective lenses was configured with a 50/50 beam splitter and a 532/10 nm bandpass filter (Figure 37a). The field diaphragm was closed down to slightly smaller than the recording frame size to reject stray light[225–227]. We first examined copper-grown graphene[184] that was wet-transferred[184,228] onto glass, with water being the top medium (Figure 37b). Highly uniform IRM signal was observed for areas of the same number of graphene layers (m), while excellent contrast were observed for m = 0-4 (Figure 37cd). The signal contrast of each added layer, as defined by $C_m = (I_{m-1} - I_m)/[(I_{m-1} + I_m)/2]$, where I_m is IRM signal intensity on m-layer graphene (I_0 for no graphene coverage), was 30%, 33%, 35%, and 34%, respectively, for m= 1 to 4 (Figure 37cd). These results are >10-fold higher than relying on light absorption (∼2%)[50,57,58,185], and even 3-fold higher than that is experimentally achieved on optimized SiO_2-capped-Si substrates (∼10%)[53,219,220]. The experimental signal-to-noise ratio for each additional layer of graphene, defined as $SNR_m = (I_{m-1} - I_m)/[(\sigma_{m-1} + \sigma_m)/2]$, where σ_m is the standard deviation of signal between pixels for the same m, is found to be 34, 32, 31, and 22 for m= 1 to 4, respectively. This result suggests our data should enable unambiguous identification of graphene layers down to subpixel levels. In comparison, conventional transmission light microscopy, performed on the same microscope using the same objective lens (thus the same magnification and numerical aperture) and with comparable light intensities at the same camera, achieved low contrast of ∼2% and SNR of 2-3 for each layer (Figure 37cd), thus illustrating the common difficulties in characterizing graphene on transparent substrates[53–59,221]. To understand the exceptional contrast we achieved, we adapted IRM theories[225–227] but further took into account the finite absorption of graphene and the interferences between infinite times of reflection at the substrate-graphene and graphene-medium interfaces (Figure 37a). Using transfer-matrix method we found (Methods) the intensity of reflected light (and thus IRM signal) to be:

$$I = |\frac{e^{i\varphi} r_{12} + e^{-i\varphi} r_{23}}{e^{i\varphi} + e^{-i\varphi} r_{12} r_{23}}|^2 I_I \tag{8.1}$$

where I_I is the intensity of incident light, $\varphi = 2\pi n_2 d_2/\lambda$ is the phase change across graphene, $r_{12} = (n_1 - n_2)/(n_1 + n_2)$, and $r_{23} = (n_2 - n_3)/(n_2 + n_3)$. Here n_1, n_2, and n_3 are the refractive indices of the substrate, graphene, and overlying medium, respectively. $d_2 = 0.335m$ nm is the thickness of graphene of m layers, and λ is wavelength of incident light. For $\lambda = 532$ nm, with glass ($n_1 = 1.52$) and water ($n_3 = 1.33$) being the substrate and the overlying medium, respectively, and using complex refractive index of graphene $n_2 = 2.65 - 1.27i$[219,229], we thus calculated the theoetical C_m to be 31%, 34%, 36%, and 35%, for $m = 1$ to 4, respectively, in good agreement with our experimental results (Figure 37cd). Eqn 8.1 further predicts that the achieved contrast is relatively insensitive to the wavelength, and we have experimentally achieved comparable contrast without using any optical filters (SI in ref[5]).

The outstanding contrast of IRM is powerful in revealing nanoscale structures and defects in graphene. Figure 38a shows result on a nano-patterned graphene monolayer on glass. Excellent contrast and resolution were observed. Intensity profiles yielded ∼ 300 nm fea-

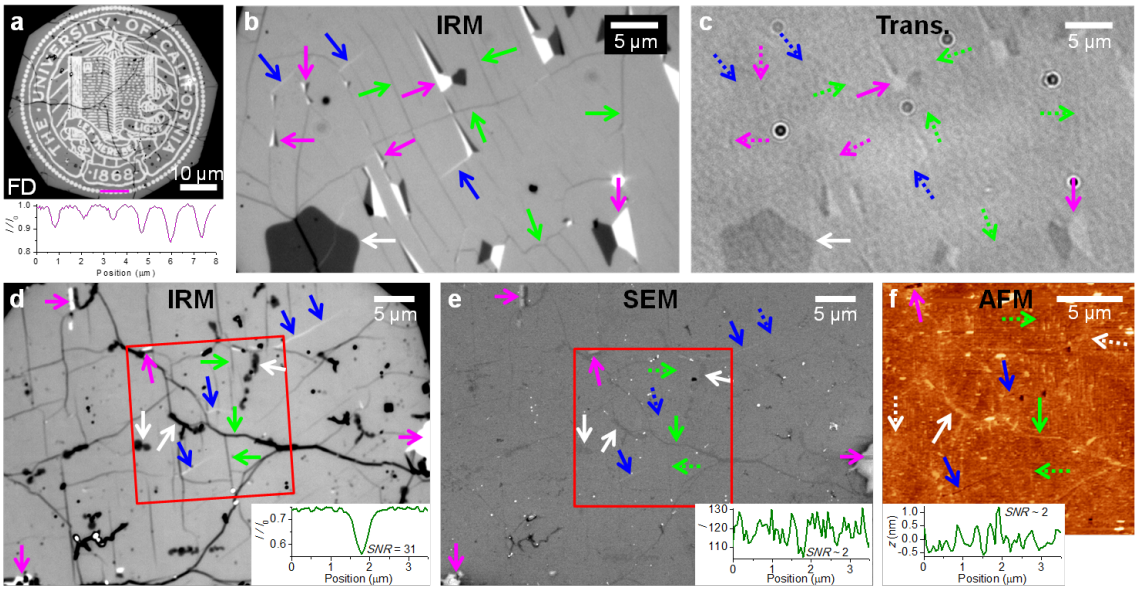

Figure 38: IRM visualization of nanoscale structures in graphene. (a) IRM of a nano-patterned graphene monolayer on glass (top), and intensity profile along the magenta line (bottom). FD: field diaphragm. (b) IRM of a predominantly monolayer graphene sample that was subjected to mechanical disruptions. (c) Transmitted microscopy of the same area. (d-f) IRM result (d) cross-examined with SEM (e) and AFM (f). AFM image corresponds to red boxes in (d,e). Insets: intensity and height profiles across the same major wrinkle that is observed in all imaging modes (vertical green arrows). Arrows: white: bilayers; magenta: tears and fold-overs; blue: cracks; green: wrinkles. Dashed arrows indicate features that are not visible in a particular imaging mode.

ture widths for the finer structures, indicating that the resolution approached the diffraction limit. Figure 38b shows a predominantly monolayer sample that was subjected to mechanical disruptions that would possibly be encountered in device fabrication. Rich features[50,184,230] are clearly revealed, e.g., local bilayers (white arrow), tears and fold-overs (magenta arrows), and nanoscale cracks (blue arrows) and wrinkles (green arrows). In comparison, in conventional transmission light microscopy (Figure 38c) the smaller tears are overwhelmed by noise (dashed magenta arrows) and none of the nanoscale cracks or wrinkles are discernable (dashed blue and green arrows).

8.2.2 IRM outperforms SEM and AFM in revealing nanoscale features on graphene

We next cross-examined IRM with SEM and AFM (Figure 38d-f). As the glass substrate is insulating and unsuitable for SEM, we relied on the conductivity of graphene itself[6]. The SEM images (Figs. 2e, S3, S4) are in agreement with IRM results, but afford significantly lower contrast and SNR. Whereas bilayers and the more prominent wrinkles and cracks are visible (solid arrows), the thinner wrinkles and cracks, which are clearly resolved in IRM, are

hardly observable in SEM (dashed green and blue arrows). Intensity profiles indicate that the more prominent wrinkles visualized by SEM achieve SNR ~ 2 (Figure 38e inset and SI in ref[5]): the same wrinkles achieve SNR >30 in IRM (Figure 38d inset and SI in ref[5]).

AFM also yielded structural information consistent with IRM but at much reduced contrast (Figure 38f and SI in ref[5]). Due to the relatively rough surface of glass (RMS roughness ~ 0.5 nm), features $<\sim 1$ nm in height were difficult to identify. Consequently, bilayers are barely visible (white arrows), and for wrinkles, only the most prominent ones ($>\sim 1.0$ nm in height) are discernable (green arrows). SNR $<\sim 2$ was observed for the same wrinkles that achieve SNR >30 in IRM (Figure 38df insets and SI in ref[5]).

In addition to structures and defects in graphene, we note that IRM also provides excellent visualization of nanoscale contaminants, including speckle-like debris and thread-like polymer residuals that match well with SEM and AFM results (Figure 38d-f and SI in ref[5]).

We emphasize that besides outstanding contrast, IRM is further characterized by exceptional throughput, low invasiveness, and ease of operation. Wide-field images were captured in snapshots in ∼10 ms, only limited by the camera framerate. This is ∼1,000-times and <10,000-times faster than SEM and AFM, respectively. Moreover, IRM does not require vacuum, and avoids possible sample damage due to a scanning tip or electron beam (Figure 39kl below). Real-time inspection of nanoscale defects is thus readily achieved over large areas at up to 4x video-rate (Videos S1 and S2).

8.2.3 Characterization of graphene on various transparent substrates

We next examined graphene on other transparent substrates (Figure 39). Excellent IRM contrast of 42% and 39% (Figure 39abh) is respectively observed for monolayers on quartz and CaF_2 substrates, which for their superior optical properties have been often employed for graphene physics and device applications[49,50,231–234]. For flexible substrates, we achieved contrast of 23%-37% for monolayer graphene on five common polymer films, namely polychlorotrifluoroethene (Aclar), polycarbonate (PC), polyethylene terephthalate (PET), cellulose acetate (CA), and polyvinyl chloride (PVC) (Figure 39c-h). Nanoscale graphene structures/defects of different types were clearly visualized on all substrates. We note that except Aclar, in our hands the other polymer films were noticeably attacked by solvents used to dissolve the PMMA protection layer in graphene wet-transfer. For the heat-stable PC substrate, we thus instead transferred graphene using thermal release tapes[50]. Although a high yield was achieved, microscopic cracks were often found in the transferred graphene (Figure 39d). Transfer using Scotch tape led to very low yield and larger cracks (Figure 39e for PET). Wet transfer without PMMA protection led to low yields and frequent cracks (Figure 39fg for CA and PVC). By consistently achieving high contrast, IRM thus provides a way to directly characterize and compare defect levels as graphene is transferred to different potential device substrates via different procedures.

We note that these characterizations are difficult to achieve with alternative techniques.

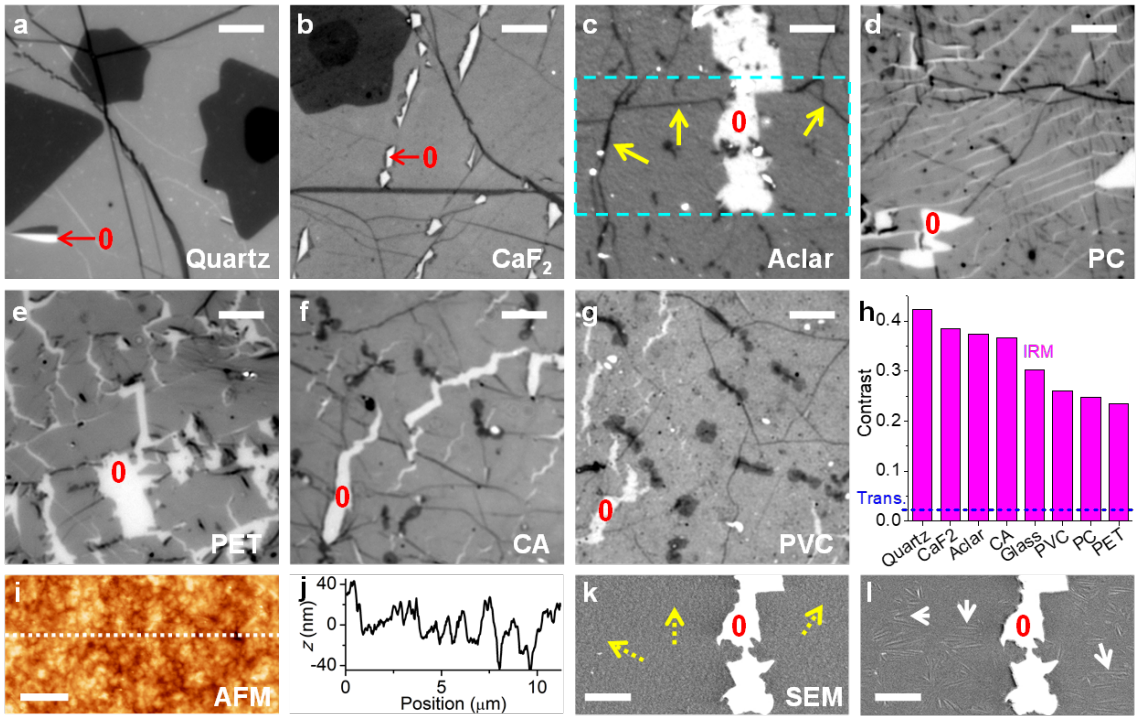

Figure 39: IRM visualization of graphene on different transparent substrates. (a) Quartz. (b) Calcium fluoride. (c) Aclar (polychlorotrifluoroethene). (d) Polycarbonate. (e) Polyethylene terephthalate. (f) Cellulose acetate. (g) Polyvinyl chloride. (h) Measured IRM contrast for monolayer graphene on different substrates (magenta). Blue line: contrast of transmission microscopy. (i) AFM image of graphene on Aclar [same sample as (c)]. (j) Height profile along the dotted line. (k) SEM image of the same sample [cyan box in (c)]. Dotted arrows point to where wrinkles are visualized in IRM (c). (l) A subsequent SEM image: arrowheads point to structural changes. Scale bars: 5 μm (a-g, k, l); 2 μm (i). "0" marks areas with no graphene coverage.

Due to the very large surface roughness of commercial-grade polymer films (>10 nm), AFM often does not provide useful contrast (Figure 39ij). Meanwhile, SEM provides poor contrast and causes major structural changes of the sample (Figure 39kl and SI in ref[5]) due to electron beam. IRM thus uniquely provides nanoscale structural details for graphene on these substrates.

8.2.4 *In situ* monitoring of crack propagation upon tensile stress

As a key demonstration of the enabling power of our technique, we next report in situ monitoring of the microscopic failure mode of graphene under strain, an important performance parameter for flexible electronics. Monolayer graphene on Aclar films was subjected to uniaxial stretching, during which process concurrent IRM and electrical characterizations were performed (Figure 40 and Video S3). IRM captured the very onset of graphene failure at $\sim$ 0.9% strain, where the observed emergence of nano-cracks (Figure 40f and Video S3)

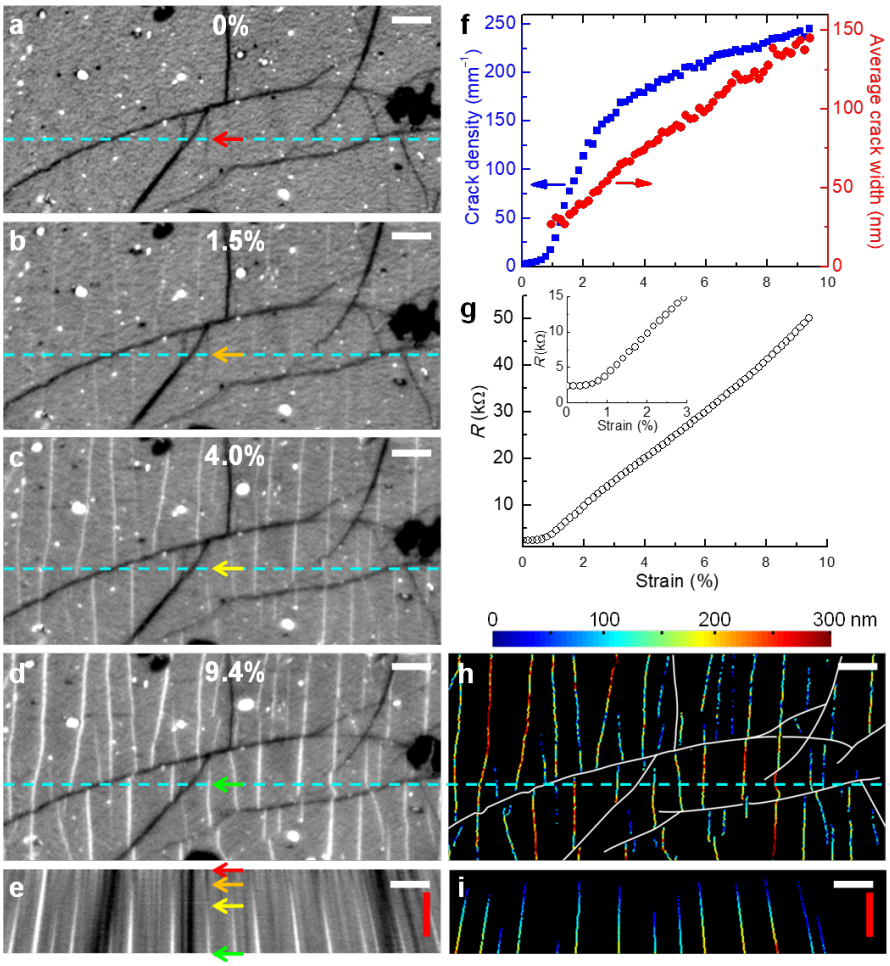

Figure 40: *In situ* monitoring of the microscopic failure mode of graphene under uniaxial strain. (a-d) Four representative IRM frames recorded during stretching. Strain amount (in horizontal direction) is labeled in each image. (e) Kymograph along the cyan lines in (a-d), constructed by extracting pixels along this particular line from every IRM frame and lining them up in the vertical direction. Red, orange, yellow, and green arrows correspond to data in (a-d), respectively, and point to a wrinkle that evolves into a crack during stretching. (f) Strain-dependent crack density and average crack width, determined from IRM images. (g) Concurrently measured graphene resistance. Insets: zoom-in at low strain. (h) Computer-tracked nano-cracks in (d) with local width coded by color. Major wrinkles are drawn as white lines. (i) Kymograph of tracked cracks. Horizontal scale bars: 5 μm. Vertical scale bars (red): 5% strain.

coincided with a sudden rise in electrical resistance (Figure 40g and inset). Previous bulk Raman spectroscopy studies on monolayer graphene and carbon fibers indicate mechanical failure at similar strain levels ($\sim$1.0%)[235,236], although electrical measurements on multilayer devices have reported little resistance change up to 6% strain[49,50]. Crack propagation ensued upon further stretching, and numerous nano-cracks became readily visible in IRM at $\sim$1.5% strain (Figure 40b and Video S3). The rapid increase in crack density slowed down at $\sim$4% strain, where nano-cracks distributed roughly evenly across graphene at a density

of ∼180 mm^{-1} (Figure 40c). Crack widening persisted throughout stretching (Figure 40efi); the measured average crack width, as determined from the integrated light intensity of the diffraction-limited IRM images, increased from the initial ∼25 nm to ∼140 nm at 9.4% strain (Figure 40f). Resistance increased monotonically as cracks developed and widened (Figure 40g). These observations bear general similarities to that reported for thin metal oxide films under strain[237,238]. However, for graphene the traditional SEM approaches are unsuitable (Figure 39kl).

8.3 Conclusion

In this chapter, we directly visualized and examined graphene on transparent substrates. We utilized IRM, a label-free interference microscopy method, to characterize the graphene and its defect with high contrast. We achieved 10-fold increase in the optical contrast, from 2∼3% optical contrast of a conventional transmission microscopy. Cross-examination with other microscopy technique, AFM and SEM, also confirms that IRM enabled high-contrast visualization of nanoscale defects on graphene. This approach is particularly useful with plastic polymer substrate with high surface roughness (>few nm): AFM or SEM fails to pick up the defects on graphene. IRM enables high-contrast, high-throughput characterization of graphene, and opens the door to other exciting applications.

8.4 Materials and Method

IRM Theory

Our derivations and notations follow conventions of thin-film optics[239]. Layer configuration of the system is given in Figure 37a. Incident light of wavelength λ and intensity I_I enters the sample from the substrate side, successively encounters graphene and top medium, and leaves as reflected (R) and transmitted (T) light. The refractive indices of the substrate, graphene, and top medium are respectively denoted as n_1, n_2, and n_3. Graphene thickness is d_2.

The Fresnel coefficients at the substrate-graphene and graphene-top medium interfaces are respectively $r_{12} = \frac{n_1-n_2}{n_1+n_2}$, $t_{12} = \frac{2n_1}{n_1+n_2}$ and $r_{23} = \frac{n_2+n_3}{n_2+n_3}$, $t_{23} = \frac{2n_2}{n_2+n+3}$. The transfer matrices at the two interfaces are $T^{12} = \frac{1}{t_{12}} \begin{bmatrix} 1 & r_{12} \\ r_{12} & 1 \end{bmatrix}$ and $T^{23} = \frac{1}{t_{23}} \begin{bmatrix} 1 & r_{23} \\ r_{23} & 1 \end{bmatrix}$. The transfer matrix in graphene is $T^2 = \begin{bmatrix} e^{i\varphi} & 0 \\ 0 & e^{-i\varphi} \end{bmatrix}$, where $\varphi = \frac{2\pi}{\lambda} n_2 d_2$. The transfer matrix for the system is:

$$T^{13} = T^{12}T^{2}T^{23}$$

$$= \frac{1}{t_{12}}\begin{bmatrix} 1 & r_{12} \\ r_{12} & 1 \end{bmatrix}\begin{bmatrix} e^{i\varphi} & 0 \\ 0 & e^{-i\varphi} \end{bmatrix}\frac{1}{t_{23}}\begin{bmatrix} 1 & r_{23} \\ r_{23} & 1 \end{bmatrix}$$

$$= \frac{1}{t_{12}t_{23}}\begin{bmatrix} e^{i\varphi} + e^{-i\varphi}r_{12}r_{23} & e^{-i\varphi}r_{12} + e^{i\varphi}r_{23} \\ e^{i\varphi}r_{12} + e^{-i\varphi}r_{2}3 & e^{-i\varphi} + e^{i\varphi}r_{12}r_{23} \end{bmatrix}$$

The reflection coefficient is:

$$r = \frac{T_{21}^{13}}{T_{11}^{13}} = \frac{e^{i\varphi}r_{12} + e^{-i\varphi}r_{23}}{e^{i\varphi} + e^{-i\varphi}r_{12}r_{23}}$$

Intensity of reflected light, which is recorded experimentally in IRM images, is thus:

$$I = |r|^2 I_I = |\frac{e^{i\varphi}r_{12} + e^{-i\varphi}r_{23}}{e^{i\varphi} + e^{-i\varphi}r_{12}r_{23}}|^2 I_I$$

Meanwhile, intensity without graphene (a direct n_1-n_3 interface) is: $I_0 = |\frac{n_1 - n_2}{n_1 + n_3}|^2 I_I$. It can be shown that this result is equal to that obtained through Eqn 8.1 for $d_2 = 0$ (number of graphene layer, $m = 0$).

Preparation of graphene on different substrates

Wet transfer with PMMA protection Graphene on glass, quartz, CaF_2 and Aclar (polychlorotrifluoroethene) substrates were prepared through the standard wet-transfer method with PMMA protection[184,228]. CVD graphene on copper foils (Graphene Supermarket, Calverton, NY) was spin-coated with a ∼150 nm layer of polymethyl methacrylate (PMMA 495 A4, MicroChem, Newton, MA). After the copper was removed in an etching solution (5% HCl + 20% $FeCl_3$), the graphene-PMMA stack was transferred to a fresh water bath so it floated on the water surface. Water bath transfer was repeated three times to remove traces of ferric chloride. The PMMA-protected graphene film was then transferred to the target substrates. PMMA was removed in two steps using anisole (15 min) and acetone (1-2 hours) followed by a rinse in isopropanol (10 min), and the sample was dried with nitrogen gas.

Wet transfer without PMMA protection CVD graphene on copper was floated on top of an etching solution for 5-10 minutes to remove copper. As soon as the copper layer became invisible, a cleaned polymer substrate was used to carefully stamp the graphene piece from the top. The polymer substrate with graphene was air-dried for ∼20 minutes and then rinsed with DI water.

Dry transfer using thermal release tape Graphene transfer tape (Graphene Supermarket, GTT-5pk) was applied to a piece of CVD graphene on copper and pressed thoroughly. Copper was removed in an etching solution for ∼10 minutes. Tape with graphene was rinsed in fresh DI water for three times and then briefly air-dried. The tape was applied to the polymer substrate, pressed and scraped thoroughly. A hotplate was used to heat the sample to ∼90 °C for release of the tape.

Dry transfer with 3M scotch tape 3M Scotch 105 Magic Tape was applied to a piece of CVD graphene on copper and pressed and scraped thoroughly. Copper was removed in an etching solution for ∼10 minutes. Sample was rinsed with fresh DI water for three times. After brief air-drying, the tape with graphene was applied on a cleaned polymer substrate, pressed and scraped thoroughly. The tape was gently taken off from the polymer substrate.

Nano-patterning of graphene

Defined nano-patterns of graphene (Figure 38a) were fabricated using focused ion beam (FIB). A gallium ion beam in a FEI Quanta SEM/FIB system was used to pattern CVD graphene on a copper foil, and the patterned graphene was transferred to a glass substrate using PMMA-protected wet transfer as described above. Mechanically disrupted graphene samples (e.g., Figure 38bc) were produced by immersing the samples in acetone and using a pipette to generate air bubbles at the graphene surface, a process that emulates what is often encountered in the lift-off process of photolithography for device nanofabrication.

Interference reflection microscopy (IRM)

IRM was performed on a conventional Olympus IX73 inverted wide-field epifluorescence microscope that was equipped with a standard lamp for fluorescence microscopy (U-HGLGPS). The fluorescence filter cube was configured with a 50/50 beam splitter (Chroma 21000) and a 530/10 nm band pass filter (Chroma D532/10x) as the excitation filter. While the use of a band pass filter facilitated comparison of results with theory, the obtained contrast was relatively insensitive to the wavelength, and comparable contrast may be obtained without using an optical filter (SI in ref[5]). No emission filter was used. Objective lenses were an Olympus UplanFl 100x oil-immersion objective (NA ∼0.9 with iris diaphragm) and an Olympus UplanSapo 60x water-immersion objective (NA 1.2). Significantly reduced contrast was observed when dry objective lens was employed due to back-reflections at air-glass interfaces (∼8% for monolayer graphene on glass when using an UplanSapo 20x objective), and so is not recommended. IRM images were acquired at 16-bit bit-depth using an Andor Zyla 4.2 sCMOS camera at 1024x1024 pixels with ∼20 ms integration time (∼50 frames per second) or at 512x512 pixels to achieve a 10 ms integration time (100 frames per second or 4x video-rate). Effective pixel size, l_{pixel}, was 65 nm and 108 nm when using the 100x and 60x objectives, respectively. The microscope field diaphragm was closed down to slightly smaller than the 1024x1024 frame size to reject stray light from oblique angles, hence the black edges

in images. Comparable results were obtained when the entire sample was immersed in water, or when a droplet of water was deposited at the area of observation. Eqn 8.1 predicts that the final results only depend on the index of refraction, rather than the nature, of the top medium. In this work we focused on water as it is most accessible and uniquely compatible with all the substrates used in this study.

SEM and AFM characterization

The conductivity of graphene itself was utilized to enable SEM characterization of graphene on the insulating substrates[6]. The sample was mounted on a standard metallic sample mount using carbon tape, and a small amount of silver colloid paint (Ted Pella 16031) was used to create a conductive bridge between graphene and the sample mount. SEM imaging was performed on a FEI Quanta 3D FEG system in secondary-electron mode. Comparison of images obtained at different acceleration voltages indicated that best contrast was obtained at 2 kV (SI in ref[5]), which was selected for comparison with IRM results. AFM images were taken on an Asylum MFP-3D system in tapping mode using aluminum-coated probes (Tap150Al-G; BudgetSensors). Nominal values of the force constant, resonance frequency, and tip radius were 5 N/m, 150 kHz, and <10 nm, respectively. AFM data were processed using WsXM[240].

Concurrent IRM and electrical characterization of graphene subject to uniaxial stretching

Sample preparation For stretching experiments, CVD graphene (∼10x4 mm) was deposited at the center of a ∼60x6 mm strip of a 0.2 mm-thick Aclar 33C film (Ted Pella, Redding, CA). A liquid metal, GaInSn (68.5%:21.5%:10%), was employed as contact electrodes to ensure reliable contact to graphene during stretching (Scheme S1 inset). Two thin copper wires were first connected to graphene using silver paint and glued down onto the substrate with epoxy. GaInSn liquid metal was then applied to connect the graphene surface with the copper wires; final distance between electrodes was ∼8 mm. The liquid metal wetted the graphene surface well and so maintained highly stable junction conductance during stretching. A control sample in which GaInSn liquid metal directly bridged two copper wires on the Aclar substrate showed a highly stable resistance of 1.36-1.38 Ω during a similar stretching process, which is more than three orders of magnitude smaller than the measured resistance of graphene.

Measurement system The measurement system (Figure 41) was comprised of three sub units, namely a home-built tensile-testing station to apply uniaxial strain, IRM to monitor *in situ* structural changes in graphene under strain, and a Keithley 2400 SourceMeter to concurrently monitor the electrical properties of graphene.

The tensile-testing station was constructed by mounting two single-axis motorized translation stages (PT1-Z8, Thorlabs) onto the central plate of the microscope stage, face to face

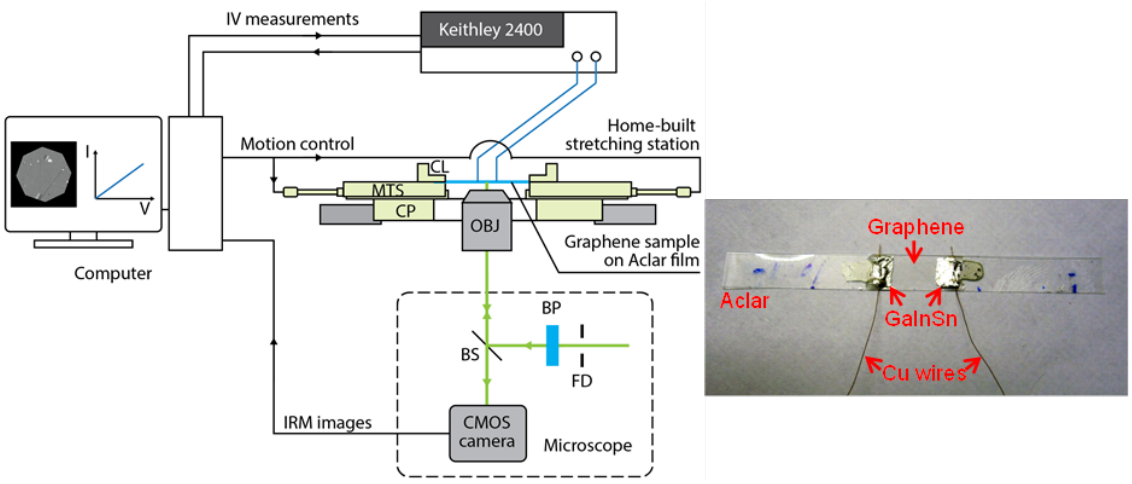

Figure 41: Experimental setup for concurrent IRM and electrical characterization of graphene under stretching. CP: Central plate of the microscope. MTS: motorized translation stage. CL: clamp. Inset: photo of the sample. A GaInSn liquid metal was employed to achieve reliable contact to graphene during stretching.

with a 50 mm gap at zero displacement. The strip-shaped sample was clamped at the two ends to the two stages so that its long axis is aligned with the translational axes of both stages. A computer program was developed to simultaneously displace the two motorized stages to opposite directions at the same rate. The system is effective for stretching graphene up to a strain of ∼9.5 %, when the Aclar film starts to yield. Strain was measured by examining the actual displacements of structural features within the sample from the obtained IRM images.

IRM system was as described above, but with the addition of an extension tube for the objective lens to account for the increase in height due to the stretching stages. To calculate the width of nano-cracks in monolayer graphene, which are often smaller than the diffraction-limited resolution of optical microscopy (∼300 nm), we integrated by pixel, across the crack, the intensity difference when compared to continuous graphene, $\Sigma\Delta I_{crack}$. The crack width was then determined by $w = l_{pixel}\Sigma\Delta I_{crack}/(I_0 - I_1)$. Here l_{pixel} is the effective pixel size, and I_0 and I_1 are the experimentally measured light intensity per pixel on blank substrate and on continuous monolayer graphene, respectively. Crack density is calculated as the number of nano-cracks per unit length in the stretching direction, averaged across the image.

A Keithley 2400 SourceMeter was used to monitor the electrical properties of graphene during stretching. Current through graphene was recorded as the voltage was continuously swept in loops between -12 mV and 12 mV. Resistance was determined by fitting to the resultant, highly linear I-V data.

Chapter 9

Conclusion and outlook

The projects presented in this thesis is under a unified theme: how to maximize the power of optical microscopy in terms of the performance (spatial resolution and contrast) and the dimensionality of the data we acquire. As concluding remarks, I would like to briefly introduce noteworthy ongoing efforts in these directions.

Multidimensional approaches in super-resolution microscopy

Combination of single-molecule localization with other measurement provides the ultimate sensitivity at a molecule level and superior spatial resolution. In this thesis, I focused on the spectral measurement and discussed the strategies to encode and decode micro-environments of the system via single-molecule fluorescent spectrum. Recent studies in single-molecule measurement further utilize other dimensional information, and use a variety of optical approaches to encode/decode the micro-environment or the parameter of interest[241,242]. For example, our lab showed that the diffusivity of a freely diffusing fluorescent protein in a cell could be mapped thorugh a stroboscopic approach[242]. Pulsed illumination was employed to minimize motion-blur of a fluorescent protein as well as to measure nano-scale displacement between the consecutive frames[242]. As an approach to retrieve more information from the temporal domain, the binding kinetics of bio-molecules was quantitatively measured by manipulating with the temporal domain[241]. The temporal dynamics is encoded into a point spread function (PSF) through a rotating phase mask in the Fourier plane, and retrieved by fitting PSF orientation in the processing step[241].

Alternatively, a parameter of interest can be encoded/decoded in a ratiometric manner[26,27,29–31,243,244]. This has been extensively used for multi-color imaging to classify a few different fluorescent dyes/proteins[29–31], but this does not have to be limited for this purpose. For instance, molecular orientation of a fluorescent protein was measured by comparing fluorescence signal along different polarization orientations[243–245]. To summarize, multi-dimensional single-molecule microscopy is a promising direction to probe local micro-environment in a heterogeneous systems, and this can be achieved through various optical strategies. I look forward to development of such strategies that will broaden the potential

of fluorescence microscopy.

New fluorescent probes

Since the advent of single-molecule localization microscopy, numerous fluorescent probes and strategies to achieve the optimal blinking/switching kinetics were reported[7–9,22–24,187,246–248]. Besides the brightness and blinking behavior, environment-sensing ability of a fluorescent probe could be characterized and optimized for multidimensional, functional super-resolution microscopy. Up to this point, the environment-sensing ability of fluorescent sensors is mostly characterized at bulk level[37–44,46], and they are utilized with a confocal microscopy in ratiometric manner[43,44,46]. Characterization and design of fluorescent sensors that work well for the single-molecule localization microscopy still remain largely unexplored, but such efforts would enable us to look at the heterogeneous system with multi-dimensional aspect.

At this point, we still have a plenty of room to improve and optimize both the optical and sensing performance, and to design and characterize a new probe for multidimensional super-resolution imaging. Indeed, my colleague and I found quite a few organic dyes suitable for STORM imaging, and some of them exhibited a mild spectral shift upon environment change such as a change in pH or solvent polarity. Molecular modification to improve their performance in STORM imaging as well as the sensitivity would be a good starting point. As part of such attempts, I have been collaborating with Dr. Andrey Klymchenko at CNRS on developing tailor-made fluorescent probes for live cell imaging. We modified a solvatochromic dye so that it exhibits good photostability, proper binding kinetics, high specificity for plasma membrane, and brightness while keeping their solvatochromic behavior. With those new probes, we were able to visualize rich features and lipid order of plasma membranes of live cells, which are not often visualized with typical, cell-permeable fluorescent probes.

Besides probes' spectral/optical properties, a mechanism to achieve molecular specificity of fluorescent probes is critical for the imaging experiments. In earlier days, the researchers relied on transient expression of the fluorescent proteins[8], antibodies[7,25], or partition property of the organic dyes[9,84,86]. Thanks to the recent advances in gene editing methods such as Crispr-Cas system[249,250], we now have better tools to tag a target of interest with a fluorescent probe in highly specific fashion[251,252]. Furthermore, use of smaller antibodies, such as single-domain antibody (or nanobody)[253–257] would reduce the bias in the target labelling, thus improve the spatial resolution. For organic dyes, the molecular specificity towards a target has been achieved in multiple manners. For example, some cell permeable dyes "click" to the target via unnatural amino acid or enzymatic reactions[258–261]. Such strategies would enable us to label and visualize target in live cells with the smaller fluorescent tags.

Computational microscopy

In single-molecule localization microscopy, the final image is reconstructed from a image stack (typically a few thousand to a few tens of thousand frames) by identifying and localizing the turned-on fluorescent probes[7,8]. For the best spatial resolution, precise modeling and fitting

of the diffraction-limited images of fluorescent molecule, PSF images, are critical. However, most researchers still rely on Gaussian-like function to approximate the PSFs and to achieve the subpixel resolution due to the simplictiy[262,263].

As we could afford more computational power nowadays, attempts to use more complicated and realistic PSF models have been made[131,133,264]. For example, arbitrary PSFs can be modeled as spline polynomials and fitted accordingly[131,133,264]. This would cost extra computational power and time[133], but offers a better performance in the spatial resolution[131]. This method provides a way to consider consider and calibrate instrument-specific abbreviation[131], which often deviate PSF images substantially from the ideal Gaussian-like shapes. Furthermore, advanced fitting/estimators open the possibility to model custom PSFs[133] through PSF engineering, such as double-helix models[126] or saddle-point model[265].

Besides the complex parametric models, machine learning and other data-driven approaches have been adapted in optical microscopy field[3,266–270]. Here we presented a multidimensional imaging application where neural networks, one of machine learning technique, extract the multiple parameters from the unmodified PSF images[3]. Machine learning-based approaches have been also applied to localization of molecules[268], reconstruction of high quality image from the sparse localization[266], and estimation of emission wavelength or axial position from PSF images[3,136,267]. The computational approaches give the researchers flexibility in designing experiment, in a sense that they often compensate the weakness of the experiment or the data acquired, thus improve the performance[271,272]. Working with single-molecule data gives immediate advantage and challenge: it is easy to accumulate enough amount of data in short time, but accessing their good "ground truth" could be challenging due to relatively low signal-to-noise ratio or stochastic nature. The latter could be tackled by novel approaches such as correlative measurement with other technique, experiment design that minimizes deviation, or realistic PSF modeling and simulations.

Optical microscopy for graphene and 2D materials

In chapter 8, we employed interference reflection microscopy (IRM) to examine graphene with high contrast and throughput. Owing to its good temporal resolution, we successfully tracked the crack propagation upon tensile stress in situ. In similar fashion, it is also possible to track the change in graphene with good temporal resolution, as long as it involves change in refractive index or thickness. My colleagues recently presented monitoring of reactions on graphene substrate *in situ*[273,274]. In these works, the change of graphene substrate upon chemical oxidation[273], or electrochemical oxidation/reduction[274] was monitored. Their finding highlights the reactions progress in spatially heterogeneous fashion[273,274]: the reaction initiates at/near defects and propagates in two dimensions. Although other alternatives, like micro-Raman spectroscopy are capable to reveal the reaction progress, they provide lower temporal resolution and reduced contrast. Furthermore, application of IRM could extend to other 2D materials and enable large-scale examination.

To conclude, optical microscopy is a solid tool in scientific research. Especially, single-molecule localization microscopy has been growing rapidly in the last decade, and numerous effort has been merged to this field. One of the exciting features of this topic is that people from diverse knowledge and background could bring their aspects and make contribution. It has embraced quite a few different disciplines, including cell biology, neuroscience, organic chemistry, optics, physics, mathematics, as well as computer science, and the interdisciplinary inputs enrich the field. During my PhD, I learned that a gorgeous microscopy image is built on numerous behind-the-scenes, from molecular biology, optics to computational processing. That said, we have quite a few different options/ways when improving the performance, usability, and potential of the microscopy. As a part of such effort, this dissertation covers the multiple strategies to improve the performance of optical microscopy from various aspects. Now I look forward to seeing new methods that maximize the potential of optical microscopy as well as applications in broad research fields.

Reference

[1] S. Moon, R. Yan, S. J. Kenny, Y. Shyu, L. Xiang, W. Li, and K. Xu. "Spectrally resolved, functional super-resolution microscopy reveals nanoscale compositional heterogeneity in live-cell membranes". *J. Am. Chem. Soc.* **139**, (2017), 10944.

[2] L. Xiang, M. Wojcik, S. J. Kenny, R. Yan, S. Moon, W. Li, and K. Xu. "Optical characterization of surface adlayers and their compositional demixing at the nanoscale". *Nat. Commun.* **9**, (2018), 1435.

[3] T. Kim, S. Moon, and K. Xu. "Information-rich localization microscopy through machine learning". *Nat. Commun.* **10**, (2019), 1996.

[4] R. Yan, S. Moon, S. J. Kenny, and K. Xu. "Spectrally Resolved and Functional Super-resolution Microscopy via Ultrahigh-Throughput Single-Molecule Spectroscopy". *Acc. Chem. Res.* **51**, (2018), 697–705.

[5] W. Li, S. Moon, M. Wojcik, and K. Xu. "Direct Optical Visualization of Graphene and Its Nanoscale Defects on Transparent Substrates". *Nano Lett.* **16**, (2016), 5027–5031.

[6] M. Wojcik, M. Hauser, W. Li, S. Moon, and K. Xu. "Graphene-enabled electron microscopy and correlated super-resolution microscopy of wet cells". *Nat. Commun.* **6**, (2015), 7384.

[7] M. J. Rust, M. Bates, and X. W. Zhuang. "Sub-diffraction-limit imaging by stochastic optical reconstruction microscopy (STORM)". *Nat. Methods* **3**, (2006), 793–795.

[8] E. Betzig, G. H. Patterson, R. Sougrat, O. W. Lindwasser, S. Olenych, J. S. Bonifacino, M. W. Davidson, J. Lippincott-Schwartz, and H. F. Hess. "Imaging intracellular fluorescent proteins at nanometer resolution". *Science* **313**, (2006), 1642–1645.

[9] A. Sharonov and R. M. Hochstrasser. "Wide-field subdiffraction imaging by accumulated binding of diffusing probes". *Proc. Natl Acad. Sci. USA* **103**, (2006), 18911.

[10] R. E. Thompson, D. R. Larson, and W. W. Webb. "Precise nanometer localization analysis for individual fluorescent probes". *Biophys. J.* **82**, (2002), 2775.

[11] A. Yildiz, J. N. Forkey, S. A. McKinney, T. Ha, Y. E. Goldman, and P. R. Selvin. "Myosin V walks hand-over-hand: Single fluorophore imaging with 1.5-nm localization". *Science* **300**, (2003), 2061.

[12] R. N. Ghosh and W. W. Webb. "Automated detection and tracking of individual and clustered cell surface low density lipoprotein receptor molecules". *Biophys. J.* **66**, (1994), 1301–1318.

[13] H. P. Kao and A. S. Verkman. "Tracking of single fluorescent particles in three dimensions: use of cylindrical optics to encode particle position." *Biophys. J.* **67**, (1994), 1291–1300.

[14] G. J. Schütz, H. Schindler, and T. Schmidt. "Single-molecule microscopy on model membranes reveals anomalous diffusion." *Biophys. J.* **73**, (1997), 1073–1080.

[15] U. Kubitscheck, O. Kuckmann, T. Kues, and R. Peters. "Imaging and tracking of single GFP molecules in solution." *Biophys. J.* **78**, (2000), 2170–2179.

[16] M. Goulian and S. M. Simon. "Tracking Single Proteins within Cells". *Biophys. J.* **79**, (2000), 2188–2198.

[17] R. M. Dickson, A. B. Cubitt, R. Y. Tsien, and W. E. Moerner. "On/off blinking and switching behaviour of single molecules of green fluorescent protein". *Nature* **388**, (1997), 355–358.

[18] D. W. Pierce, N. Hom-Booher, and R. D. Vale. "Imaging individual green fluorescent proteins". *Nature* **388**, (1997), 338.

[19] D. S. English, A. Furube, and P. F. Barbara. "Single-molecule spectroscopy in oxygen-depleted polymer films". *Chem. Phys. Lett.* **324**, (2000), 15–19.

[20] C. G. Hübner, A. Renn, I. Renge, and U. P. Wild. "Direct observation of the triplet lifetime quenching of single dye molecules by molecular oxygen". *J. Chem. Phys.* **115**, (2001), 9619–9622.

[21] F. Köhn, J. Hofkens, R. Gronheid, M. Van der Auweraer, and F. C. De Schryver. "Parameters Influencing the On- and Off-Times in the Fluorescence Intensity Traces of Single Cyanine Dye Molecules". *J. Phys. Chem. A* **106**, (2002), 4808–4814.

[22] M. Heilemann, E. Margeat, R. Kasper, M. Sauer, and P. Tinnefeld. "Carbocyanine Dyes as Efficient Reversible Single-Molecule Optical Switch". *J. Am. Chem. Soc.* **127**, (2005), 3801–3806.

[23] G. T. Dempsey, M. Bates, W. E. Kowtoniuk, D. R. Liu, R. Y. Tsien, and X. Zhuang. "Photoswitching Mechanism of Cyanine Dyes". *J. Am. Chem. Soc.* **131**, (2009), 18192–18193.

[24] G. T. Dempsey, J. C. Vaughan, K. H. Chen, M. Bates, and X. Zhuang. "Evaluation of fluorophores for optimal performance in localization-based super-resolution imaging". *Nat. Methods* **8**, (2011), 1027–1036.

[25] B. Huang, W. Wang, M. Bates, and X. Zhuang. "Three-dimensional super-resolution imaging by stochastic optical reconstruction microscopy". *Science* **319**, (2008), 810–813.

[26] S. Brasselet and W. E. Moerner. "Fluorescence behavior of single-molecule pH-sensors". *Single Mol.* **1**, (2000), 17.

[27] P. Tinnefeld, D. P. Herten, and M. Sauer. "Photophysical dynamics of single molecules studied by spectrally-resolved fluorescence lifetime imaging microscopy (SFLIM)". *J. Phys. Chem. A* **105**, (2001), 7989.

[28] W. E. Moerner and D. P. Fromm. "Methods of single-molecule fluorescence spectroscopy and microscopy". *Rev. Sci. Instrum.* **74**, (2003), 3597.

[29] M. Bossi, J. Folling, V. N. Belov, V. P. Boyarskiy, R. Medda, A. Egner, C. Eggeling, A. Schonle, and S. W. Hell. "Multicolor far-field fluorescence nanoscopy through isolated detection of distinct molecular species". *Nano Lett.* **8**, (2008), 2463.

[30] I. Testa, C. A. Wurm, R. Medda, E. Rothermel, C. von Middendorf, J. Folling, S. Jakobs, A. Schonle, S. W. Hell, and C. Eggeling. "Multicolor fluorescence nanoscopy in fixed and living cells by exciting conventional fluorophores with a single wavelength". *Biophys. J.* **99**, (2010), 2686.

[31] M. S. Gunewardene, F. V. Subach, T. J. Gould, G. P. Penoncello, M. V. Gudheti, V. V. Verkhusha, and S. T. Hess. "Superresolution imaging of multiple fluorescent proteins with highly overlapping emission spectra in living cells". *Biophys. J.* **101**, (2011), 1522.

[32] X. S. Xie and J. K. Trautman. "Optical studies of single molecules at room temperature". *Annu. Rev. Phys. Chem.* **49**, (1998), 441.

[33] W. E. Moerner and M. Orrit. "Illuminating single molecules in condensed matter". *Science* **283**, (1999), 1670.

[34] A. K. Luong, G. C. Gradinaru, D. W. Chandler, and C. C. Hayden. "Simultaneous time- and wavelength-resolved fluorescence microscopy of single molecules". *J. Phys. Chem. B* **109**, (2005), 15691.

[35] Z. Y. Zhang, S. J. Kenny, M. Hauser, W. Li, and K. Xu. "Ultrahigh-throughput single-molecule spectroscopy and spectrally resolved super-resolution microscopy". *Nat. Methods* **12**, (2015), 935.

[36] B. Q. Dong, L. Almassalha, B. E. Urban, T. Q. Nguyen, S. Khuon, T. L. Chew, V. Backman, C. Sun, and H. F. Zhang. "Super-resolution spectroscopic microscopy via photon localization". *Nat. Commun.* **7**, (2016), 12290.

[37] K. J. Buckler and R. D. Vaughan-Jones. "Application of a new pH-sensitive fluoroprobe (carboxy-SNARF-1) for intracellular pH measurement in small, isolated cells". *Pflügers Archiv* **417**, (1990), 234–239.

[38] G. Miesenböck, D. A. De Angelis, and J. E. Rothman. "Visualizing secretion and synaptic transmission with pH-sensitive green fluorescent proteins". *Nature* **394**, (1998), 192–195.

[39] M. Kneen, J. Farinas, Y. Li, and A. S. Verkman. "Green Fluorescent Protein as a Noninvasive Intracellular pH Indicator". *Biophys. J.* **74**, (1998), 1591–1599.

[40] R. C. Hunter and T. J. Beveridge. "Application of a pH-Sensitive Fluoroprobe (C-SNARF-4) for pH Microenvironment Analysis in Pseudomonas aeruginosa Biofilms". *Appl. Environ. Microbiol.* **71**, (2005), 2501–2510.

[41] J. Han and K. Burgess. "Fluorescent indicators for intracellular pH". *Chem. Rev.* **110**, (2010), 2709.

[42] C. Reichardt. "Solvatochromic dyes as solvent polarity indicators". *Chem. Rev.* **94**, (1994).

[43] O. A. Kucherak, S. Oncul, Z. Darwich, D. A. Yushchenko, Y. Arntz, P. Didier, Y. Mély, and A. S. Klymchenko. "Switchable Nile Red-Based Probe for Cholesterol and Lipid Order at the Outer Leaflet of Biomembranes". *J. Am. Chem. Soc.* **132**, (2010), 4907–4916.

[44] A. S. Klymchenko. "Solvatochromic and fluorogenic dyes as environment-sensitive probes: design and biological applications". *Acc. Chem. Res.* **50**, (2017), 366.

[45] M. W. Roe, J. J. Lemasters, and B. Herman. "Assessment of Fura-2 for measurements of cytosolic free calcium". *Cell Calcium* **11**, (1990), 63–73.

[46] M. Collot, F. Ponsot, and A. S. Klymchenko. "Ca-NIR: a ratiometric near-infrared calcium probe based on a dihydroxanthene-hemicyanine fluorophore". *Chem. Commun.* **53**, (2017), 6117–6120.

[47] A. K. Geim and K. S. Novoselov. "The rise of graphene". *Nat. Mater* **6**, (2007), 183–191.

[48] K. S. Novoselov, A. K. Geim, S. V. Morozov, D. Jiang, Y. Zhang, S. V. Dubonos, I. V. Grigorieva, and A. A. Firsov. "Electric Field Effect in Atomically Thin Carbon Films". *Science* **306**, (2004), 666–669.

[49] K. S. Kim, Y. Zhao, H. Jang, S. Y. Lee, J. M. Kim, K. S. Kim, J.-H. Ahn, P. Kim, J.-Y. Choi, and B. H. Hong. "Large-scale pattern growth of graphene films for stretchable transparent electrodes". *Nature* **457**, (2009), 706–710.

[50] S. Bae, H. Kim, Y. Lee, X. Xu, J.-S. Park, Y. Zheng, J. Balakrishnan, T. Lei, H. Ri Kim, Y. I. Song, Y.-J. Kim, K. S. Kim, B. Özyilmaz, J.-H. Ahn, B. H. Hong, and S. Iijima. "Roll-to-roll production of 30-inch graphene films for transparent electrodes". *Nat. Nanotechnol.* **5**, (2010), 574–578.

[51] F. Bonaccorso, Z. Sun, T. Hasan, and A. C. Ferrari. "Graphene photonics and optoelectronics". *Nat. Photonics* **4**, (2010), 611–622.

[52] K. S. Novoselov, V. I. Fal'ko, L. Colombo, P. R. Gellert, M. G. Schwab, and K. Kim. "A roadmap for graphene". *Nature* **490**, (2012), 192–200.

[53] C. Casiraghi, A. Hartschuh, E. Lidorikis, H. Qian, H. Harutyunyan, T. Gokus, K. S. Novoselov, and A. C. Ferrari. "Rayleigh Imaging of Graphene and Graphene Layers". *Nano Lett.* **7**, (2007), 2711–2717.

[54] P. E. Gaskell, H. S. Skulason, C. Rodenchuk, and T. Szkopek. "Counting graphene layers on glass via optical reflection microscopy". *Appl. Phys. Lett.* **94**, (2009), 143101.

[55] M. Dorn, P. Lange, A. Chekushin, N. Severin, and J. P. Rabe. "High contrast optical detection of single graphenes on optically transparent substrates". *J. Appl. Phys.* **108**, (2010), 106101.

[56] H. Gonçalves, M. Belsley, C. Moura, T. Stauber, and P. Schellenberg. "Enhancing visibility of graphene on arbitrary substrates by microdroplet condensation". *Appl. Phys. Lett.* **97**, (2010), 231905.

[57] J. Kim, F. Kim, and J. Huang. "Seeing graphene-based sheets". *Mater. Today* **13**, (2010), 28–38.

[58] J. R. Kyle, C. S. Ozkan, and M. Ozkan. "Industrial graphene metrology". *Nanoscale* **4**, (2012), 3807–3819.

[59] P. Wang, Z.-B. Liu, X.-D. Chen, F. Xing, W.-S. Jiang, B. Dong, W. Xin, and J.-G. Tian. "Accurate layers determination of graphene on transparent substrate based on polarization-sensitive absorption effect". *Appl. Phys. Lett.* **103**, (2013), 181902.

[60] K. Xu, H. P. Babcock, and X. Zhuang. "Dual-objective STORM reveals three-dimensional filament organization in the actin cytoskeleton". *Nat. Methods* **9**, (2012), 185–188.

[61] G. van Meer, D. R. Voelker, and G. W. Feigenson. "Membrane lipids: where they are and how they behave". *Nat. Rev. Mol. Cell Biol.* **9**, (2008), 112.

[62] J. C. M. Holthuis and A. K. Menon. "Lipid landscapes and pipelines in membrane homeostasis". *Nature* **510**, (2014), 48–57.

[63] J. C. M. Holthuis and T. P. Levine. "Lipid traffic: floppy drives and a superhighway". *Nat. Rev. Mol. Cell Biol.* **6**, (2005), 209–220.

[64] G. van Meer and A. I. P. M. de Kroon. "Lipid map of the mammalian cell". *J. Cell Sci.* **124**, (2011), 5–8.

[65] D. M. Owen, C. Rentero, A. Magenau, A. Abu-Siniyeh, and K. Gaus. "Quantitative imaging of membrane lipid order in cells and organisms". *Nat. Protoc.* **7**, (2012), 24–35.

[66] O. Golfetto, E. Hinde, and E. Gratton. "Laurdan fluorescence lifetime discriminates cholesterol content from changes in fluidity in living cell membranes". *Biophys. J.* **104**, (2013), 1238.

[67] Y. Niko, P. Didier, Y. Mely, G. Konishi, and A. S. Klymchenko. "Bright and photostable push-pull pyrene dye visualizes lipid order variation between plasma and intracellular membranes". *Sci. Rep.* **6**, (2016), 18870.

[68] S. Munro. "Lipid Rafts: Elusive or Illusive?" *Cell* **115**, (2003), 377–388.

[69] D. Lingwood and K. Simons. "Lipid rafts as a membrane-organizing principle". *Science* **327**, (2010), 46.

[70] E. Sevcsik and G. J. Schütz. "With or without rafts? Alternative views on cell membranes". *Bioessays* **38**, (2016), 129–139.

[71] I. Levental and S. L. Veatch. "The Continuing Mystery of Lipid Rafts". *J. Mol. Biol.* Molecular Biology of Membrane Lipids **428**, (2016), 4749–4764.

[72] Klotzsch Enrico and Schütz Gerhard J. "A critical survey of methods to detect plasma membrane rafts". *Philos. Trans. Royal Soc. B* **368**, (2013), 20120033.

[73] A. S. Klymchenko and R. Kreder. "Fluorescent probes for lipid rafts: From model membranes to living cells". *Chem. Biol.* **21**, (2014), 97.

[74] M. Schäferling. "The Art of Fluorescence Imaging with Chemical Sensors". *Angew. Chem. Int. Ed.* **51**, (2012), 3532–3554.

[75] Z. Yang, J. Cao, Y. He, J. H. Yang, T. Kim, X. Peng, and J. S. Kim. "Macro-/micro-environment-sensitive chemosensing and biological imaging". *Chem. Soc. Rev.* **43**, (2014), 4563.

[76] A. P. Demchenko, Y. Mély, G. Duportail, and A. S. Klymchenko. "Monitoring Biophysical Properties of Lipid Membranes by Environment-Sensitive Fluorescent Probes". *Biophys. J.* **96**, (2009), 3461–3470.

[77] S. W. Hell. "Far-Field Optical Nanoscopy". *Science* **316**, (2007), 1153–1158.

[78] B. Huang, H. Babcock, and X. Zhuang. "Breaking the diffraction barrier: super-resolution imaging of cells". *Cell* **143**, (2010), 1047–1058.

[79] G. Patterson, M. Davidson, S. Manley, and J. Lippincott-Schwartz. "Superresolution Imaging using Single-Molecule Localization". *Annu. Rev. Phys. Chem.* **61**, (2010), 345–367.

[80] M. D. Lew. "Three-dimensional super resolution colocalization of intracellular protein superstructures and the cell surface in live Caulobacter crescentus". *Proc. Natl Acad. Sci. USA* **108**, (2011).

[81] M. J. Mlodzianoski, N. M. Curthoys, M. S. Gunewardene, S. Carter, and S. T. Hess. "Super-resolution imaging of molecular emission spectra and single molecule spectral fluctuations". *PLOS ONE* **11**, (2016), e0147506.

[82] M. N. Bongiovanni, J. Godet, M. H. Horrocks, L. Tosatto, A. R. Carr, D. C. Wirthensohn, R. T. Ranasinghe, J. E. Lee, A. Ponjavic, J. V. Fritz, C. M. Dobson, D. Klenerman, and S. F. Lee. "Multi-dimensional super-resolution imaging enables surface hydrophobicity mapping". *Nat. Commun.* **7**, (2016), 13544.

[83] M. Hauser, M. Wojcik, D. Kim, M. Mahmoudi, W. Li, and K. Xu. "Correlative super-resolution microscopy: new dimensions and new opportunities". *Chem. Rev.* **117**, (2017), 7428.

[84] L. Carlini and S. Manley. "Live Intracellular Super-Resolution Imaging Using Site-Specific Stains". *ACS Chem. Biol.* **8**, (2013), 2643–2648.

[85] Y. Ma, M. R. Shortreed, and E. S. Yeung. "High-throughput single-molecule spectroscopy in free solution". *Anal. Chem.* **72**, (2000), 4640.

[86] S. H. Shim. "Super-resolution fluorescence imaging of organelles in live cells with photoswitchable membrane probes". *Proc. Natl Acad. Sci. USA* **109**, (2012).

[87] H. P. Lu and X. S. Xie. "Single-molecule spectral fluctuations at room temperature". *Nature* **385**, (1997), 143.

[88] R. Zidovetzki and I. Levitan. "Use of cyclodextrins to manipulate plasma membrane cholesterol content: Evidence, misconceptions and control strategies". *Biochim. Biophys. Acta* **1768**, (2007), 1311–1324.

[89] T. S. v. Zanten, J. Gómez, C. Manzo, A. Cambi, J. Buceta, R. Reigada, and M. F. Garcia-Parajo. "Direct mapping of nanoscale compositional connectivity on intact cell membranes". *Proc. Natl Acad. Sci. USA* **107**, (2010), 15437–15442.

[90] P. Greenspan and S. D. Fowler. "Spectrofluorometric studies of the lipid probe, nile red". *J. Lipid Res.* **26**, (1985).

[91] A. Honigmann, V. Mueller, H. Ta, A. Schoenle, E. Sezgin, S. W. Hell, and C. Eggeling. "Scanning STED-FCS reveals spatiotemporal heterogeneity of lipid interaction in the plasma membrane of living cells". *Nat. Commun.* **5**, (2014), 5412.

[92] E. Sevcsik, M. Brameshuber, M. Fölser, J. Weghuber, A. Honigmann, and G. J. Schütz. "GPI-anchored proteins do not reside in ordered domains in the live cell plasma membrane". *Nat. Commun.* **6**, (2015), 6969.

[93] K. W. Bewig and W. A. Zisman. "The wetting of gold and platinum by water". *J. Phys. Chem.* **69**, (1965).

[94] T. Smith. "The hydrophilic nature of a clean gold surface". *J. Colloid Interface Sci.* **75**, (1980).

[95] W. Den, H. L. Bai, and Y. H. Kang. "Organic airborne molecular contamination in semiconductor fabrication clean rooms—a review". *J. Electrochem. Soc.* **153**, (2006).

[96] Z. T. Li. "Effect of airborne contaminants on the wettability of supported graphene and graphite". *Nat. Mater.* **12**, (2013).

[97] J. F. Weaver, A. F. Carlsson, and R. J. Madix. "The adsorption and reaction of low molecular weight alkanes on metallic single crystal surfaces". *Surf. Sci. Rep.* **50**, (2003).

[98] K. U. Goss. "The air/surface adsorption equilibrium of organic compounds under ambient conditions". *Crit. Rev. Environ. Sci. Technol.* **34**, (2004).

[99] E. Hilner. "The effect of ionic strength on oil adhesion in sandstone—the search for the low salinity mechanism". *Sci. Rep.* **5**, (2015).

[100] L. Xu, M. Salmeron, and S. Bardon. "Wetting and molecular orientation of 8CB on silicon substrates". *Phys. Rev. Lett.* **84**, (2000).

[101] L. Xu. "De-wetting of lubricants on hard disks". *J. Chem. Phys.* **112**, (2000).

[102] T. Gowthami, G. Tamilselvi, G. Jacob, and G. Raina. "The role of ambient ice-like water adlayers formed at the interfaces of graphene on hydrophobic and hydrophilic substrates probed using scanning probe microscopy". *Phys. Chem. Chem. Phys.* **17**, (2015).

[103] K. Xu, P. G. Cao, and J. R. Heath. "Graphene visualizes the first water adlayers on mica at ambient conditions". *Science* **329**, (2010), 1188–1191.

[104] P. G. Cao, K. Xu, J. O. Varghese, and J. R. Heath. "Atomic force microscopy characterization of room-temperature adlayers of small organic molecules through graphene templating". *J. Am. Chem. Soc.* **133**, (2011), 2334–2337.

[105] P. G. Cao, K. Xu, J. O. Varghese, and J. R. Heath. "The microscopic structure of adsorbed water on hydrophobic surfaces under ambient conditions". *Nano. Lett.* **11**, (2011).

[106] S. J. Sahl, S. W. Hell, and S. Jakobs. "Fluorescence nanoscopy in cell biology". *Nat. Rev. Mol. Cell. Biol.* **18**, (2017), 685.

[107] D. M. Wu, Z. W. Liu, C. Sun, and X. Zhang. "Super-resolution imaging by random adsorbed molecule probes". *Nano. Lett.* **8**, (2008).

[108] R. Walder, N. Nelson, and D. K. Schwartz. "Super-resolution surface mapping using the trajectories of molecular probes". *Nat. Commun.* **2**, (2011).

[109] L. Albertazzi. "Probing exchange pathways in one-dimensional aggregates with super-resolution microscopy". *Science* **344**, (2014).

[110] C. E. Boott. "In situ visualization of block copolymer self-assembly in organic media by super-resolution fluorescence microscopy". *Chem. Eur. J.* **21**, (2015).

[111] A. Aloi, N. Vilanova, L. Albertazzi, and I. K. Voets. "iPAINT: a general approach tailored to image the topology of interfaces with nanometer resolution". *Nanoscale* **8**, (2016).

[112] D. Wöll and C. Flors. "Super-resolution fluorescence imaging for materials science". *Small Methods* **1**, (2017).

[113] Y. Hou, A. M. Bardo, C. Martinez, and D. A. Higgins. "Characterization of molecular scale environments in polymer films by single molecule spectroscopy". *J. Phys. Chem. B.* **104**, (2000), 212.

[114] S. A. Mutch. "Deconvolving single-molecule intensity distributions for quantitative microscopy measurements". *Biophys. J.* **92**, (2007).

[115] K. I. Mortensen, L. S. Churchman, J. A. Spudich, and H. Flyvbjerg. "Optimized localization analysis for single-molecule tracking and super-resolution microscopy". *Nat. Methods* **7**, (2010).

[116] P. Tinnefeld, C. Eggeling, and S. W. Hell. *Far-Field Optical Nanoscopy*. Springer, 2015.

[117] A. Mendez-Vilas, A. B. Jodar-Reyes, and M. L. Gonzalez-Martin. "Ultrasmall liquid droplets on solid surfaces: production, imaging, and relevance for current wetting research". *Small* **5**, (2009).

[118] B. Cunderlikova and L. Sikurova. "Solvent effects on photophysical properties of merocyanine 540". *Chem. Phys.* **263**, (2001).

[119] N. Severin. "Nanophase separation in monomolecularly thin water-ethanol films controlled by graphene". *Nano. Lett.* **15**, (2015).

[120] P. Bampoulis. "Structure and dynamics of confined alcohol-water mixtures". *ACS Nano* **10**, (2016).

[121] M. Zinke-Allmang. "Phase separation on solid surfaces: nucleation, coarsening and coalescence kinetics". *Thin Solid Films* **346**, (1999).

[122] P. Muller-Buschbaum, E. Bauer, O. Wunnicke, and M. Stamm. "The control of thin film morphology by the interplay of dewetting, phase separation and microphase separation". *J. Phys. Condens. Matter* **17**, (2005).

[123] C. Bernardini, S. D. Stoyanov, L. N. Arnaudov, and M. A. C. Stuart. "Colloids in Flatland: a perspective on 2D phase-separated systems, characterisation methods, and lineactant design". *Chem. Soc. Rev.* **42**, (2013).

[124] A. von Diezmann, Y. Shechtman, and W. E. Moerner. "Three-dimensional localization of single molecules for super-resolution imaging and single-particle tracking". *Chem. Rev.* **117**, (2017), 7244–7275.

[125] G. Shtengel, J. A. Galbraith, C. G. Galbraith, J. Lippincott-Schwartz, J. M. Gillette, S. Manley, R. Sougrat, C. M. Waterman, P. Kanchanawong, M. W. Davidson, R. D. Fetter, and H. F. Hess. "Interferometric fluorescent super-resolution microscopy resolves 3D cellular ultrastructure". *Proc. Natl Acad. Sci. USA* **106**, (2009), 3125–3130.

[126] S. R. P. Pavani, M. A. Thompson, J. S. Biteen, S. J. Lord, N. Liu, R. J. Twieg, R. Piestun, and W. E. Moerner. "Three-dimensional, single-molecule fluorescence imaging beyond the diffraction limit by using a double-helix point spread function". *Proc. Natl Acad. Sci. USA* **106**, (2009), 2995–2999.

[127] Y. Shechtman, L. E. Weiss, A. S. Backer, M. Y. Lee, and W. E. Moerner. "Multicolour localization microscopy by point-spread-function engineering". *Nat. Photonics* **10**, (2016), 590.

[128] C. Smith, M. Huisman, M. Siemons, D. Grunwald, and S. Stallinga. "Simultaneous measurement of emission color and 3D position of single molecules". *Opt. Express* **24**, (2016), 4996.

[129] M. Siemons, C. N. Hulleman, R. Ø. Thorsen, C. S. Smith, and S. Stallinga. "High precision wavefront control in point spread function engineering for single emitter localization". *Opt. Express* **26**, (2018), 8397–8416.

[130] C. Franke, M. Sauer, and S. van de Linde. "Photometry unlocks 3D information from 2D localization microscopy data". *Nat. Methods* **14**, (2016), 41–44.

[131] Y. Li, M. Mund, P. Hoess, J. Deschamps, U. Matti, B. Nijmeijer, V. J. Sabinina, J. Ellenberg, I. Schoen, and J. Ries. "Real-time 3D single-molecule localization using experimental point spread functions". *Nat. Methods* **15**, (2018), 367–369.

[132] S. F. Gibson and F. Lanni. "Diffraction by a circular aperture as a model for three-dimensional optical microscopy". *J. Opt. Soc. Am. A* **6**, (1989), 1357.

[133] H. P. Babcock and X. Zhuang. "Analyzing single molecule localization microscopy data using cubic splines". *Sci. Rep.* **7**, (2017), 552.

[134] T. Kuntzer, M. Tewes, and F. Courbin. "Stellar classification from single-band imaging using machine learning". *Astronomy & Astrophysics* **591**, (2016), A54.

[135] J. M. Newby, A. M. Schaefer, P. T. Lee, M. G. Forest, and S. K. Lai. "Convolutional neural networks automate detection for tracking of submicron-scale particles in 2D and 3D". *Proc. Natl Acad. Sci. USA* **115**, (2018), 9026–9031.

[136] P. Zelger, K. Kaser, B. Rossboth, L. Velas, G. J. Schütz, and A. Jesacher. "Three-dimensional localization microscopy using deep learning". *Opt. Express* **26**, (2018), 33166–33179.

[137] X. Glorot and Y. Bengio. "Understanding the difficulty of training deep feedforward neural networks". *Proceedings of the Thirteenth International Conference on Artificial Intelligence and Statistics*. Proceedings of the Thirteenth International Conference on Artificial Intelligence and Statistics, 2010, 249–256.

[138] R. M. Zur, Y. Jiang, L. L. Pesce, and K. Drukker. "Noise injection for training artificial neural networks: A comparison with weight decay and early stopping". *Med. Phys.* **36**, (2009), 4810–4818.

[139] S. Liu, E. B. Kromann, W. D. Krueger, J. Bewersdorf, and K. A. Lidke. "Three dimensional single molecule localization using a phase retrieved pupil function". *Opt. Express* **21**, (2013), 29462–29487.

[140] K. Hara, R. Vemulapalli, and R. Chellappa. "Designing deep convolutional neural networks for continuous object orientation estimation". *arXiv:1702.01499 [cs]* (2017).

[141] M. Ovesný, P. Křížek, J. Borkovec, Z. Švindrych, and G. M. Hagen. "ThunderSTORM: a comprehensive ImageJ plug-in for PALM and STORM data analysis and super-resolution imaging". *Bioinformatics* **30**, (2014), 2389–2390.

[142] B. Huang, M. Bates, and X. Zhuang. "Super-resolution fluorescence microscopy". *Annu. Rev. Biochem.* **78**, (2009), 993.

[143] T. Chen, B. Dong, K. Chen, F. Zhao, X. Cheng, C. Ma, S. Lee, P. Zhang, S. H. Kang, J. W. Ha, W. Xu, and N. Fang. "Optical super-resolution imaging of surface reactions". *Chem. Rev.* **117**, (2017), 7510.

[144] C. Joo, H. Balci, Y. Ishitsuka, C. Buranachai, and T. Ha. "Advances in single-molecule fluorescence methods for molecular biology". *Annu. Rev. Biochem.* **77**, (2008), 51.

[145] T. Cordes and S. A. Blum. "Opportunities and challenges in single-molecule and single-particle fluorescence microscopy for mechanistic studies of chemical reactions". *Nat. Chem.* **5**, (2013), 993.

[146] S. T. Hess, T. P. K. Girirajan, and M. D. Mason. "Ultra-high resolution imaging by fluorescence photoactivation localization microscopy". *Biophys. J.* **91**, (2006), 4258.

[147] P. Chen, X. Zhou, N. M. Andoy, K. S. Han, E. Choudhary, N. Zou, G. Chen, and H. Shen. "Spatiotemporal catalytic dynamics within single nanocatalysts revealed by single-molecule microscopy". *Chem. Soc. Rev.* **43**, (2014), 1107.

[148] J. K. Trautman, J. J. Macklin, L. E. Brus, and E. Betzig. "Near-field spectroscopy of single molecules at room-temperature". *Nature* **369**, (1994), 40.

[149] J. J. Macklin, J. K. Trautman, T. D. Harris, and L. E. Brus. "Imaging and time-resolved spectroscopy of single molecules at an interface". *Science* **272**, (1996), 255.

[150] P. M. Lundquist, C. F. Zhong, P. Zhao, A. B. Tomaney, P. S. Peluso, J. Dixon, B. Bettman, Y. Lacroix, D. P. Kwo, E. McCullough, M. Maxham, K. Hester, P. McNitt, D. M. Grey, C. Henriquez, M. Foquet, S. W. Turner, and D. Zaccarin. "Parallel confocal detection of single molecules in real time". *Opt. Lett.* **33**, (2008), 1026.

[151] S. B. Howell. *Handbook of CCD Astronomy*. Ed. by 2. 2006.

[152] L. Wei, C. Liu, B. Chen, P. Zhou, H. Li, L. Xiao, and E. S. Yeung. "Probing single-molecule fluorescence spectral modulation within individual hotspots with subdiffraction-limit image resolution". *Anal. Chem.* **85**, (2013), 3789.

[153] D. Kim, Z. Zhang, and K. Xu. "Spectrally resolved super-resolution microscopy unveils multipath reaction pathways of single spiropyran molecules". *J. Am. Chem. Soc.* **139**, (2017), 9447.

[154] Q. Wang and W. E. Moerner. "Lifetime and spectrally resolved characterization of the photodynamics of single fluorophores in solution using the anti-Brownian electrokinetic trap". *J. Phys. Chem. B* **117**, (2013), 4641.

[155] J. Broeken, B. Rieger, and S. Stallinga. "Simultaneous measurement of position and color of single fluorescent emitters using diffractive optics". *Opt. Lett.* **39**, (2014), 3352.

[156] J. Comtet, E. Glushkov, V. Navikas, J. Feng, V. Babenko, S. Hofmann, K. Watanabe, T. Taniguchi, and A. Radenovic. "Wide-field spectral super-resolution mapping of optically active defects in hBN". *arXiv:1901.06989 [cond-mat, physics:physics]* (2019). arXiv: 1901.06989.

[157] P. Nuernberger, S. Ruetzel, and T. Brixner. "Multidimensional electronic spectroscopy of photochemical reactions". *Angew. Chem., Int. Ed.* **54**, (2015), 11368.

[158] J. V. Small, K. Rottner, P. Hahne, and K. I. Anderson. "Visualising the actin cytoskeleton". *Microsc. Res. Tech.* **47**, (1999), 3–17.

[159] T. Svitkina. "Electron microscopic analysis of the leading edge in migrating cells". *Methods Cell Biol.* **79**, (2007), 295–319.

[160] H. Schatten and J. B. Pawley, eds. *Biological low voltage field emission scanning electron microscopy*. OCLC: ocn166358120. New York ; London: Springer, 2008.

[161] S. Watanabe. "Protein localization in electron micrographs using fluorescence nanoscopy". *Nat. Methods* **8**, (2011), 80–84.

[162] B. G. Kopek, G. Shtengel, C. S. Xu, D. A. Clayton, and H. F. Hess. "Correlative 3D super resolution fluorescence and electron microscopy reveal the relationship of mitochondrial nucleoids to membranes". *Proc. Natl Acad. Sci. Usa* **109**, (2012), 6136–6141.

[163] K. A. Sochacki, G. Shtengel, S. B. van Engelenburg, H. F. Hess, and J. W. Taraska. "Correlative super-resolution fluorescence and metal-replica transmission electron microscopy". *Nat. Methods* **11**, (2014), 305–308.

[164] N. de Jonge and F. M. Ross. "Electron microscopy of specimens in liquid". *Nat. Nanotechnol.* **6**, (2011), 695–704.

[165] L. F. Kourkoutis, J. M. Plitzko, and W. Baumeister. "Electron microscopy of biological materials at the nanometer scale". *Annu. Rev. Mater. Res.* **42**, (2012), 33–58.

[166] S. Thiberge. "Scanning electron microscopy of cells and tissues under fully hydrated conditions". *Proc. Natl Acad. Sci. Usa* **101**, (2004), 3346–3351.

[167] N. de Jonge, D. B. Peckys, G. J. Kremers, and D. W. Piston. "Electron microscopy of whole cells in liquid with nanometer resolution". *Proc. Natl Acad. Sci. Usa* **106**, (2009), 2159–2164.

[168] H. Nishiyama. "Atmospheric scanning electron microscope observes cells and tissues in open medium through silicon nitride film". *J. Struct. Biol.* **169**, (2010), 438–449.

[169] D. B. Peckys, P. Mazur, K. L. Gould, and N. de Jonge. "Fully hydrated yeast cells imaged with electron microscopy". *Biophys. J.* **100**, (2011), 2522–2529.

[170] E. A. Ring, D. B. Peckys, M. J. Dukes, J. P. Baudoin, and N. de Jonge. "Silicon nitride windows for electron microscopy of whole cells". *J. Microsc.* **243**, (2011), 273–283.

[171] J. S. Bunch. "Impermeable atomic membranes from graphene sheets". *Nano Lett.* **8**, (2008), 2458–2462.

[172] E. Stolyarova. "Observation of graphene bubbles and effective mass transport under graphene films". *Nano Lett.* **9**, (2009), 332–337.

[173] S. Chen. "Oxidation resistance of graphene-coated Cu and Cu/Ni alloy". *ACS Nano* **5**, (2011), 1321–1327.

[174] V. Berry. "Impermeability of graphene and its applications". *Carbon N. Y.* **62**, (2013), 1–10.

[175] P. G. Cao, J. O. Varghese, K. Xu, and J. R. Heath. "Visualizing local doping effects of individual water clusters on gold(111)-supported graphene". *Nano Lett.* **12**, (2012), 1459–1463.

[176] J. C. Meyer, C. O. Girit, M. F. Crommie, and A. Zettl. "Imaging and dynamics of light atoms and molecules on graphene". *Nature* **454**, (2008), 319–322.

[177] R. R. Nair. "Graphene as a transparent conductive support for studying biological molecules by transmission electron microscopy". *Appl. Phys. Lett.* **97**, (2010), 153102.

[178] J. M. Yuk. "High-resolution EM of colloidal nanocrystal growth using graphene liquid cells". *Science* **336**, (2012), 61–64.

[179] Q. Chen. "3D motion of DNA-Au nanoconjugates in graphene liquid cell electron microscopy". *Nano Lett.* **13**, (2013), 4556–4561.

[180] C. H. Wang, Q. Qiao, T. Shokuhfar, and R. F. Klie. "High-resolution electron microscopy and spectroscopy of ferritin in biocompatible graphene liquid cells and graphene sandwiches". *Adv. Mater.* **26**, (2014), 3410–3414.

[181] N. Mohanty, M. Fahrenholtz, A. Nagaraja, D. Boyle, and V. Berry. "Impermeable graphenic encasement of bacteria". *Nano Lett.* **11**, (2011), 1270–1275.

[182] Y. F. Li. "Graphene microsheets enter cells through spontaneous membrane penetration at edge asperities and corner sites". *Proc. Natl Acad. Sci. Usa* **110**, (2013), 12295–12300.

[183] A. C. Ferrari. "Raman spectrum of graphene and graphene layers". *Phys. Rev. Lett.* **97**, (2006), 187401.

[184] X. S. Li. "Large-area synthesis of high-quality and uniform graphene films on copper foils". *Science* **324**, (2009), 1312–1314.

[185] R. R. Nair, P. Blake, A. N. Grigorenko, K. S. Novoselov, T. J. Booth, T. Stauber, N. M. R. Peres, and A. K. Geim. "Fine structure constant defines visual transparency of graphene". *Science* **320**, (2008), 1308–1308.

[186] K. Xu, S.-H. Shim, and X. Zhuang. "Super-Resolution Imaging Through Stochastic Switching and Localization of Single Molecules: An Overview". *Far-Field Optical Nanoscopy*. Springer Series on Fluorescence. Springer, Berlin, Heidelberg, 2013, 27–64.

[187] H. Li and J. C. Vaughan. "Switchable Fluorophores for Single-Molecule Localization Microscopy". *Chem. Rev.* **118**, (2018), 9412–9454.

[188] S. A. Jones, S.-H. Shim, J. He, and X. Zhuang. "Fast three-dimensional super-resolution imaging of live cells". *Nat. Methods* **8**, (2011), 499–508.

[189] M. P. Stewart, A. Sharei, X. Ding, G. Sahay, R. Langer, and K. F. Jensen. "*In vitro* and *ex vivo* strategies for intracellular delivery". *Nature* **538**, (2016), 183–192.

[190] M. P. Stewart, R. Langer, and K. F. Jensen. "Intracellular Delivery by Membrane Disruption: Mechanisms, Strategies, and Concepts". *Chem. Rev.* **118**, (2018), 7409–7531.

[191] J. C. Brooks and S. Treml. "Catecholamine secretion by chemically skinned cultured chromaffin cells". *J. Neurochem.* **40**, (1983), 468–473.

[192] I. Schulz. "[19] Permeabilizing cells: Some methods and applications for the study of intracellular processes". *Methods in Enzymology*. Vol. 192. Biomembranes Part W: Cellular and Subcellular Transport: Epithelial Cells. Academic Press, 1990, 280–300.

[193] A. L. van de Ven, K. Adler-Storthz, and R. Richards-Kortum. "Delivery of Optical Contrast Agents using Triton-X100, Part 1: Reversible permeabilization of live cells for intracellular labeling". *J. Biomed. Opt.* **14**, (2009), 021012.

[194] G. Ahnert-Hilger, S. Bhakdi, and M. Gratzl. "Minimal requirements for exocytosis. A study using PC 12 cells permeabilized with staphylococcal alpha-toxin". *J. Biol. Chem.* **260**, (1985), 12730–12734.

[195] K. W. Teng, Y. Ishitsuka, P. Ren, Y. Youn, X. Deng, P. Ge, S. H. Lee, A. S. Belmont, and P. R. Selvin. "Labeling Proteins Inside Living Cells Using External Fluorophores for Fluorescence Microscopy". *eLife* **6**, (2017), e25460.

[196] D. Koley and A. J. Bard. "Triton X-100 concentration effects on membrane permeability of a single HeLa cell by scanning electrochemical microscopy (SECM)". *Proc. Natl Acad. Sci. USA* **107**, (2010), 16783–16787.

[197] M. R. Capecchi. "High efficiency transformation by direct microinjection of DNA into cultured mammalian cells". *Cell* **22**, (1980), 479–488.

[198] J. W. Gordon, G. A. Scangos, D. J. Plotkin, J. A. Barbosa, and F. H. Ruddle. "Genetic transformation of mouse embryos by microinjection of purified DNA". *Proc. Natl Acad. Sci. USA* **77**, (1980), 7380–7384.

[199] M. Fechheimer, J. F. Boylan, S. Parker, J. E. Sisken, G. L. Patel, and S. G. Zimmer. "Transfection of mammalian cells with plasmid DNA by scrape loading and sonication loading." *Proc. Natl Acad. Sci. USA* **84**, (1987), 8463–8467.

[200] S. Bao, B. D. Thrall, and D. L. Miller. "Transfection of a reporter plasmid into cultured cells by sonoporation in vitro". *Ultrasound Med. Biol.* **23**, (1997), 953–959.

[201] E. Neumann, M. Schaefer-Ridder, Y. Wang, and P. H. Hofschneider. "Gene transfer into mouse lyoma cells by electroporation in high electric fields". *EMBO J.* **1**, (1982), 841–845.

[202] S. Baron, J. Poast, D. Rizzo, E. McFarland, and E. Kieff. "Electroporation of antibodies, DNA, and other macromolecules into cells: a highly efficient method". *J. Immunol. Methods* **242**, (2000), 115–126.

[203] M. L. Yarmush, A. Golberg, G. Serša, T. Kotnik, and D. Miklavčič. "Electroporation-based technologies for medicine: principles, applications, and challenges". *Annu Rev Biomed Eng* **16**, (2014), 295–320.

[204] J. Shi, Y. Ma, J. Zhu, Y. Chen, Y. Sun, Y. Yao, Z. Yang, and J. Xie. "A Review on Electroporation-Based Intracellular Delivery". *Molecules* **23**, (2018).

[205] W. Kim, J. K. Ng, M. E. Kunitake, B. R. Conklin, and P. Yang. "Interfacing Silicon Nanowires with Mammalian Cells". *J. Am. Chem. Soc.* **129**, (2007), 7228–7229.

[206] A. K. Shalek, J. T. Robinson, E. S. Karp, J. S. Lee, D.-R. Ahn, M.-H. Yoon, A. Sutton, M. Jorgolli, R. S. Gertner, T. S. Gujral, G. MacBeath, E. G. Yang, and H. Park. "Vertical silicon nanowires as a universal platform for delivering biomolecules into living cells". *Proc Natl Acad Sci U S A* **107**, (2010), 1870–1875.

[207] P. E. Boukany, A. Morss, W.-c. Liao, B. Henslee, H. Jung, X. Zhang, B. Yu, X. Wang, Y. Wu, L. Li, K. Gao, X. Hu, X. Zhao, O. Hemminger, W. Lu, G. P. Lafyatis, and L. J. Lee. "Nanochannel electroporation delivers precise amounts of biomolecules into living cells". *Nature Nanotechnology* **6**, (2011), 747–754.

[208] X. Xie, A. M. Xu, S. Leal-Ortiz, Y. Cao, C. C. Garner, and N. A. Melosh. "Nanostraw–Electroporation System for Highly Efficient Intracellular Delivery and Transfection". *ACS Nano* **7**, (2013), 4351–4358.

[209] X. Han, Z. Liu, M. c. Jo, K. Zhang, Y. Li, Z. Zeng, N. Li, Y. Zu, and L. Qin. "CRISPR-Cas9 delivery to hard-to-transfect cells via membrane deformation". *Sci Adv* **1**, (2015).

[210] Y. Cao, M. Hjort, H. Chen, F. Birey, S. A. Leal-Ortiz, C. M. Han, J. G. Santiago, S. P. Paşca, J. C. Wu, and N. A. Melosh. "Nondestructive nanostraw intracellular sampling for longitudinal cell monitoring". *Proc. Natl. Acad. Sci. U.S.A.* **114**, (2017), E1866–E1874.

[211] Y. Cao, E. Ma, S. Cestellos-Blanco, B. Zhang, R. Qiu, Y. Su, J. A. Doudna, and P. Yang. "Nontoxic nanopore electroporation for effective intracellular delivery of biological macromolecules". *PNAS* **116**, (2019), 7899–7904.

[212] P. Nguyen and V. Berry. "Graphene Interfaced with Biological Cells: Opportunities and Challenges". *J. Phys. Chem. Lett.* **3**, (2012), 1024–1029.

[213] K. Kostarelos and K. S. Novoselov. "Exploring the Interface of Graphene and Biology". *Science* **344**, (2014), 261–263.

[214] C. Cheng, S. Li, A. Thomas, N. A. Kotov, and R. Haag. "Functional Graphene Nanomaterials Based Architectures: Biointeractions, Fabrications, and Emerging Biological Applications". *Chem. Rev.* **117**, (2017), 1826–1914.

[215] A. Pierres, V. Monnet-Corti, A.-M. Benoliel, and P. Bongrand. "Do membrane undulations help cells probe the world?" *Trends Cell Biol.* **19**, (2009), 428–433.

[216] M. Kalbacova, A. Broz, J. Kong, and M. Kalbac. "Graphene substrates promote adherence of human osteoblasts and mesenchymal stromal cells". *Carbon* **48**, (2010), 4323–4329.

[217] N. Li, X. Zhang, Q. Song, R. Su, Q. Zhang, T. Kong, L. Liu, G. Jin, M. Tang, and G. Cheng. "The promotion of neurite sprouting and outgrowth of mouse hippocampal cells in culture by graphene substrates". *Biomaterials* **32**, (2011), 9374–9382.

[218] J. Riedl, A. H. Crevenna, K. Kessenbrock, J. H. Yu, D. Neukirchen, M. Bista, F. Bradke, D. Jenne, T. A. Holak, Z. Werb, M. Sixt, and R. Wedlich-Soldner. "Lifeact: a versatile marker to visualize F-actin". *Nat. Methods* **5**, (2008), 605–607.

[219] P. Blake, E. W. Hill, A. H. Castro Neto, K. S. Novoselov, D. Jiang, R. Yang, T. J. Booth, and A. K. Geim. "Making graphene visible". *Appl. Phys. Lett.* **91**, (2007), 063124.

[220] Z. H. Ni, H. M. Wang, J. Kasim, H. M. Fan, T. Yu, Y. H. Wu, Y. P. Feng, and Z. X. Shen. "Graphene Thickness Determination Using Reflection and Contrast Spectroscopy". *Nano Lett.* **7**, (2007), 2758–2763.

[221] P. Romagnoli, H. G. Rosa, D. Lopez-Cortes, E. A. T. Souza, J. C. Viana-Gomes, W. Margulis, and C. J. S. d. Matos. "Making graphene visible on transparent dielectric substrates: Brewster angle imaging". *2D Materials* **2**, (2015), 035017.

[222] E. Treossi, M. Melucci, A. Liscio, M. Gazzano, P. Samorì, and V. Palermo. "High-Contrast Visualization of Graphene Oxide on Dye-Sensitized Glass, Quartz, and Silicon by Fluorescence Quenching". *J. Am. Chem. Soc.* **131**, (2009), 15576–15577.

[223] J. Kim, L. J. Cote, F. Kim, and J. Huang. "Visualizing Graphene Based Sheets by Fluorescence Quenching Microscopy". *J. Am. Chem. Soc.* **132**, (2010), 260–267.

[224] J. R. Kyle, A. Guvenc, W. Wang, M. Ghazinejad, J. Lin, S. Guo, C. S. Ozkan, and M. Ozkan. "Centimeter-Scale High-Resolution Metrology of Entire CVD-Grown Graphene Sheets". *Small* **7**, (2011), 2599–2606.

[225] A. S. G. Curtis. "THE MECHANISM OF ADHESION OF CELLS TO GLASS: A Study by Interference Reflection Microscopy". *J. Cell Biol.* **20**, (1964), 199–215.

[226] H. Verschueren. "Interference reflection microscopy in cell biology: methodology and applications". *J. Cell Sci.* **75**, (1985), 279–301.

[227] L. Limozin and K. Sengupta. "Quantitative Reflection Interference Contrast Microscopy (RICM) in Soft Matter and Cell Adhesion". *ChemPhysChem* **10**, (2009), 2752–2768.

[228] A. Reina, H. Son, L. Jiao, B. Fan, M. S. Dresselhaus, Z. Liu, and J. Kong. "Transferring and Identification of Single- and Few-Layer Graphene on Arbitrary Substrates". *J. Phys. Chem. C* **112**, (2008), 17741–17744.

[229] S. Cheon, K. D. Kihm, H. g. Kim, G. Lim, J. S. Park, and J. S. Lee. "How to Reliably Determine the Complex Refractive Index (RI) of Graphene by Using Two Independent Measurement Constraints". *Sci. Rep.* **4**, (2014), 6364.

[230] W. Zhu, T. Low, V. Perebeinos, A. A. Bol, Y. Zhu, H. Yan, J. Tersoff, and P. Avouris. "Structure and Electronic Transport in Graphene Wrinkles". *Nano Lett.* **12**, (2012), 3431–3436.

[231] V. G. Kravets, A. N. Grigorenko, R. R. Nair, P. Blake, S. Anissimova, K. S. Novoselov, and A. K. Geim. "Spectroscopic ellipsometry of graphene and an exciton-shifted van Hove peak in absorption". *Phys. Rev. B* **81**, (2010), 155413.

[232] K. F. Mak, M. Y. Sfeir, J. A. Misewich, and T. F. Heinz. "The evolution of electronic structure in few-layer graphene revealed by optical spectroscopy". *Proc. Natl Acad. Sci. USA* **107**, (2010), 14999–15004.

[233] M. N. Cizmeciyan, J. W. Kim, S. Bae, B. H. Hong, F. Rotermund, and A. Sennaroglu. "Graphene mode-locked femtosecond Cr:ZnSe laser at 2500 nm". *Opt. Lett.* **38**, (2013), 341–343.

[234] P. Klar, E. Lidorikis, A. Eckmann, I. A. Verzhbitskiy, A. C. Ferrari, and C. Casiraghi. "Raman scattering efficiency of graphene". *Phys. Rev. B* **87**, (2013), 205435.

[235] G. Tsoukleri, J. Parthenios, K. Papagelis, R. Jalil, A. C. Ferrari, A. K. Geim, K. S. Novoselov, and C. Galiotis. "Subjecting a Graphene Monolayer to Tension and Compression". *Small* **5**, (2009), 2397–2402.

[236] O. Frank, G. Tsoukleri, I. Riaz, K. Papagelis, J. Parthenios, A. C. Ferrari, A. K. Geim, K. S. Novoselov, and C. Galiotis. "Development of a universal stress sensor for graphene and carbon fibres". *Nat. Commun.* **2**, (2011), 255.

[237] D. C. Miller, R. R. Foster, Y. Zhang, S.-H. Jen, J. A. Bertrand, Z. Lu, D. Seghete, J. L. O'Patchen, R. Yang, Y.-C. Lee, S. M. George, and M. L. Dunn. "The mechanical robustness of atomic-layer- and molecular-layer-deposited coatings on polymer substrates". *J. Appl. Phys.* **105**, (2009), 093527.

[238] C. Peng, Z. Jia, H. Neilson, T. Li, and J. Lou. "In Situ Electro-Mechanical Experiments and Mechanics Modeling of Fracture in Indium Tin Oxide-Based Multilayer Electrodes". *Adv. Eng. Mater.* **15**, (2013), 250–256.

[239] P. Yeh. *Optical Waves in Layered Media*. Wiley Series in Pure and Applied Optics. Wiley, 2005.

[240] I. Horcas, R. Fernández, J. M. Gómez-Rodríguez, J. Colchero, J. Gómez-Herrero, and A. M. Baro. "WSXM: A software for scanning probe microscopy and a tool for nanotechnology". *Rev. Sci. Instrum.* **78**, (2007), 013705.

[241] W. Wang, H. Shen, B. Shuang, B. S. Hoener, L. J. Tauzin, N. A. Moringo, K. F. Kelly, and C. F. Landes. "Super Temporal-Resolved Microscopy (STReM)". *J. Phys. Chem. Lett.* **7**, (2016), 4524–4529.

[242] L. Xiang, K. Chen, R. Yan, W. Li, and K. Xu. "Super-resolution displacement mapping of unbound single molecules reveals nanoscale heterogeneities in intracellular diffusivity". *bioRxiv* (2019), 559484.

[243] I. Sase, H. Miyata, S. Ishiwata, and K. Kinosita. "Axial rotation of sliding actin filaments revealed by single-fluorophore imaging". *Proc. Natl Acad. Sci. USA* **94**, (1997), 5646–5650.

[244] S. B. Mehta, M. McQuilken, P. J. L. Riviere, P. Occhipinti, A. Verma, R. Oldenbourg, A. S. Gladfelter, and T. Tani. "Dissection of molecular assembly dynamics by tracking orientation and position of single molecules in live cells". *Proc. Natl Acad. Sci. USA* **113**, (2016), E6352–E6361.

[245] M. Ohmachi, Y. Komori, A. H. Iwane, F. Fujii, T. Jin, and T. Yanagida. "Fluorescence microscopy for simultaneous observation of 3D orientation and movement and its application to quantum rod-tagged myosin V". *Proc. Natl Acad. Sci. USA* **109**, (2012), 5294–5298.

[246] J. Lippincott-Schwartz and G. H. Patterson. "Photoactivatable fluorescent proteins for diffraction-limited and super-resolution imaging". *Trends Cell Biol.* Special Issue – Imaging Cell Biology **19**, (2009), 555–565.

[247] J. C. Vaughan, S. Jia, and X. Zhuang. "Ultrabright photoactivatable fluorophores created by reductive caging". *Nat. Methods* **9**, (2012), 1181–1184.

[248] S. v. d. Linde and M. Sauer. "How to switch a fluorophore: from undesired blinking to controlled photoswitching". *Chem. Soc. Rev.* **43**, (2014), 1076–1087.

[249] L. Cong, F. A. Ran, D. Cox, S. Lin, R. Barretto, N. Habib, P. D. Hsu, X. Wu, W. Jiang, L. A. Marraffini, and F. Zhang. "Multiplex Genome Engineering Using CRISPR/Cas Systems". *Science* **339**, (2013), 819–823.

[250] P. Mali, L. Yang, K. M. Esvelt, J. Aach, M. Guell, J. E. DiCarlo, J. E. Norville, and G. M. Church. "RNA-Guided Human Genome Engineering via Cas9". *Science* **339**, (2013), 823–826.

[251] W. Deng, X. Shi, R. Tjian, T. Lionnet, and R. H. Singer. "CASFISH: CRISPR/Cas9-mediated in situ labeling of genomic loci in fixed cells". *Proc. Natl Acad. Sci. USA* **112**, (2015), 11870–11875.

[252] A. O. Khan, V. A. Simms, J. A. Pike, S. G. Thomas, and N. V. Morgan. "CRISPR-Cas9 Mediated Labelling Allows for Single Molecule Imaging and Resolution". *Sci. Rep.* **7**, (2017), 8450.

[253] C. Hamers-Casterman, T. Atarhouch, S. Muyldermans, G. Robinson, C. Hammers, E. B. Songa, N. Bendahman, and R. Hammers. "Naturally occurring antibodies devoid of light chains". *Nature* **363**, (1993), 446.

[254] M. M. Harmsen and H. J. De Haard. "Properties, production, and applications of camelid single-domain antibody fragments". *Appl. Microbiol. Biotechnol.* **77**, (2007), 13–22.

[255] S. Muyldermans. "Nanobodies: Natural Single-Domain Antibodies". *Annu. Rev. Biochem.* **82**, (2013), 775–797.

[256] T. De Meyer, S. Muyldermans, and A. Depicker. "Nanobody-based products as research and diagnostic tools". *Trends Biotechnol.* **32**, (2014), 263–270.

[257] B. Traenkle and U. Rothbauer. "Under the Microscope: Single-Domain Antibodies for Live-Cell Imaging and Super-Resolution Microscopy". *Front. Immunol.* **8**, (2017).

[258] D. S. Liu, L. G. Nivón, F. Richter, P. J. Goldman, T. J. Deerinck, J. Z. Yao, D. Richardson, W. S. Phipps, A. Z. Ye, M. H. Ellisman, C. L. Drennan, D. Baker, and A. Y. Ting. "Computational design of a red fluorophore ligase for site-specific protein labeling in living cells". *Proc. Natl Acad. Sci. USA* **111**, (2014), E4551–E4559.

[259] I. Nikić, T. Plass, O. Schraidt, J. Szymański, J. A. G. Briggs, C. Schultz, and E. A. Lemke. "Minimal Tags for Rapid Dual-Color Live-Cell Labeling and Super-Resolution Microscopy". *Angew. Chem. Int. Ed.* **53**, (2014), 2245–2249.

[260] C. Uttamapinant, J. D. Howe, K. Lang, V. Beránek, L. Davis, M. Mahesh, N. P. Barry, and J. W. Chin. "Genetic Code Expansion Enables Live-Cell and Super-Resolution Imaging of Site-Specifically Labeled Cellular Proteins". *J. Am. Chem. Soc.* **137**, (2015), 4602–4605.

[261] T. Schvartz, N. Aloush, I. Goliand, I. Segal, D. Nachmias, E. Arbely, and N. Elia. "Direct fluorescent-dye labeling of α-tubulin in mammalian cells for live cell and superresolution imaging". *Mol. Biol. Cell* **28**, (2017), 2747–2756.

[262] D. Sage, H. Kirshner, T. Pengo, N. Stuurman, J. Min, S. Manley, and M. Unser. "Quantitative evaluation of software packages for single-molecule localization microscopy". *Nat. Methods* **12**, (2015), 717–724.

[263] D. Sage, T.-A. Pham, H. Babcock, T. Lukes, T. Pengo, J. Chao, R. Velmurugan, A. Herbert, A. Agrawal, S. Colabrese, A. Wheeler, A. Archetti, B. Rieger, R. Ober, G. M. Hagen, J.-B. Sibarita, J. Ries, R. Henriques, M. Unser, and S. Holden. "Super-resolution fight club: A broad assessment of 2D & 3D single-molecule localization microscopy software". *bioRxiv* (2018), 362517.

[264] S. Proppert, S. Wolter, T. Holm, T. Klein, S. v. d. Linde, and M. Sauer. "Cubic B-spline calibration for 3D super-resolution measurements using astigmatic imaging". *Opt. Express* **22**, (2014), 10304–10316.

[265] Y. Shechtman, S. J. Sahl, A. S. Backer, and W. E. Moerner. "Optimal Point Spread Function Design for 3D Imaging". *Phys. Rev. Lett.* **113**, (2014), 133902.

[266] W. Ouyang, A. Aristov, M. Lelek, X. Hao, and C. Zimmer. "Deep learning massively accelerates super-resolution localization microscopy". *Nat. Biotechnol.* **36**, (2018), 460–468.

[267] E. Nehme, L. E. Weiss, T. Michaeli, and Y. Shechtman. "Deep-STORM: super-resolution single-molecule microscopy by deep learning". *Optica* **5**, (2018), 458–464.

[268] N. Boyd, E. Jonas, H. P. Babcock, and B. Recht. "DeepLoco: Fast 3D Localization Microscopy Using Neural Networks". *bioRxiv* (2018), 267096.

[269] H. Wang, Y. Rivenson, Y. Jin, Z. Wei, R. Gao, H. Günaydın, L. A. Bentolila, C. Kural, and A. Ozcan. "Deep learning enables cross-modality super-resolution in fluorescence microscopy". *Nat. Methods* **16**, (2019), 103.

[270] E. Hershko, L. E. Weiss, T. Michaeli, and Y. Shechtman. "Multicolor localization microscopy and point-spread-function engineering by deep learning". *Opt. Express* **27**, (2019), 6158–6183.

[271] R. Strack. "Deep learning advances super-resolution imaging". *Nat. Methods* **15**, (2018), 403.

[272] R. Strack. "Deep learning in imaging". *Nat. Methods* **16**, (2019), 17.

[273] M. Wojcik, Y. Li, W. Li, and K. Xu. "Spatially Resolved in Situ Reaction Dynamics of Graphene via Optical Microscopy". *J. Am. Chem. Soc.* **139**, (2017), 5836–5841.

[274] W. Li, M. Wojcik, and K. Xu. "Optical Microscopy Unveils Rapid, Reversible Electrochemical Oxidation and Reduction of Graphene". *Nano Lett.* **19**, (2019), 983–989.